NEUROMORPHIC COMPUTING WITH ANTIFERROMAGNETIC ARTIFICIAL NEURONS

by

HANNAH D BRADLEY

A dissertation submitted in partial fulfillment of the
requirements for the degree of

DOCTOR OF PHILOSOPHY IN APPLIED AND COMPUTATIONAL PHYSICS

2024

Oakland University
Rochester, Michigan

Doctoral Advisory Committee:

Vasyl Tyberkevych, Ph.D., Chair
Andrei Slavin, Ph.D., Co-Chair
Evgeniy Khain, Ph.D.
Dmytro Bozhko, Ph.D.

To my mom and dad, Debra and David. Without your support, I could not have continued my education. I love you both.

To Joshua, you've stood by me through thick and thin, enduring countless hours of endless monologues. I'm going to get you so many lizards.

ACKNOWLEDGMENTS

I would like to extend my deepest gratitude to Dr. Vasyl Tyberkevych for his unwavering support and guidance over the past four years. His mentorship has been invaluable, instilling in me the confidence to persevere through challenging times and complete this thesis. I greatly appreciate the time and effort he invested in meeting with me to discuss my research and progress. I am also grateful to Dr. Andrei Slavin for his support and advice throughout my time at Oakland. I would like to thank my dissertation committee members, Dr. Evgeniy Khain and Dr. Dmytro Bozhko, for their time and insightful feedback on this thesis. Additionally, I would like to acknowledge my co-authors who contributed to the publications detailed in this dissertation. I am also thankful to the Air Force Office of Scientific Research (AFOSR) Multidisciplinary Research Program of the University Research Initiative (MURI) for their grant support.

Hannah D Bradley

ABSTRACT

NEUROMORPHIC COMPUTING WITH ANTIFERROMAGNETIC ARTIFICIAL NEURONS

by

Hannah D Bradley

Adviser: Vasyl Tyberkevych, Ph.D.

The increasing focus on Artificial Intelligence (AI) presents notable challenges, especially in the power requirements essential for training AI models. Consequently, there is a growing emphasis on neuromorphic computing, which aims to construct Artificial Neural Networks (ANNs) from artificial neurons to replicate the speed and efficiency of the human brain. With their significantly lower power consumption, spintronic devices acting as artificial neurons offer the potential for ANNs that rival conventional components. This innovative approach not only tackles the energy efficiency challenges but also paves the way for advancements in neuromorphic computing by integrating magnetic materials and spin-dependent effects. Antiferromagnetic (AFM) materials, characterized by their inherent THz frequencies, provide a unique opportunity for spintronic devices with ultra-fast dynamics.

There's a proposal to utilize AFM materials to craft ultra-fast spin-Hall oscillators. These oscillators emit spiking signals resembling those of biological neurons, indicating their potential as artificial neurons. AFM oscillators exhibit exceptionally fast characteristics, including picosecond-scale spike widths and unique features absent in conventional artificial neuron models. This research examines the utilization of AFM oscillators as artificial neurons and their significance in the realm of neuromorphic computing.

This dissertation begins with a comprehensive overview of relevant topics, covering the principles of spintronics, AFM materials, and neuromorphic computing. It examines the unique dynamics of AFM neurons, such as response latency and refraction time, which arise from an effective internal inertia. Then, it explores innovative AFM neuron circuits that exhibit functionalities unattainable by conventional artificial neurons, such as non-monotonic inhibition. Additionally, conventional learning algorithms like backpropagation are used to train AFM ANNs for pattern recognition. Finally, it leverages the similarities between AFM and biological neurons to model the biological neural network responsible for the withdrawal reflex.

With their simplistic design and high speeds, AFM neurons exhibit energy efficiencies several orders of magnitude higher than traditional artificial neurons and even other spintronic designs. This suggests that AFM ANNs will excel at training AI models while addressing the energy crisis impeding technological progress. As a result, AFM neurons drive forward the progress of spintronic neuromorphic computing, providing a promising alternative for future technological development.

TABLE OF CONTENTS

ACKNOWLEDGMENTS iv

ABSTRACT v

LIST OF TABLES xi

LIST OF FIGURES xii

LIST OF ABBREVIATIONS xv

CHAPTER ONE
INTRODUCTION 1

1.1. Motivation 1

1.2. Organization of the dissertation 6

CHAPTER TWO
BACKGROUND 8

2.1. Spintronics 8

2.1.1. Antiferromagnets 13

2.1.2. Antiferromagnetic oscillator 20

2.2. Neuromorphic computing 25

2.2.1. Artificial neural networks 26

2.2.2. Spiking neural networks 29

2.3. Spintronic neuromorphic computing 32

2.3.1. Antiferromagnetic neurons 36

CHAPTER THREE
BASIC DYNAMICAL PROPERTIES OF AFM NEURONS 43

3.1. Physical implementation and simulation parameters 45

3.2. Single AFM neuron behavior 50

3.2.1. AFM neuron spiking demonstration 50

3.2.2. AFM neuron refraction 55

3.2.3. AFM neuron polarity 58

3.3. Interconnecting AFM neurons 59

3.3.1. Mathematical model for AFM neural networks 63

3.3.2. Simple neuron chain 63

3.3.3. Symmetric coupling 67

3.4. Comparison of AFM neurons and biological neurons 73

3.5. Conclusion 74

CHAPTER FOUR
SIMPLE AFM NEURON CIRCUITS 76

4.1. AFM neurons as gates for Boolean logic 76

4.2. Inhibition 85

4.3. Memory cells 90

4.4. Conclusion 95

CHAPTER FIVE
PATTERN RECOGNITION WITH AFM NEURONS 96

5.1. SPAN neural network 97

5.1.1. Methods 97

5.1.2. Results 101

5.2. Gradient descent algorithm 107

5.3. Two layer neural network 109

5.3.1. Methods 109

5.3.2. Results 111

5.4. Two input graph neural network 111

5.4.1. Methods 114

5.4.2. Results 117

5.5. One input graph neural network 119

5.6. Conclusion 121

CHAPTER SIX
BIOLOGICAL NEURAL NETWORK MODELING 123

6.1. The withdrawal reflex 125

6.2. The Hodgkin-Huxley comparison 127

6.3. The withdrawal reflex neural network 130

6.4. Simulation results 133

6.4.1. Tone 133

6.4.2. Voluntary motion 134

6.4.3. Reaction to weak and strong stimuli 135

6.4.4. Inhibition of the withdrawal reflex 136

6.5. Conclusion 138

CHAPTER SEVEN
CONCLUSIONS 140

TABLE OF CONTENTS—Continued

APPENDICES

A. Pattern recognition neural networks 143

A.1. SPAN neural network 144

A.2. Two layer neural network 144

A.3. Graph neural networks 144

B. Withdrawal reflex neural network 145

REFERENCES 148

LIST OF TABLES

Table 3.1	AFM material parameters, fundamental constants, and physical dimensions used in simulations, unless otherwise noted.	46
Table B.1	Bias current values in the AFM withdrawal reflex neural network.	146
Table B.2	Synaptic connections in the AFM withdrawal reflex neural network.	148

LIST OF FIGURES

Figure 1.1	Von Neumann architecture.	2
Figure 2.1	Resistivity changes due to the parallel or anti-parallel orientation of magnetic layers in Fe/Cr multilayers of different thickness.	9
Figure 2.2	The progress of magnetic recording technology.	10
Figure 2.3	Ferromagnetic and Antiferromagnetic magnetic ordering.	14
Figure 2.4	AFM oscillator.	21
Figure 2.5	The typical structure of an ANN.	27
Figure 2.6	Output profile of different types of neurons.	30
Figure 2.7	Simulation results of an AFM SHNO at different regimes.	38
Figure 2.8	Simple pendulum as a mechanical analog of an AFM neuron.	39
Figure 3.1	AFM neuron.	44
Figure 3.2	Input current and simulated AFM neuron output.	51
Figure 3.3	AFM neuron spike characteristics.	55
Figure 3.4	Simulation demonstrating the refractory period of the AFM neuron.	57
Figure 3.5	Reversible polarity of a single AFM neuron.	58
Figure 3.6	AFM neuron interconnection.	60
Figure 3.7	Simulation results for five AFM neurons connected in a sequential chain.	64
Figure 3.8	Symmetric coupling and unidirectional signal propagation.	68

Figure 3.9	Isolator composed of symmetrically coupled neurons.	71
Figure 3.10	Combiner composed of symmetrically coupled neurons.	72
Figure 4.1	CMOS AND gate circuit.	77
Figure 4.2	AND gate implemented with an AFM neuron.	78
Figure 4.3	OR gate implemented with an AFM neuron.	80
Figure 4.4	Majority gate implemented with an AFM neuron.	83
Figure 4.5	Inhibitor circuit design.	85
Figure 4.6	Negative inhibition.	87
Figure 4.7	Positive inhibition.	89
Figure 4.8	Simple AFM neuron ring.	91
Figure 4.9	Double spiking AFM neuron ring.	92
Figure 4.10	AFM neuron memory cell.	93
Figure 4.11	Double spiking memory cell.	94
Figure 5.1	Single AFM SPAN neural network.	98
Figure 5.2	Simulation result of output signals generated by a trained AFM SPAN network.	100
Figure 5.3	Simulations depicting the training process of an AFM SPAN.	102
Figure 5.4	Simulation result of the output spikes of a trained AFM SPAN for different incorrect symbols.	103
Figure 5.5	Distribution of weights connecting inputs to SPAN.	103
Figure 5.6	Architecture of a 3 AFM SPAN neural network.	104

Figure 5.7	Simulated result of a 3 SPAN neural network for 3 different input symbols.	106
Figure 5.8	Two layer AFM neural network.	110
Figure 5.9	Two input graph AFM neural network.	112
Figure 5.10	Simulated inputs and outputs to the graph neural network at different points of training.	118
Figure 5.11	One input graph AFM neural network.	120
Figure 6.1	Circuit diagram of the Hodgkin-Huxley model of a biological neuron.	128
Figure 6.2	Architecture of the AFM withdrawal reflex artificial neural network.	131
Figure 6.3	Withdrawal reflex simulations in the absence of the sensory stimulus.	133
Figure 6.4	Simulated response of the withdrawal reflex arc to weak and strong sensory stimuli.	135
Figure 6.5	Simulated results for the inhibition of the withdrawal reflex.	137
Figure B.1	Complete AFM withdrawal reflex neural network.	147

LIST OF ABBREVIATIONS

AFM	Antiferromagnet
AFMR	Antiferromagnetic Resonance
AI	Artificial Intelligence
ANN	Artifical Neural Network
CMOS	Complementary Metal-Oxide-Semiconductor
CPU	Central Processing Unit
DARPA	Defense Advanced Research Projects Agency
DW	Domain Wall
FM	Ferromagnet
FMR	Ferromagnetic Resonance
GMR	Giant Magnetoresistance
IF	Integrate and Fire
LIF	Leaky Integrate and Fire
LL	Landau-Lifshitz
LLGS	Landau-Lifshitz-Gilbert-Slonczewski
MRAM	Magnetoresistive Random Access Memory
MTJ	Magnetic Tunnel Junction
NiO	Nickle-Oxide
Pt	Platinum
SHNO	Spin-Hall Nano-Oscillator
SNN	Spiking Neural Network
SPAN	Spike Pattern Association Neuron

STDP	Spike-Time-Dependent Plasticity
STNO	Spin-Torque Nano-Oscillator
STT	Spin Transfer Torque
VCMA	Voltage-Controlled Magnetic Anisotropy
WTA	Winner-Takes-All

CHAPTER ONE

INTRODUCTION

1.1 Motivation

Today's technology heavily relies on the movement of electrons to generate charge currents. However, in the late 20th century, a new revolutionary field called spintronics emerged, seeking to use the spin property of electrons for the creation of new technologies. Electron spin serves as the fundamental basis for magnetic ordering and various magnetic principles. Spintronics, short for spin-electronics, strives to use magnetic materials and spin-dependent principles to enhance present-day technology. Notably, spintronic devices offer the dual advantages of reduced energy consumption and a compact nano-scale size compared to conventional circuit elements. These attributes present an ideal solution to the current challenges impeding the progress of modern technologies.

Spintronic devices have already shown remarkable progress in enhancing energy-efficient memory storage and in-memory computing architectures [1]–[3]. For instance, Magnetoresistive Random Access Memory (MRAM), a non-volatile and non-destructive read-out memory, capitalizes on spintronic principles such as magnetic anisotropy to preserve and magnetoresistance to retrieve information, aiming to replace semiconductor-based memory technologies [4]. Another innovative approach, Domain Wall (DW) racetrack memory, involves the movement of magnetic DWs representing bits along a track [5]. Writing and reading information on these racetracks via DW motion employs various spintronic principles, including magnetoresistance, spin momentum transfer torque, and spin-polarized current.

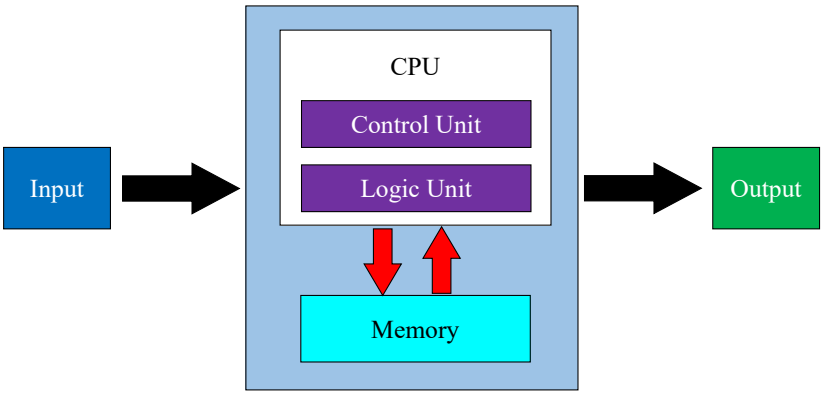

Figure 1.1: Von Neumann architecture. This computing scheme is characterized by its separate computational and memory elements. Data must be transferred back and forth from the CPU and memory during computation, as depicted by the red arrows.

Modern technology depends on digital computers operating within Von Neumann architecture, visually depicted in Fig. 1.1 [6], [7]. This architectural paradigm is characterized by a Central Processing Unit (CPU) working parallel to a separate memory unit. During processing, data shuttles back and forth between the CPU and memory, significantly amplifying both time and energy consumption per operation. These drawbacks lead to the Von-Neumann bottleneck, which, if not resolved, will limit future computational capabilities.

In contrast, the human brain stands out as an energy-efficient processor, accomplishing analyses with a power consumption of less than 20 W [8]. The efficiency is attributed to the brain's locally storing memory, eliminating the need for data transfer outside of the computational elements during processing. It is natural for software and hardware developers to turn to the brain for inspiration as they work to improve the challenges posed by the Von Neumann bottleneck. This innovative approach is known as neuromorphic computing, with the goal of emulating both the computational speed and power efficiency of the human brain.

Neuromorphic computing uses machine learning algorithms to train Artifical Neural Networks (ANNs) [9], designed to mirror the fundamental elements of the human brain—neurons and synapses. Artificial neurons function as individual processing units interconnected by artificial synapses. Machine learning algorithms execute computations by adjusting the strength of synaptic connections, enabling the creation of new pathways between neurons. With memory stored locally within neurons and synapses, ANNs exhibit computational speeds and energy efficiency that rival the most proficient Von Neumann architectures.

The core building blocks of ANNs are the artificial neurons, which process information by combining inputs through interconnected synapses. Following this, a non-linear activation function, such as the sigmoid function, computes the output. ANNs using non-linear activation functions has exhibited remarkable success in the realm of Artificial Intelligence (AI). Notably, in 2023, OpenAI unveiled ChatGPT-3, a remarkable language model in the form of a chatbot, which contributed to refining the language of this dissertation [10], [11]. Operating on an ANN with a staggering 175 billion neurons and synapses, ChatGPT has achieved significant milestones. However, despite its accomplishments, several drawbacks still exist. Estimates suggest that training a large language model like ChatGPT requires up to 10 GWh of energy [12], equivalent to the yearly energy consumption of 1,000 American households. Although ChatGPT's staggering power consumption is an approximation, other AI models also report substantial energy usage. Deep Blue, a formidable chess-playing supercomputer [13], and AlphaGo, an AI model proficient in playing the intricate game of Go [14], [15], consume 3 kW and 1 MW of power, respectively. Clearly, all these instances of ANN-powered AI exhibit unsustainable power demands.

One key factor contributing to the brain's remarkable energy efficiency is the communication between biological neurons through voltage spikes known as action

potentials. It has been suggested that incorporating artificial neurons capable of producing spikes akin to those in biological neurons could significantly enhance the energy efficiency and speed of ANNs. These Spiking Neural Networks (SNNs) use artificial neurons that generate voltage spikes upon reaching a threshold, similar to the action potential production in biological neurons. In 2021, Intel introduced the Loihi 2 spiking neuromorphic chip. This SNN featured 1 million neurons and 120 million synapses, showcasing a substantial reduction in power consumption compared to other ANNs. Intel reported that the Loihi 2 chip requires merely 20 pJ per operation in 3.5 ns [16], highlighting how SNNs may be the future of neuromorphic computing.

However, the success of the Loihi chip also illustrates a challenge in current neuromorphic technology. To simulate its 1 million neurons and 120 million synapses, the Loihi 2 chip needs a staggering 2.3 billion Complementary Metal-Oxide-Semiconductor (CMOS) transistors [16], [17]. This reveals a substantial hardware-to-element loss, as numerous transistors are needed to create a single artificial neuron or synapse. Consequently, the associated area and power requirements are substantial, as evidenced by Loihi 2's 31 mm^2 area.

In recent years, the exploration of spintronic devices as an alternative to transistor-based neuromorphic computing has gained significant interest [18]–[20]. The use of spintronic principles holds promise for overcoming the limitations in transistor-based neural networks, as evident by the success of spintronic in-memory technology. Spintronic devices exhibit inherent non-linear dynamics, rendering them viable as activation functions for artificial neurons. Many spintronic devices utilized in neuromorphic computing can be fabricated on a nanometer scale, with a single device functioning as an individual neuron or synapse. Consequently, spintronic devices demand less area and power when compared to their transistor-based counterparts. It is well-documented that many spintronic devices can be used to create artificial neurons and

synapses. This dissertation aims to introduce a novel spintronic device designed for neuromorphic computing.

Despite the growing prevalence of spintronic devices in this domain, there remains a notable gap in the exploration of Antiferromagnets (AFMs). AFM materials, characterized by two opposing magnetic sublattices, present unique challenges due to their limited response to external magnetic fields. Nonetheless, AFM materials offer numerous advantages, including the absence of stray magnetic fields, enabling much denser packing of AFM devices, and a wide array of AFM materials with diverse properties. A significant advantage of AFMs lies in their intrinsic resonance frequency, which falls within the THz range, making them promising candidates for high-speed spintronic devices. Proposals have been made to utilize AFM materials for the development of ultra-fast oscillators [21]–[25]. Nano-sized AFM spin-Hall oscillators exhibit THz generation frequencies while maintaining exceptional energy efficiency.

The core objective of this dissertation is to demonstrate the use of an AFM oscillator as a spiking artificial neuron for neuromorphic computing. Similar to other spintronic devices, AFM neurons can be crafted on a nanometer scale, significantly reducing area requirements compared to conventional transistor-based models. Leveraging the THz dynamics of AFMs, these neurons operate on an exceptionally fast time scale, surpassing the speeds achievable by typical transistor-based or other spintronic device-based artificial neurons. This speed, coupled with the simplistic design of the AFM oscillator, leads to a power consumption of several orders of magnitude lower than current spiking neuromorphic circuits.

This dissertation aims to unveil the extraordinary potential of AFM materials to revolutionize AI and neuromorphic computing. Utilizing a theoretical mathematical model, it establishes that an AFM oscillator possesses the essential characteristics for simulating a spiking artificial neuron. The strong exchange interaction within the AFM

sublattices gives rise to an effective inertia, leading to an array of distinctive properties, including biologically realistic response latency, refraction time, and bursting dynamics, setting them apart from conventional artificial neuron models. Furthermore, when interconnected, AFM neurons form static circuits capable of executing functions unattainable by traditional ANNs. For instance, the AFM inhibitor circuit emulates non-monotonic inhibition observed in biological neurons but impossible with conventional inertia-less neural networks. Additionally, AFM SNNs effectively employ machine learning algorithms for pattern recognition, a common benchmark task in neuromorphic computing. Leveraging the distinctive characteristics of AFM neurons, these SNNs achieve exceptional accuracy in pattern recognition tasks at high speeds with minimal power consumption. Moreover, due to the striking similarities between AFM neurons and their biological counterparts, AFM neurons can realistically model complex biological neural networks using fewer than 50 AFM neurons while other models require over 2,000 artificial neurons. The findings of this dissertation not only expand the field of spintronic neuromorphic computing in a new direction but also give a glimpse into the future of high-speed energy-efficient AI.

1.2 Organization of the dissertation

Chapter 2 provides a general background for topics relevant to this thesis. This chapter begins with an introduction to the field of spintronics and AFM materials. It includes the derivation of the mathematical model for AFM neurons used throughout this dissertation. After this, it covers the inception of neuromorphic computing and ANNs. Subsequently, the chapter establishes a linkage between spintronics and neuromorphic computing. Lastly, AFM neurons are introduced, laying the groundwork for their exploration in subsequent chapters.

Chapters 3-6 cover the original results obtained for this dissertation. These results were presented in 3 peer-reviewed papers [26]–[28] and 18 conference presentation [29]–[46].

Chapter 3 is dedicated to providing details of AFM neurons, including material parameters and single-neuron behavior. Subsequently, it investigates the coupling of AFM neurons in chains and examines the resulting dynamics, exploring both uni-directional and bi-directional coupling.

Chapter 4 presents multiple examples of simple AFM neuron circuits. It begins with the utilization of AFM neurons as Boolean logic gates and concludes by exploring memory rings and inhibitors, two distinctive circuits unique to AFM neurons.

Chapter 5 delves into the training of AFM neurons for pattern recognition, a standard neuromorphic computing benchmark task. Initially, it discusses a simple supervised learning algorithm and the subsequent creation of a one-layer neural network. It then elaborates on more complex multilayered AFM neural networks and the gradient descent algorithm utilized for their training.

Chapter 6 uses AFM neurons to model a biological neural network, the withdrawal reflex arc. This chapter provides insight into the biological aspects of the withdrawal reflex, as well as juxtaposing the AFM neuron equation with a mathematical model for biological neurons. Following an overview of the neural network utilized in this investigation, the chapter delineates the five simulated scenarios aimed at modeling the biological withdrawal reflex.

Chapter 7 summarizes the findings of this dissertation, providing a comprehensive overview of the research outcomes. Additionally, the chapter outlines potential directions for future research in the field.

CHAPTER TWO

BACKGROUND

This dissertation serves a unique purpose, forming a bridge between two fields: spintronics and neuromorphic computing. By exploring the intersection of these fields, it introduces a novel research domain where spintronic principles and devices are used in neuromorphic computing architectures. This chapter provides an in-depth exploration of the background of both fields and establishes a connection between them.

The chapter will begin with an introduction to the field of spintronics, offering insights into its inception and detailing the key physical principles relevant to this study. It will then delve into AFM materials and their application in the development of ultra-fast oscillators. Following this, the chapter will transition to an exploration of neuromorphic computing. It will provide a comprehensive overview of neuromorphic computing, offering a history of traditional and non-traditional computing approaches and providing context for the evolution of computational paradigms. Then, it will establish a connection between the two fields and give an overview of recent breakthroughs in spintronic neuromorphic computing. Finally, the chapter will introduce AFM neurons, setting the stage for subsequent discussions and analyses within this dissertation.

2.1 Spintronics

By the mid-20th century, it was established that electron spin plays a pivotal role in magnetism and magnetic materials [47]. This realization gave rise to a new field of science, called spintronics, where magnetic materials and electron spin-dependent effects were harnessed to develop a diverse array of nano-scale devices [48]–[51].

Spintronics was kicked started by the discovery of Giant Magnetoresistance (GMR) in 1988 [52], [53]. While working with thin metallic films, Grünberg and Fert

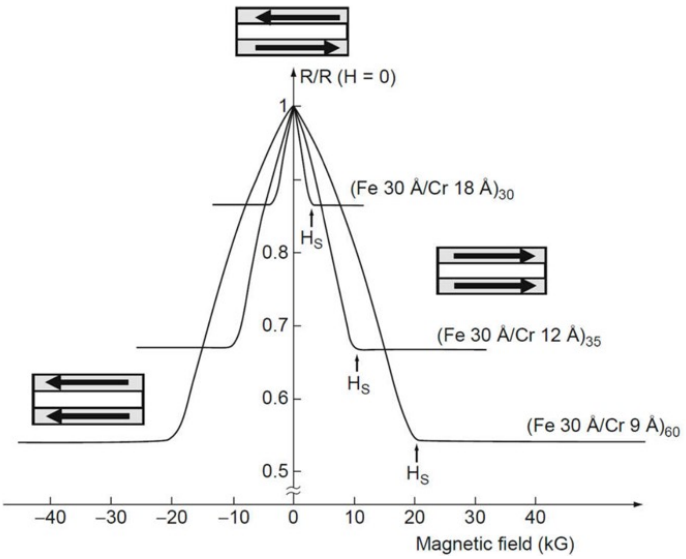

Figure 2.1: Resistivity changes due to the parallel or anti-parallel orientation of magnetic layers in Fe/Cr multilayers of different thickness. This figure was published in 'Nanomagnetism and Spintronics', Teruya Shinjo, pg 32, Copyright Elsevier 2009.

observed that two Ferromagnet (FM) layers aligned either in a parallel or anti-parallel state, depending on the thickness of a non-magnetic spacer and applied magnetic field. This configuration of two FM layers and a non-magnetic spacer was coined as a spin valve. The breakthrough made by Grünberg and Fert was the revelation that the parallel alignment of FM layers in the spin valve corresponded to a low-resistance state, while the anti-parallel state exhibited high resistance, as illustrated in Fig. 2.1. The discovery of GMR paved the way for the development of highly sensitive sensors capable of detecting external magnetic fields through electrical resistance. Grünberg and Fert were awarded the Nobel Prize in 2007 in recognition of their groundbreaking discovery.

Since its discovery, GMR has found widespread application in various sensor technologies across diverse fields [54]. However, GMR's most significant impact on modern technology lies in its role in hard-disc read-heads [54], [55]. In the realm of

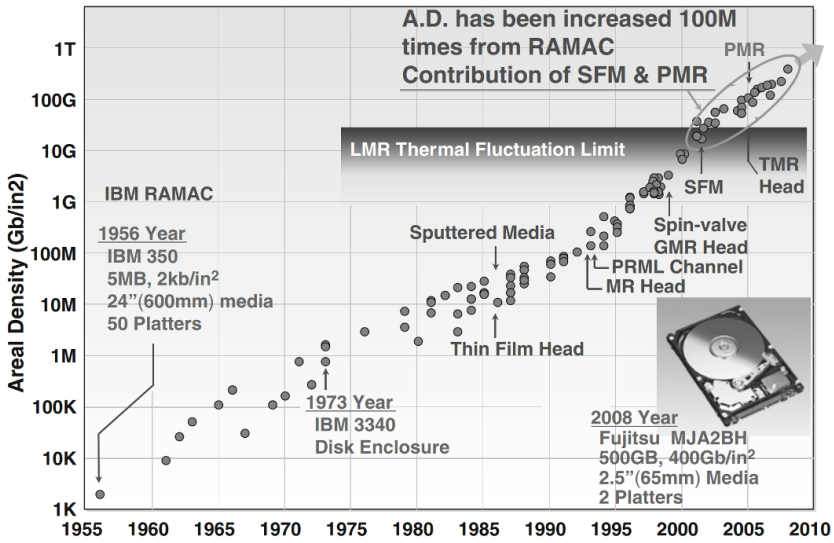

Figure 2.2: The progress of magnetic recording technology. LMR, SFM, and PMR mean longitudinal magnetic recording, synthetic antiferromagnetism, and perpendicular magnetic recording, respectively. The thermal fluctuation limit was thought to be the highest attainable boundary for recording density before the appearance of GMR. This figure was published in 'Nanomagnetism and Spintronics', Teruya Shinjo, pg 8, Copyright Elsevier 2009.

computer data storage, information is encoded as bits through magnetic recording, wherein the magnetization direction is employed to represent 0s and 1s. A GMR sensor is then utilized to read these bits by detecting the magnetization direction through its resistance. This synergy between magnetic recording and the application of a GMR sensor is known as MRAM. Commercial products incorporating GMR read heads and MRAM have played a pivotal role in advancing magnetic recording technology, as illustrated in Fig. 2.2. In 1996, Defense Advanced Research Projects Agency (DARPA) coined the term spintronics, short for SPIN TRansfer elecTRONICS, as a new project to develop both non-volatile MRAM and also magnetic sensors for specialized applications [56], [57]. Since its inception, spintronics has transcended its initial focus on GMR to encompass a broader spectrum, now defined as a field that harnesses electron spin and spin-dependent effects.

Modern technology heavily relies on electron movement to generate charge currents. Traditionally, the focus has been solely on the electron's charge, overlooking its spin. The idea of spin-polarized electrical current was initially proposed by Mott in 1936, almost half a century before the discovery of GMR [58]. Mott illustrated that electrons carrying electrical current through FMs exhibit spin polarization. This concept evolved over time, simplifying its terminology to *spin current*, indicating the flow of electrons with a net spin.

The impact of spin currents on magnetic materials is profound. As electrons traverse the spin valve structure, the electrical current becomes spin-polarized, aligning with the direction of the first FM layer and retaining this polarization within the non-magnetic tunnel barrier. Consequently, when the magnetization of the second FM layer is anti-parallel to the first, the spin polarization of the current changes. This change occurs due to the conservation of momentum principle. Spin, representing the angular momentum of electrons, prompts the rotation of the magnetization of the second FM layer

through *Spin Transfer Torque (STT)* [59]–[61]. This phenomenon was predicted in 1996 by both Slonczewski [62] and Berger [63], who posited that a spin current perpendicular to the magnetization direction could yield a sufficiently robust torque to reorient the magnetization. This discovery challenged previous assumptions that magnetization could only be influenced by an external magnetic field.

While STT arises from current-induced magnetization dynamics, an inverse process also exists. In this process, the precession of magnetization within a FM layer influences the spin state of an adjacent non-magnetic layer, a phenomenon known as *spin pumping*. First described in 2002 by Tserkovnyak and Bratass, spin pumping was introduced alongside the term "spin battery", used to describe FM/non-magnetic structures exhibiting this effect [64]–[67]. Similar to a conventional battery generating electrical current, the spin battery structure generates a spin current via spin pumping. Notably, the spin current produced through spin pumping is decoupled from electric current, constituting what is known as *pure spin current*. In pure spin current, electrons with opposing spins move in opposite directions, resulting in zero net movement of electrons and, consequently, zero charge current. The emergence of pure spin current holds immense potential for technological advancement, as it eliminates Ohmic losses typically associated with charge current flow. Spin current could be the foundation for future ultra-energy-efficient technology.

Spin pumping is not the sole method for generating spin currents. The spin-orbit interaction, a fundamental phenomenon in magnetic materials, influences electron trajectories by their spin properties. As a result, when electrons traverse a material under the influence of an applied electric field, there is a spin accumulation at opposite edges. This accumulation leads to the generation of pure spin current perpendicular to the direction of the electrical field, a phenomenon called the *spin-Hall effect* [60], [68], [69].

The spin-Hall effect facilitates the conversion of charge current into pure spin current, further expanding the avenues for spintronic research and applications.

These spintronic effects are harnessed to develop a myriad of devices and applications aimed at advancing technology. Later in this chapter, the spin-Hall effect and spin pumping will be the focus of particular attention, as they are the foundational principles for constructing the nano-oscillator that forms the basis of this dissertation.

2.1.1 Antiferromagnets

Many applications of magnetism and spintronic principles solely rely on the use of FM materials. FM materials exhibit a unidirectional magnetic lattice, where each electron spin aligns in the same direction as its neighbor, as depicted in Fig. 2.3(a). Consequently, FM materials have a magnetic moment, causing them to be responsive to external magnetic influences. However, in 1932, Louis Néel proposed the existence of materials with two opposing magnetic sublattices, calling them AFMs [70]. The electrons of these materials exhibit an alternating spin pattern, where electron spins point in the opposite direction to their neighbors, as depicted in Fig. 2.3(b). As a result of their opposing sublattices, AFM materials lack a magnetic moment. Hence, AFMs react weakly to external magnetic fields, rendering most experimental methods of the time useless. When Néel accepted the Nobel Prize in 1970 for his discovery, he described these AFMs as "interesting but useless" [71].

AFM's uniqueness stems from the energy shared between neighboring electrons. This spin-dependent energy can be modeled by the Heisenberg exchange hamiltonian between nearest neighbors,

$$H = -2\sum_{i>j} J_{i,j}\left(\boldsymbol{S}_i \cdot \boldsymbol{S}_j\right), \tag{2.1}$$

where $\boldsymbol{S}$ is the spin operator and J is the exchange constant between neighbors [72]. The sign of the exchange constant determines the system's ground state. In the case of a

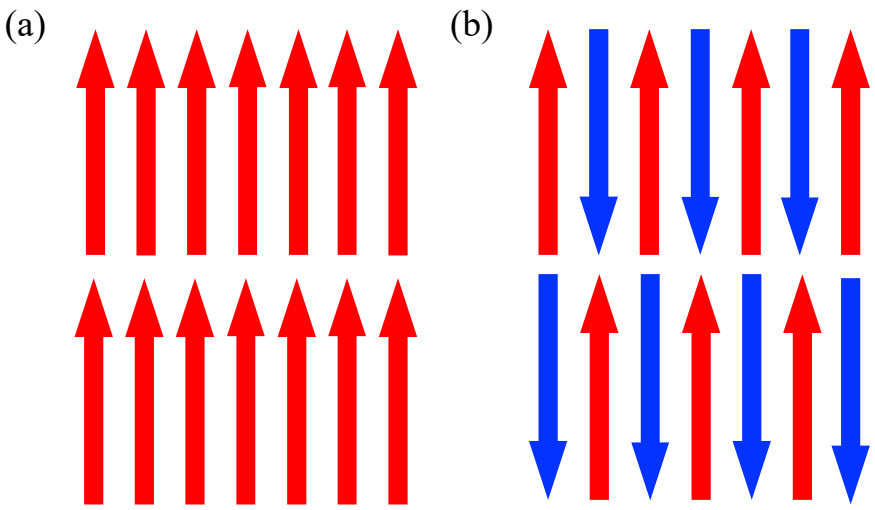

Figure 2.3: Ferromagnetic and Antiferromagnetic magnetic ordering. (a) Ferromagnetic ordering. Neighboring spins are parallel, resulting in one magnetic sublattice. (b) Antiferromagnetic ordering. Neighboring spins are antiparallel, resulting in two opposing magnetic sublattices.

positive exchange constant, $J > 0$, the material favors a FM ordering where all spins point in the same direction (Fig. 2.3(a)). But a negative exchange constant, $J < 0$, suggested AFM ordering, where neighboring spins are antiparallel (Fig. 2.3(b)). As the FM sublattice is aligned, it can be described through one vector $\boldsymbol{m}$ for its magnetic moment. However, AFMs lack a magnetic moment due to the antiparallel alignment of their sublattices. Thus, each sublattice must be described through its own magnetization vector, $\boldsymbol{m}_1$ and $\boldsymbol{m}_2$. Although AFMs lack a magnetic moment, the sublattices may still be described through one vector termed the Néel vector,

$$\boldsymbol{l} = \frac{1}{2}(\boldsymbol{m}_1 - \boldsymbol{m}_2). \tag{2.2}$$

Many examples of AFM materials exist, each possessing a diverse array of properties. Metallic AFM materials are valued for their high electrical and thermal conductivities, as well as their robust interactions between electrons, spin, phonons, and

photons [73]. On the other hand, AFM insulators are prized for their suitability in studying spin waves [74]. Thanks to their strong reaction to spin-Hall effects and spin current coupling, these insulators are primarily employed in the creation of oscillators. Historically, AFM materials were primarily conceptualized within theoretical frameworks, as their weak responses to external magnetic fields hindered experimental study. However, the emergence of STT technology has begun to revolutionize this landscape, enabling the manipulation of their magnetic sublattices. Extensive research efforts have been devoted to uncovering the practical applications of AFMs. Presently, their industrial utilization is limited, with hard-disk manufacturing standing as the sole known application.

The dynamics of AFM materials differ significantly from those of FM materials due to their lack of magnetic moment. When analyzing the dynamics of magnetic materials, four main components must be considered: Zeeman energy, dipolar interaction, exchange interaction, and magnetic anisotropy. Zeeman energy describes how an external magnetic field affects a magnetic material [72]. In FMs, the external field aligns the magnetic moment parallel to its direction. However, in AFMs, where there is no net magnetic moment, the external field must counteract a strong exchange interaction that maintains the sublattices antiparallel. Consequently, a substantial external field is required to influence the sublattices, resulting in a weak Zeeman energy for AFMs. Furthermore, the dipolar interaction, crucial in FMs due to the presence of a net magnetic moment, becomes negligible in AFMs where no such moment exists. Even when external factors attempt to realign the sublattices of AFMs, the dipolar interaction remains weak. The exchange interaction, present in both FM and AFM materials, functions to maintain the alignment within their respective sublattices. In FMs, this alignment is parallel, while in AFMs, it is antiparallel. Similarly, anisotropy serves the same purpose in both materials, orienting the sublattices along a preferred direction. Given the weak influence of Zeeman

energy and dipolar interaction, the exchange interaction and magnetic anisotropy assume crucial roles in the behavior of AFM materials.

AFM materials exhibit a diverse range of anisotropies. In uniaxial anisotropic AFMs, the sublattices align along a single axis, or in other words, the Néel vector lies parallel to this axis. Any deviations from this axis require significant energy. Alternatively, uniaxial easy plane AFM materials have a preferred plane where the sublattices lie. While the sublattices can rotate within this plane, pushing the Néel vector outside this preferred orientation requires substantial energy. This study focuses on a biaxial anisotropic AFM, where an additional biaxial anisotropy exists within the easy plane in the form of an easy and hard axis. Using this biaxial anisotropic material, the effective anisotropy field experienced by the sublattices takes the form,

$$\boldsymbol{B}_{an,1} = -B_h\,\boldsymbol{n}_h\,(\boldsymbol{n}_h\cdot\boldsymbol{m}_1) + B_e\,\boldsymbol{n}_e\,(\boldsymbol{n}_e\cdot\boldsymbol{m}_1), \tag{2.3a}$$

$$\boldsymbol{B}_{an,2} = -B_h\,\boldsymbol{n}_h\,(\boldsymbol{n}_h\cdot\boldsymbol{m}_2) + B_e\,\boldsymbol{n}_e\,(\boldsymbol{n}_e\cdot\boldsymbol{m}_2), \tag{2.3b}$$

where B_h and B_e are the hard-axis and easy-plane anisotropy fields, respectively, and $\boldsymbol{n}_h$ and $\boldsymbol{n}_e$ are the unit vectors along the hard and easy axis, respectively. As this work is based on a biaxial anisotropic AFM, the following equations will be for biaxial AFMs.

The dynamics of a biaxial anisotropic AFM can be described through two coupled Landau-Lifshitz (LL) equations for the magnetic sublattices;

$$\dot{\boldsymbol{m}}_1 = |\gamma|\,\boldsymbol{B}_{eff,1}\times\boldsymbol{m}_1, \tag{2.4a}$$

$$\dot{\boldsymbol{m}}_2 = |\gamma|\,\boldsymbol{B}_{eff,2}\times\boldsymbol{m}_2, \tag{2.4b}$$

where the effective magnetic fields acting on the sublattices take the form,

$$\boldsymbol{B}_{eff,1} = -\frac{1}{2}\,B_{ex}\,\boldsymbol{m}_2 + \boldsymbol{B}_{an,1} = -\frac{1}{2}\,B_{ex}\,\boldsymbol{m}_2 - B_h\,\boldsymbol{n}_h\,(\boldsymbol{n}_h\cdot\boldsymbol{m}_1) + B_e\,\boldsymbol{n}_e\,(\boldsymbol{n}_e\cdot\boldsymbol{m}_1), \tag{2.5a}$$

$$\boldsymbol{B}_{eff,2} = -\frac{1}{2}\,B_{ex}\,\boldsymbol{m}_1 + \boldsymbol{B}_{an,2} = -\frac{1}{2}\,B_{ex}\,\boldsymbol{m}_1 - B_h\,\boldsymbol{n}_h\,(\boldsymbol{n}_h\cdot\boldsymbol{m}_2) + B_e\,\boldsymbol{n}_e\,(\boldsymbol{n}_e\cdot\boldsymbol{m}_2), \tag{2.5b}$$

where γ is the gyromagnetic ratio and B_{ex} is the exchange field. As one can see, only exchange and anisotropy terms are present in the effective magnetic fields, unlike FMs where Zeeman energy and dipolar interaction are present. Again, this is due to AFMs lacking a magnetic moment due to the antiparallel orientation of their sublattices. With the wide diversity of different AFM materials, these fields come in a variety of values. For example, in Nickle-Oxide (NiO), the AFM material used throughout this dissertation, the exchange field is $B_{ex} \approx 800$ T, while the anisotropy fields are $B_h = 1.56$ T and $B_e = 62.5$ mT [21]. These parameters are typical for AFM materials at room temperature. It is clear that the exchange field will dominate in the LL equations. Thus, Eqs (2.4) can be rewritten as;

$$\dot{\boldsymbol{m}}_1 = -\frac{1}{2}\,\gamma\, B_{ex}\, \boldsymbol{m}_2 \times \boldsymbol{m}_1 + \boldsymbol{T}_1, \tag{2.6a}$$

$$\dot{\boldsymbol{m}}_2 = -\frac{1}{2}\,\gamma\, B_{ex}\, \boldsymbol{m}_1 \times \boldsymbol{m}_2 + \boldsymbol{T}_2, \tag{2.6b}$$

where:

$$\boldsymbol{T}_1 = -B_h\, \boldsymbol{n}_h\, (\boldsymbol{n}_h \cdot \boldsymbol{m}_1) \times \boldsymbol{m}_1 + B_e\, \boldsymbol{n}_e\, (\boldsymbol{n}_e \cdot \boldsymbol{m}_1) \times \boldsymbol{m}_1, \tag{2.7a}$$

$$\boldsymbol{T}_2 = -B_h\, \boldsymbol{n}_h\, (\boldsymbol{n}_h \cdot \boldsymbol{m}_2) \times \boldsymbol{m}_2 + B_e\, \boldsymbol{n}_e\, (\boldsymbol{n}_e \cdot \boldsymbol{m}_2) \times \boldsymbol{m}_2. \tag{2.7b}$$

As AFMs are characterized by their opposing sublattices, 2 LL equations are required. However, they can be simplified using the σ model, where the 2 coupled equations are simplified into a single equation [75], [76]. In this model, the LL equations are rewritten in terms of the magnetization vector, $\boldsymbol{m}$, and the Néel vector, $\boldsymbol{l}$;

$$\boldsymbol{m} = \frac{1}{2}(\boldsymbol{m}_1 + \boldsymbol{m}_2), \tag{2.8}$$

$$\boldsymbol{l} = \frac{1}{2}(\boldsymbol{m}_1 - \boldsymbol{m}_2). \tag{2.2}$$

The Néel vector, $\boldsymbol{l}$, lies in the easy plane of the AFM, and due to their orthogonality, the magnetization vector, $\boldsymbol{m}$, points out of the easy plane. As the two sublattice magnetizations of the AFM are antiparallel, the total magnetization vector for the AFM is weak, and therefore, its direction does not contribute to the overall dynamics of the AFM.

To derive the σ model, the derivative of $\boldsymbol{m}$ and $\boldsymbol{l}$ are found to be:

$$\dot{\boldsymbol{m}} = \frac{1}{2}(\boldsymbol{T}_1 + \boldsymbol{T}_2), \tag{2.9}$$

$$\dot{\boldsymbol{l}} = \left(\frac{1}{4}\,\gamma\, B_{ex}\, \boldsymbol{m}_1 \times \boldsymbol{m}_2 + \boldsymbol{T}_1 + \frac{1}{4}\,\gamma\, B_{ex}\, \boldsymbol{m}_1 \times \boldsymbol{m}_2 - \boldsymbol{T}_2\right). \tag{2.10}$$

The exchange field, B_{ex}, in Eq. (2.10) is much larger than the combined anisotropy fields in $\boldsymbol{T}_1$ and $\boldsymbol{T}_2$; therefore, the latter can be dropped resulting in the derivative of the Néel vector to be:

$$\dot{\boldsymbol{l}} = \frac{1}{2}(\gamma\, B_{ex}\, \boldsymbol{m}_1 \times \boldsymbol{m}_2). \tag{2.11}$$

This equation can then be rewritten in terms of $\boldsymbol{m}$ and $\boldsymbol{l}$:

$$\dot{\boldsymbol{l}} = \gamma\, B_{ex}\, \boldsymbol{l} \times \boldsymbol{m}. \tag{2.12}$$

Using the orthogonality of $\boldsymbol{m}$ (Eq. (2.8)) and $\boldsymbol{l}$ (Eq. (2.2)), the magnetization vector $\boldsymbol{m}$ can be written as a slave variable:

$$\boldsymbol{m} = -\frac{1}{\gamma\, B_{ex}} \boldsymbol{l} \times \dot{\boldsymbol{l}}. \tag{2.13}$$

Using Eq. (2.13), the dynamics of the Néel vector, $\boldsymbol{l}$, can be rewritten as a single second-order vectorial differential equation:

$$\boldsymbol{l} \times \left[\frac{1}{\omega_{ex}} \ddot{\boldsymbol{l}} + \omega_h\, \boldsymbol{n}_h\, (\boldsymbol{n}_h \cdot \boldsymbol{l}) - \omega_e\, \boldsymbol{n}_e\, (\boldsymbol{n}_e \cdot \boldsymbol{l})\right] = 0, \tag{2.14}$$

where $\omega_{ex} = \gamma B_{ex}$, $\omega_e = \gamma B_e$, and $\omega_h = \gamma B_h$. For NiO, $\omega_{ex} = 2\pi \times 27.5$ THz, $\omega_e = 2\pi \times 1.75$ GHz, and $\omega_h = 2\pi \times 43.9$ GHz [21]. This σ model simplifies the coupled LL equations into one equation, which can be solved to describe the rotation of the sublattices of AFMs.

One advantage of working with AFM materials is their high precession frequencies. FM excitation frequencies, or Ferromagnetic Resonance (FMR), have values in the GHz range and rely on shape anisotropy and external magnetic fields. Antiferromagnetic Resonance (AFMR) frequencies for a biaxial AFM are found from Eq. (2.14) and have the forms;

$$\omega_1 \approx \sqrt{\omega_{ex}\ \omega_e}, \tag{2.15a}$$

$$\omega_2 \approx \sqrt{\omega_{ex}\ (\omega_h + \omega_e)}. \tag{2.15b}$$

Equation (2.15a) describes the AFMR mode in which the Néel vector remains in the easy plane and for NiO has a value of 0.2 THz. Alternatively, Eq. (2.15b) describes the mode when the Néel vector rotates out of the easy plane and for NiO has a value of 1 THz. In comparison, the FMR for YIG, a commonly used FM, is ≈ 10 GHz for a reasonable external bias field of $B_{ext} = 0.6$ T [77]. The difference in resonance frequencies between materials arises from an effect known as *exchange amplification*. In AFMR, the large exchange factor amplifies the small anisotropies, leading to much higher frequencies compared to FMR, where only anisotropy and external fields are present. Consequently, AFMR frequencies typically lie in the terahertz range, whereas those of FMR are in the gigahertz range.

The LL equations, Eqs (2.4), only consider the effective anisotropy and exchange fields felt by the AFM sublattices. However, other factors come into effect when describing real systems. The AFM sublattices can be made to rotate through STT. Therefore, when manipulating the sublattices with STT, a torque term should be added to

the LL equations. Additionally, Gilbert damping is a material property of the AFM that affects the rotation of the sublattices and, therefore, should be taken into consideration. With the addition of these terms, the sublattices of the AFM are described through 2 coupled Landau-Lifshitz-Gilbert-Slonczewski (LLGS) equations;

$$\dot{\boldsymbol{m}}_1 = \gamma \boldsymbol{B}_{eff,1} \times \boldsymbol{m}_1 + \alpha(\boldsymbol{m}_1 \times \dot{\boldsymbol{m}}_1) + \tau\, \boldsymbol{m}_1 \times (\boldsymbol{m}_1 \times \boldsymbol{p}), \tag{2.16a}$$

$$\dot{\boldsymbol{m}}_2 = \gamma \boldsymbol{B}_{eff,2} \times \boldsymbol{m}_2 + \alpha(\boldsymbol{m}_2 \times \dot{\boldsymbol{m}}_2) + \tau\, \boldsymbol{m}_2 \times (\boldsymbol{m}_2 \times \boldsymbol{p}), \tag{2.16b}$$

where α is the effective Gilbert damping, τ is the magnitude of STT [21], [66], and $\boldsymbol{p}$ is a unit vector along the spin current polarization. The effective magnetic fields are the same as in Eq. (2.5). Following the same steps as before, the σ model is used to simplify the LLGS equations into one second-order vectorial differential equation:

$$\boldsymbol{l} \times \left[\frac{1}{\omega_{ex}} \ddot{\boldsymbol{l}} + \alpha\, \dot{\boldsymbol{l}} + \omega_h\, \boldsymbol{n}_h\, (\boldsymbol{n}_h \cdot \boldsymbol{l}) - \omega_e\, \boldsymbol{n}_e\, (\boldsymbol{n}_e \cdot \boldsymbol{l}) + \tau\, (\boldsymbol{l} \times \boldsymbol{p}) \right] = 0. \tag{2.17}$$

2.1.2 Antiferromagnetic oscillator

AFM materials having a natural frequency in the THz range allow them to be used to create very fast devices. Extensive research has been conducted on FM layered structures driven by STT induced by a DC spin current, leading to the development of Spin-Torque Nano-Oscillators (STNOs) and Spin-Hall Nano-Oscillators (SHNOs) with AC signals in the frequency range of 1–30 GHz [78]–[84]. Recently, theoretical considerations have emerged regarding the utilization of AFMs in nano-oscillators to generate THz signals [21]–[25]. Here, we discuss the mathematical model describing the AFM oscillator that forms the basis of this dissertation.

In traditional FM oscillators, STT involves a DC current polarized parallel to the equilibrium magnetization direction to counteract damping. However, in AFMs, STT would diminish damping in one magnetic sublattice but increase it in the other, resulting in a net zero effect. In response, studies have indicated that STT acting perpendicular to

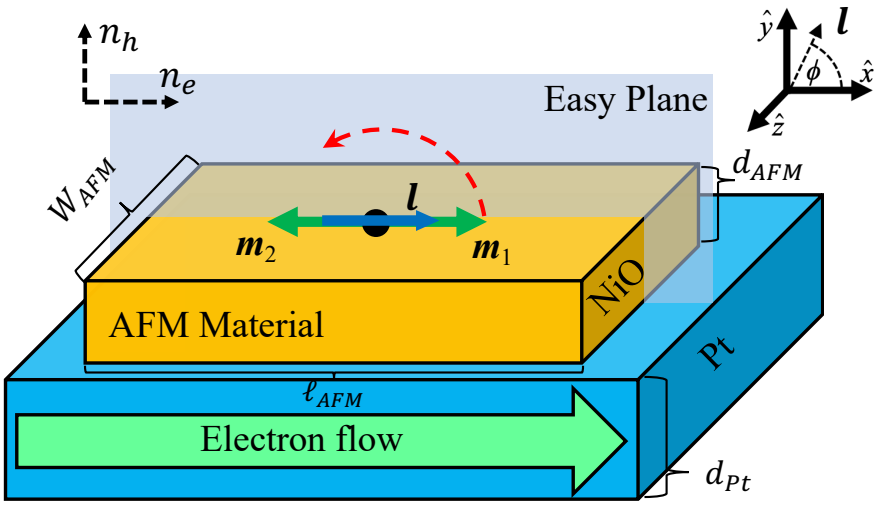

Figure 2.4: AFM oscillator. The electric current is flowing through the Pt. When the NiO easy plane is oriented, as shown in this figure, the electric current creates a torque on the AFM that causes $\boldsymbol{m}_1$ and $\boldsymbol{m}_2$ to rotate. Rotation in the easy plane is shown by a dashed red arc.

the sublattices can induce instability in sublattice orientation, leading to magnetization rotation in a plane perpendicular to the direction of the applied polarized spin current [85]–[87].

In 2017, Khymyn et al. proposed a simple structure in which an AFM material is layered on top of a heavy metal for the creation of a THz-frequency signal generator [21]. This configuration can be seen in Fig. 2.4. When an electric current flows through the Platinum (Pt) layer in the geometry depicted in Fig. 2.4, a spin current, polarized perpendicular to the easy plane, is injected into the AFM material via the spin-Hall effect [88], [89]. The spin current induces a rotation of the AFM sublattices in the easy plane by STT. The biaxial anisotropic nature of NiO results in a dual anisotropy in the form of an easy axis, $\boldsymbol{n}_e$, and a hard axis, $\boldsymbol{n}_h$, shown in Fig. 2.4. During the rotation of the sublattices, the Néel vector traverses the easy axis easier than the hard axis due to the increased

anisotropy, resulting in a non-uniform rotational speed of the magnetization. This non-uniform rotation generates a spin-pumping signal back into the Pt layer, producing an AC spin current detectable through the inverse spin-Hall effect.

To more clearly understand the dynamics of the AFM oscillator, it would be helpful to describe the rotation of the sublattices through the angle ϕ, the azimuthal angle between the Néel vector $\boldsymbol{l}$ and the easy axis (shown in the coordinate axis at the top right corner of Fig. 2.4). To achieve this, we move to a spherical coordinate system by rewriting the Néel vector as,

$$\boldsymbol{l} = \sin\theta\,\cos\phi\,\boldsymbol{x} + \sin\theta\,\sin\phi\,\boldsymbol{y} + \cos\theta\,\boldsymbol{z}. \tag{2.18}$$

Using this, the σ model, Eq. (2.17), is rewritten as two scalar equations for θ and ϕ. To simplify the derivations, we assume $\boldsymbol{p} = \boldsymbol{z}$ (the spin current is polarized along the $\boldsymbol{z}$ axis), $\boldsymbol{n}_e = \boldsymbol{x}$, and $\boldsymbol{n}_h = \boldsymbol{z}$ [21];

$$\frac{\dot{\theta}\dot{\phi}}{\omega_{ex}}\sin 2\theta + \sin^2\theta\left[\frac{\ddot{\phi}}{\omega_{ex}} + \alpha\dot{\phi} + \frac{\omega_e}{2}\sin 2\phi - \tau\right] = 0, \tag{2.19}$$

$$\frac{\ddot{\theta}}{\omega_{ex}} + \alpha\dot{\theta} - \frac{\sin 2\theta}{2}\left[\frac{\dot{\phi}^2}{\omega_{ex}} + \omega_e\cos^2\phi + \omega_h\right] = 0. \tag{2.20}$$

The ground state of the AFM corresponds to the sublattices lying in the easy plane or $\theta = \pi/2$. This solution must lead to a stable solution to Eq. (2.20). We can solve Eq. (2.20) for a small deviation in θ such that $\theta = \frac{\pi}{2} + \delta\theta$:

$$\frac{\delta\ddot{\theta}}{\omega_{ex}} + \alpha\delta\dot{\theta} + \frac{\delta\theta}{2}\Omega = 0, \tag{2.21}$$

where:

$$\Omega = \frac{\dot{\phi}^2}{\omega_{ex}} + \omega_e\cos^2\phi + \omega_h. \tag{2.22}$$

In Eq. (2.22), Ω depends on ϕ. However, the hard axis anisotropy, ω_h, is positive and much greater than other terms in Eq. (2.22), which implies that Ω is also positive and can be assumed to be independent of ϕ.

With a positive Ω, Eq. (2.21) takes the form of a linear equation with constant coefficients, and its stability can be determined by finding its eigenvalues,

$$\lambda_{1/2} = \frac{1}{2}\left[-\alpha\ \omega_{ex} \pm i\ \sqrt{\omega_{ex}}\ \sqrt{2\ \Omega - \alpha^2\ \omega_{ex}}\right]. \tag{2.23}$$

The real part of the eigenvalues, $-\alpha\omega_{ex}$, is negative, suggesting a stable solution around the ground state. This allows us to use $\theta = \pi/2$ in Eq. (2.19) to obtain a single equation describing the rotation of the Néel vector:

$$\frac{1}{\omega_{ex}}\ddot{\phi} + \alpha\dot{\phi} + \frac{\omega_e}{2}\sin 2\phi = \sigma I, \tag{2.24}$$

where I is the electric current density in the Pt layer, and σ is the spin-torque efficiency [85], [86] which has the form,

$$\sigma = \eta\frac{|\gamma|}{M_s\ d_{\mathrm{AFM}}\ w_{\mathrm{AFM}}\ d_{\mathrm{Pt}}}, \tag{2.25}$$

where γ is the gyromagnetic ratio, M_s is the saturation magnetization of one NiO sublattice, d_{AFM} is the thickness of the NiO, w_{AFM} is the width of the NiO/Pt interface, d_{Pt} is the thickness of the Pt, and η is a constant to be discussed in Chapter 3 [21]. These physical dimensions are shown in Fig. 2.4. Equation (2.24) is a well-known equation describing a particle in a tilted washboard potential and is analogous to a model of the superconducting phase of a Josephson Junction that is capacitively shunted under a bias current [90], [91].

For sufficiently large currents, the AFM sublattices lose their stability and start to rotate. The electric current that drives the oscillations must overcome a threshold value

proportional to the easy plane anisotropy:

$$I_{\text{th}} = \frac{\omega_e}{2\sigma}. \tag{2.26}$$

Above the threshold current, the angle ϕ increases in time as the sublattices continuously rotate around the direction of spin current polarization, resulting in an auto-oscillatory regime. The key feature is that the rotation is not uniform in time due to the easy plane anisotropy. This leads to an AC generation frequency,

$$\omega_{gen} = 2\frac{\sigma I}{\alpha}. \tag{2.27}$$

It should be noted that the frequency generated by the AFM oscillator does not depend on AFMR frequencies but instead on the ratio of STT and damping. The frequency ω_{gen} can be tuned from almost 0 to several THz using current densities $I \sim 10^8\ A/cm^2$ [21].

The rotation of the AFM sublattices causes a spin-pumping effect, wherein the rotation of the Néel vector influences the state of the adjacent metal layer. The non-uniform rotation generates a spiking spin-pumping signal emitted from the AFM. The signal is proportional to the velocity of the angle ϕ and is detectable as a voltage through the inverse spin-Hall effect. This is the output signal of the AFM oscillator and is given by the simple equation:

$$v(t) = \beta\dot{\phi}(t), \tag{2.28}$$

where $v(t)$ is a time dependent voltage, and β is the spin pumping efficiency which has the form,

$$\beta = \eta\frac{\ell_{\text{Pt}}}{d_{\text{Pt}}}, \tag{2.29}$$

where d_{Pt} is the thickness of the Pt layer and ℓ_{Pt} is the length of the NiO/Pt interface [21]. Later, it will be discussed how this spin pumping signal can be used as the output of a spiking artificial neuron.

2.2 Neuromorphic computing

This chapter will now transition between the fields of spintronics and neuromorphic computing to sufficiently establish the motivation of this interdisciplinary work. Despite decades of continuous technological advancements, recent progress has encountered a notable slowdown due to a fundamental challenge: the hardware's inability to keep pace, especially in the rising field of AI.

The history of AI traces back to the 1950s when British mathematician Alan Turing posed the fundamental question, "Can machines think?" [92]. Since its inception, AI has been a focal point of research spanning fields from computer science to linguistics. Over the past decade, AI has gained widespread attention and is now integral to applications ranging from image recognition and self-driving vehicles to medical sciences [93], [94]. However, this rapid progress has revealed an issue that demands resolution for sustained growth. Mainly, AI running on existing hardware is unsustainable [95].

The digital computers that are the backbone of our society run on what is known as Von Neumann architecture, illustrated by Fig. 1.1 [6], [7]. In this framework, machine instructions and data are stored together in memory, while computation occurs separately on a CPU. This architecture necessitates constant data transfers between memory and the CPU during processing, prolonging computation time and diminishing energy efficiency. AI, relying on extensive data for predictive modeling, demands substantial energy and time when operating within the confines of Von Neumann architecture. It becomes evident that a revolutionary shift in computation methods is imperative for the continued advancement of AI [95].

In response to the limitations imposed by Von Neumann architecture, many have turned to biology for inspiration in finding a solution. The human brain, recognized as the most energy-efficient processor, can execute intricate analyses with a power consumption of less than 20 W [8]. The key distinction lies in the brain's absence of separate memory and computational elements. This has prompted exploration into how in-memory technologies can enhance the shortcomings of Von Neumann architecture [96], [97].

The human brain consists of an estimated 100 billion nerve cells called neurons, which communicate through over 100 trillion connections known as synapses [98]. Information is processed as neurons transmit signals through synaptic connections, with the strength and number of these connections determining the outcome of computation. Unlike Von Neumann architecture, the brain stores memory locally within the neurons and synapses. This localized memory storage enables the brain to perform computations at high speeds, with energy efficiency far surpassing modern computers. Neuromorphic computing is the study of systems that emulate the brain's computational processes, aiming to create processors that are both high-speed and low-power [99], [100].

2.2.1 Artificial neural networks

Drawing inspiration from the intricate network of neurons and synapses found in the human brain, neuromorphic computing leverages ANNs as the foundation for computational models. In ANNs, artificial neurons act as individual nodes, mirroring their biological counterparts, and activate based on a nonlinear activation function. These artificial neurons simulate the behavior of biological neurons, responding to input signals and producing output signals that contribute to the overall computation. Artificial synapses within ANNs function as weights, defining the strength and characteristics of connections between artificial neurons. These synaptic weights are adjustable and play a crucial role in the network's learning process. The connections between neurons in ANNs

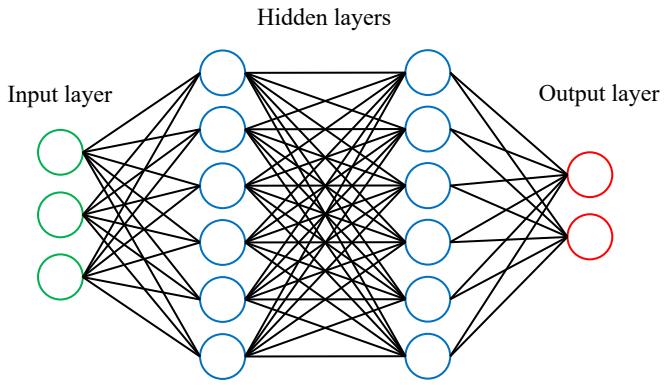

Figure 2.5: The typical structure of an ANN. Colored circles represent artificial neurons connected by artificial synapses indicated by black lines.

allow for the transmission of information, much like the synaptic connections in biological neural networks.

Architecturally, ANNs are organized into layers of artificial neurons, with these layers interconnected through artificial synapses. The arrangement of these layers and the interconnectivity between neurons within and across layers determine the network's structure and functionality. This layered structure facilitates the hierarchical processing of information, where input data is transformed through successive layers to produce the final output. This concept is illustrated in Fig. 2.5, which visually depicts the layered structure of ANNs, showcasing the interconnected nodes and the adjustable weights associated with the artificial synapses. ANNs have gained prominence for their ability to adapt and learn from data, making them a fundamental component in neuromorphic computing and AI.

To achieve the desired output, the ANN undergoes a process known as training, during which the synaptic weights are adjusted [9], [101], [102]. The extent of these adjustments is determined by various machine learning algorithms, which broadly fall into two categories: supervised learning and unsupervised learning [103], [104]. The primary distinction lies in whether the training data is labeled.

In supervised learning, the training dataset is labeled, with each input associated with its corresponding desired output [105], [106]. This approach is commonly employed for classification tasks, where the network learns to distinguish between different classes. For example, in image recognition, supervised learning could be used to classify pictures of cats and dogs. On the other hand, unsupervised learning operates on unlabeled data, seeking to discover underlying patterns in large datasets [107]. Algorithms in this category are adept at identifying hidden structures and relationships within data without explicit guidance.

One of the widely adopted supervised learning algorithms is backpropagation [108]–[110]. In the backpropagation process, a signal traverses the entire ANN, and an error is computed by comparing the actual outputs (y) with the target outputs (t). An example of such an error function is the commonly used squared error, formulated as,

$$E = \frac{1}{2}\sum_i (y_i - t_i)^2 . \tag{2.30}$$

Subsequently, the process of gradient descent is employed to determine the adjustments needed in the synaptic weights (W_{ij}) between neuron i and neuron j [111], [112]. Gradient descent aims to minimize the error function, representing the difference between actual and desired outputs. As the outputs of an ANN are a function of its inputs, taking the derivative of this function provides the slope or gradient. In the gradient descent algorithm, weights are adjusted proportionally, with a learning rate (η), to the negative of the gradient,

$$\Delta W_{ij} = -\eta \frac{\partial E}{\partial W_{ij}}. \tag{2.31}$$

Following the calculation of weight adjustments, the synapses are updated, starting from the output layer and propagating backward through the ANN. This sequential adjustment process is aptly named backpropagation. The iterative application of

backpropagation refines the network's synaptic weights, gradually improving its ability to accurately predict outputs for a given set of inputs.

ANNs appears to offer a promising solution to the challenges faced by AI on existing hardware. Many ANNs have demonstrated remarkable success in developing AI systems. In 1996, IBM utilized ANNs to create Deep Blue, a supercomputer that achieved victory against world chess champions [13]. In 2015, AlphaGo, another supercomputer based on ANNs, beat a world champion at the game GO, considered one of the most formidable challenges for AI to master [14], [15]. More recently, in 2023, OpenAI introduced ChatGPT-3, a large language model in the form of a chatbot. ChatGPT relies on an ANN with an extensive architecture featuring 175 billion neurons and synapses [10], [11].

Despite the achievements of AI systems operating on ANNs, a notable concern remains regarding energy efficiency. Deep Blue consumed 2-3 kW of power, while AlphaGo required a substantial 1 MW. Even the most modern AI example, ChatGPT, necessitates up to 10 GWh of energy during training [12]. These instances of ANNs illustrate the success of AI systems but underscore the ongoing challenge of achieving energy efficiency comparable to the human brain.

2.2.2 Spiking neural networks

Although ANNs draw inspiration from the brain, they lack many key features that make the biological neural networks unique. For example, in the brain, biological neurons use voltage spikes, called action potentials, whose profile is depicted in Fig. 2.6(a), to communicate with each other [113]. In contrast, artificial neurons in traditional ANNs do not spike; instead, they are active or inactive based on a non-linear function, such as the ReLu function illustrated in Fig. 2.6(b). Recognizing these distinctions has prompted the development of SNNs designed to emulate the brain more closely, addressing common challenges encountered with ANNs [114]–[117].

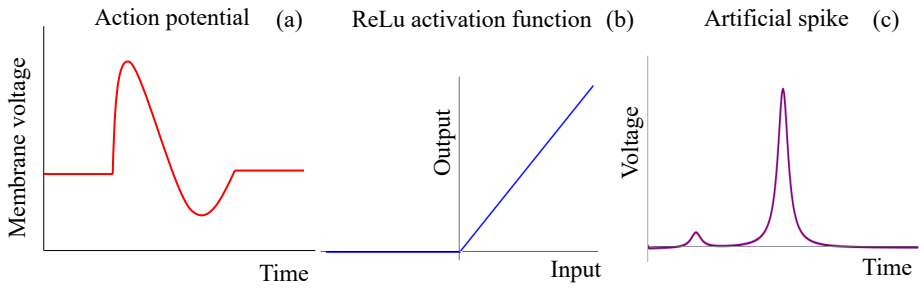

Figure 2.6: Output profile of different types of neurons. (a) Spike profile of biological action potentials. (b) Example of an activation function used by non-spiking artificial neurons. (c) Example of the spike profile of spiking artificial neurons.

The basic building block for SNNs are the artificial neurons that communicate through spikes, similar to the profile shown in Fig. 2.6(c). Spiking artificial neurons share three key similarities with their biological counterparts. First, they process information from multiple inputs and generate either none, a single, or a train of spikes as output. Second, their firing probability increases with excitatory input and decreases with inhibitory inputs. Lastly, their internal dynamics are characterized by a threshold state, where a spike is produced only after reaching the threshold [117]. Through spike-based communication, mirroring the brain's approach, SNNs exhibits lower energy consumption compared to traditional ANNs.

In 1952, Hodgkin and Huxley developed a mathematical model for the generation of action potentials in biological neurons [118]. This model has since served as a foundation for various spiking artificial neuron models. Among these models, the most fundamental is the Integrate and Fire (IF) neuron, distinguished by its approach to processing input. In IF neurons, a single spiking input might not be sufficient to surpass the internal threshold value for firing. However, a sequence of below-threshold inputs are cumulatively summed, triggering a firing event once the threshold is reached. An

extension of this model is the Leaky Integrate and Fire (LIF) artificial neuron, which shares similar behavior with the added feature of a leaky function. This function diminishes the internal value of the neuron in the absence of inputs, mirroring how biological neurons dissipate internal energy during the intervals between inputs [119], [120].

Although SNNs have many advantages compared to ANNs, a significant challenge persists. Due to SNNs encoding and transmitting information through undifferentiable spikes, conventional ANN training methods utilizing gradient descent cannot be directly applied. Consequently, the development of new learning algorithms becomes imperative for training SNNs.

One notable algorithm addressing this challenge is Spike-Time-Dependent Plasticity (STDP), an unsupervised learning algorithm inspired by biological synapses [121], [122]. The principle behind STDP is grounded in the observation that biological synapses strengthen when the pre-synaptic spike precedes the post-synaptic spike within a specific time window and weaken in the opposite scenario [123], [124]. Equation (2.32) depicts the experimentally observed STDP learning rule [125]:

$$\Delta w = \begin{cases} A\, e^{\frac{(t_{pre}-t_{post})}{\tau}} : t_{pre} - t_{post} \leq 0,\ A > 0 \\ B\, e^{\frac{-(t_{pre}-t_{post})}{\tau}} : t_{pre} - t_{post} \geq 0,\ B < 0 \end{cases}, \tag{2.32}$$

where Δw is the change in weight, A and B are constants, τ is the timing window constant, and t_{pre} and t_{post} are the timing of the pre- and post-synaptic spikes, respectively. Through STDP, SNNs establish connections that represent patterns in the data. However, a limitation of STDP lies in its performance within multilayer networks, as it strictly applies to a single layer and its previous layer without communication to another part of the network.

In an alternative approach, inspired by the success of backpropagation in training ANNs, efforts have been made to adapt it for SNNs. One of the earliest adaptations is SpikeProp and its variants [126]–[128]. Similar to other supervised learning algorithms, SpikeProp minimizes the error between desired and actual outputs. To implement gradient descent on undifferentiable spikes, SpikeProp employs temporal encoding, where the discrete timing of a spike is used to implement a cost function similar to Eq. (2.30),

$$E = \frac{1}{2}\sum_{j}\left(t_j^a - t_j^d\right)^2, \tag{2.33}$$

where t_j^a is the actual firing time of neuron j and t_j^d is the desired or target firing time. Weight adjustments are then calculated using the same gradient descent function, Eq. (2.31), as backpropagation. SpikeProp has demonstrated success in classifying the XOR problem using temporally encoded spikes and a three-layered SNN [126].

In 2021, Intel unveiled its Loihi 2 neuromorphic chip, a SNN comprising 1 million LIF neurons interconnected by 120 million synapses. The advantages of SNNs are evident, with Intel reporting a power consumption of 20 pJ per operation in just 3.5 ns [16], [17]. While this serves as a notable example of how SNNs represents the next generation of ANNs, a few drawbacks persist. To accommodate its 1 million neurons and 120 million synapses, the Loihi 2 chip relies on 2.3 billion CMOS transistors. This implies that multiple transistors are needed to create a single spiking artificial neuron or synapse. The necessity for more than one hardware element for each node in the neural network significantly amplifies power and area requirements.

2.3 Spintronic neuromorphic computing

Finally, this section will make the connection between spintronics and neuromorphic computing to set up the theme of this dissertation. In recent years, numerous research groups have harnessed spintronic concepts for neuromorphic computing [18]–[20], [129]–[131]. The utilization of spintronic devices in the

construction of artificial neurons and synapses offers three key advantages over their traditional transistor-based counterparts. Firstly, spintronic devices can be engineered at the nanometer scale, significantly diminishing the area requirements for all sizes of ANNs. Secondly, a single spintronic device has the potential to serve as a standalone artificial neuron or synapse, not only reducing area requirements but also lowering overall power consumption. Lastly, spintronic devices leverage spin-dependent effects for operation, typically demanding less energy than CMOS technology. Several spintronic devices have already demonstrated the ability to generate nanosized, energy-efficient artificial neurons and synapses.

One can imagine a spin valve structure consisting of an FM "free layer", capable of freely rotating its magnetization, and another FM "pinned layer", where the magnetization is fixed. This arrangement forms a Magnetic Tunnel Junction (MTJ), which many have used for spintronic neuromorphic computing. MTJs exhibit a threshold operation akin to the threshold potential in biological neurons. In 2016, Sengupta et al. [132] demonstrated the creation of a LIF neuron using an MTJ. They illustrated how an MTJ can integrate a series of spin current pulses, and upon reaching a threshold value, the stochastic switching of the free layer simulates the firing of a neuron. Subsequent works utilized the switching nature of MTJs to construct LIF neurons and ANNs capable of neuromorphic benchmark tasks, such as pattern recognition [133], [134]. However, these designs necessitated an additional applied current to reset the MTJ neuron back to the ground state, introducing extra energy requirements. In 2023, Wang et al. [135] proposed a LIF MTJ-based neuron with a self-reset function, eliminating the need for an external reset current. Despite this advancement, these LIF neurons still lack certain features of biological neurons. In the same year, Rodrigues et al. [136] introduced a single MTJ spiking neuron exhibiting features analogous to biological neurons. Their device demonstrated a spike profile similar to biological neurons, along with refractory periods

essential for SNN training. A neural network composed of these MTJ spiking neurons successfully performed pattern recognition tasks.

Another direction in spintronic neuromorphic computing employs magnetic DWs, which are a mobile interface between opposing magnetization directions within a magnetic material. The position of the DW can be manipulated along a device by applying either a current or spin-orbit torque, a phenomenon previously employed for Boolean logic operation [137]. Numerous research groups have integrated DW motion with MTJs to develop devices with artificial neuron capabilities [138]–[142]. In 2016, Sengupta et al. [141] proposed an all-spintronic ANN wherein both the neurons and synapses relied on DW motion. For the synapses, the position of the DW beneath an MTJ determined the ratio of parallel and anti-parallel states, with the equivalent conduction of the MTJ serving as the synaptic weight. Their DW artificial neurons exhibited integrate-and-fire functionality, where the DW is moved along a track towards a sensing MTJ. The resistance of the MTJ flips as the DW passed underneath it, resulting in a firing event. However, the DW neurons used in their all-spin neural network lacked the leaky feature found in biological neurons. In 2019, Bringer et al. [142] proposed a LIF DW neuron that used shape-based anisotropy to exhibit the leaky nature. The trapezoidal shape of the FM track results in an increase in DW energy with position, dependent on shape anisotropy. Consequently, the DW exhibits leaky behavior as it moves backward to minimize its energy between integrating pulses. In 2018, Hassan et al. [140] proposed a different LIF DW neuron that relied on a nearby FM, creating a magnetic field to push the DW backward. Their design also enabled the DW neuron to exhibit lateral inhibition, a characteristic of biological neurons where the activity of nearby neurons affects each other.

Magnetic skyrmions are quasi-particle chiral spin textures found in magnetic materials that have garnered attention for their potential application in neuromorphic

computing due to their nano-scale size and high-speed motion with a low current density [143]. Several groups have proposed LIF artificial neurons based on the motions of skyrmions [144], [145]. In these designs, skyrmions integrate input current, moving along a track where the width changes with length. This alteration in track width induces a change in the perpendicular magnetic anisotropy experienced by the skyrmions, resulting in a pushback effect that produces the leaky behavior. In 2022, Liu et al. [146] proposed a skyrmion-based SNN where both the neurons and synapses relied on skyrmion motion. They report that their skyrmion SNN boasts all the advantages of spintronic-based neuromorphic computing while achieving reduced area requirements and increased energy efficiency compared to a CMOS design.

Section 2.1.2 mentions much work has been done studying FM oscillators, and many groups have used these devices for neuromorphic computing. These nano-sized devices use STT or spin-Hall effects to achieve oscillations in the GHz range. STNOs are spintronic devices structurally similar to MTJs comprising a pillar with two FM layers separated by a non-magnetic spacer. When a current passes through the pillar, it generates a torque on the magnetization, resulting in magnetization precessions at frequencies ranging from hundreds of megahertz to tens of gigahertz [62], [147]. In 2017, Torrejon et al. [148] proposed the use of STNOs for neuromorphic computing. They assert that STNOs have two fundamental properties needed for artificial neurons: nonlinearity and memory. Their proposal involves a STNO radio frequency neuron that takes in time-dependent current and performs computation through the resulting amplitude of oscillations. Since 2017, they have implemented their radio frequency neurons in hardware and in the creation of multilayered neural networks [149], [150]. Similar to STNO, SHNOs induce oscillations in an FM layer via the spin-Hall effect [80], [151], [152]. In 2020, Zahedinejad et al. [153] demonstrated that the mutual synchronization of an array of SHNOs can be leveraged for neuromorphic vowel recognition. The

oscillations of an SHNO can also be harnessed to create spiking artificial neurons, as shown by Manna et al. [154] and Markovic et al. [155].

As the popularity of AFMs grows, AFM spintronic devices have found applications in the realm of spintronic neuromorphic computing. Some groups employ DWs in AFMs to emulate LIF neurons [156], [157]. Similar to the use of FM DW motion for LIF neurons, the position and movement of the AFM DW demonstrate the leaky and integrated behavior characteristic of artificial neurons. Other studies use the combination of AFM materials and skyrmions to engineer artificial neurons [158], [159]. While skyrmion motion on FM tracks exhibits drawbacks, such as uneven trajectories and the risk of annihilation at track edges due to a perpendicular force from the driving current, these issues are notably absent in skyrmion motion within AFM materials. Researchers harness these features to develop AFM skyrmion spiking neurons, both with and without a leaky nature.

2.3.1 Antiferromagnetic neurons

While some groups have begun integrating AFM devices into spintronic neuromorphic computing, none have fully harnessed the potential of AFM materials' THz dynamics. The AFM SHNO, detailed in section 2.1.2, introduces a novel, simplistic device capable of ultra-fast nonlinear dynamics. These distinctive attributes position it favorably for utilization as an artificial neuron in neuromorphic computing applications.

One can consider a scenario in which a subcritical DC current, $I < I_{\text{th}}$, drives an AFM oscillator causing the sublattices to remain stationary. To induce rotation, an additional modulated current is introduced in combination with the DC current, expressed as,

$$I = I_{dc} + i_{ac} \sin(2\pi f_{ac} t), \tag{2.34}$$

where I_{dc} is the amplitude of the DC component of the applied current, i_{ac} is the amplitude of the AC component of the applied current, and f_{ac} is the frequency of the AC component [160]. When the combined current momentarily surpasses the threshold for oscillations, I_{th}, the AFM sublattices undergo a singular rotation. Through spin-pumping, a brief burst of electric voltage emanates from the AFM via the inverse spin-Hall effect and is detected through Eq. (2.28) [161], [162].

Simulations of the inputs and outputs to this AFM SHNO can be seen in Fig. 2.7. Figure 2.7(a) shows the input driving current with a DC component fixed below the threshold $I_{dc} < I_{dc}^{\text{th}}$. At the low values of the AC current amplitude i_{ac} the oscillator does not produce a significant output signal (Fig. 2.7(b)). With the increase of the i_{ac}, at some point when the combined amplitude exceeds a generation threshold $I_{dc} + i_{ac} = I_1^{\text{th}}$, the device generates a single sharp spike of a significant amplitude during each period of applied AC current, (Fig. 2.7(c)). The well-defined threshold value for i_{ac} required for spike generation in the AFM oscillator mirrors how biological neurons respond to an external stimulus exceeding a threshold, producing voltage spikes known as action potentials [113]. The voltage spikes produced by the AFM oscillator, seen in Fig. 2.7(c), exhibit a similar profile to biological action potentials. Because of the THz dynamics inherent to AFM materials, these spikes exhibit widths on the scale of a few picoseconds, operating on a timescale significantly faster than any existing artificial neuron design. Further increasing i_{ac}, can lead to a double switch of the AFM sublattices per one period of the AC driving current, resulting in a burst of multiple spin-pumping spikes, as shown by Fig. 2.7(d). This bursting effect is a known feature of biological neurons.

Given these notable similarities, it can be asserted that an AFM oscillator, governed by,

$$\frac{1}{\omega_{ex}}\ddot{\phi} + \alpha\dot{\phi} + \frac{\omega_e}{2}\sin 2\phi = \sigma I, \tag{2.24}$$

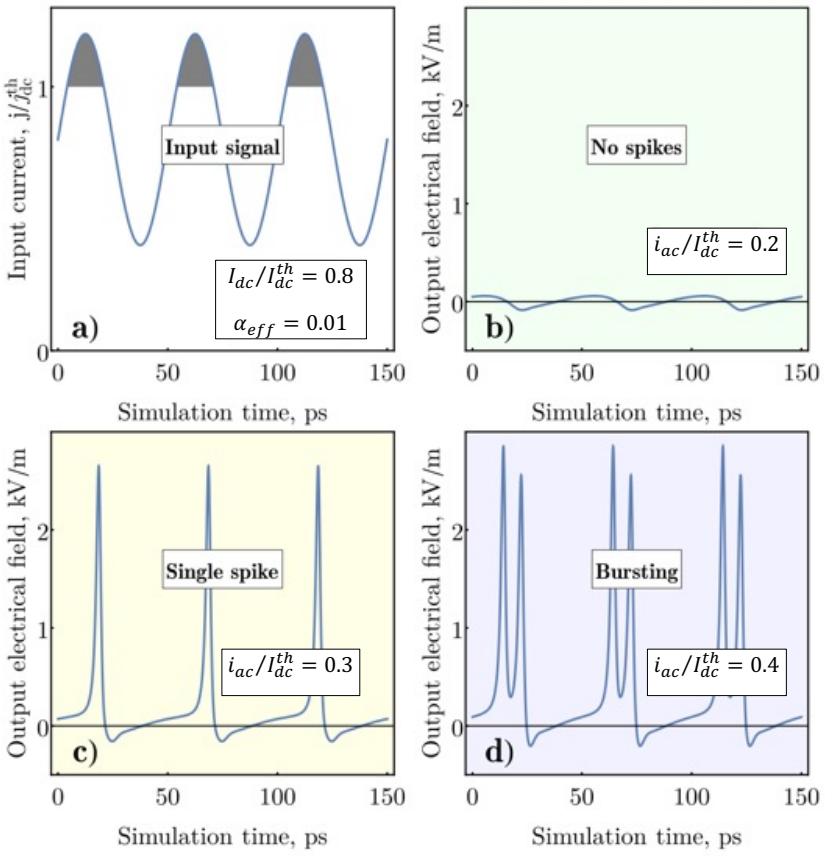

Figure 2.7: Simulation results of an AFM SHNO at different regimes. (a) The shape of the combined DC and AC input current. (b) The output of the AFM SHNO for a 'low' value of AC current results in no spike generation. (c) Single spike output of AFM SHNO with one spike per period of 'moderate' AC driving current. (d) Bursting effect of AFM SHNO resulting in multiple spike generation during each period of 'high' AC driving current. Figure reproduced from R. Khymyn, I. Lisenkov, J. Voorheis, O. Sulymenko, O. Prokopenko, V. Tiberkevich, J. Akerman, and A. Slavin, Scientific Reports, 8, 1–9 (2018); licensed under a Creative Commons Attribution (CC BY) license.

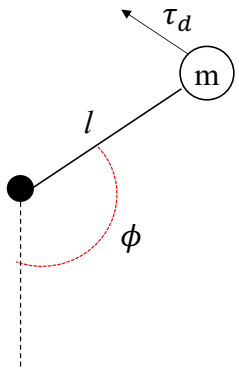

Figure 2.8: Simple pendulum as a mechanical analog of an AFM neuron. The mass m is affixed at a distance l from an axis, and is displaced from vertical by an angle ϕ. The mass is subject to an external driving torque τ_d.

and driven by a sub-threshold current, functions as an artificial neuron. The THz dynamics of AFM materials contribute to spikes generated by the "AFM neuron" being on the order of picoseconds, surpassing the typical spike width of both biological neurons and other artificial neurons. Equation (2.24) will henceforth be referred to as the "AFM neuron equation".

To gain a better understanding of the AFM neuron equation, Eq. (2.24), a remarkable analogy can be made with a mechanical pendulum illustrated in Fig. 2.8 and described by the equation,

$$I_m\ddot{\phi} + b\dot{\phi} + mgl\sin\phi = \tau_d. \tag{2.35}$$

By comparing this equation with Eq. (2.24), it is evident that this system is analogous to that of an AFM neuron. Therefore, it is useful to describe each term in this equation individually in order to gain a better understanding of this system.

The first term on the left-hand side of Eq. (2.35), $I_m\ddot{\phi}$, contains the moment of inertia. The moment of inertia describes how difficult it is to change the angular velocity of an object rotating about an axis. When comparing the mechanical analog in Eq. (2.35)

with the AFM neuron equation Eq. (2.24), it is evident that the first term on the left-hand side of Eq. (2.24) models the inertia of the system. This implies that $(1/\omega_{ex})$ is analogous to the moment of inertia. Thus, the exchange interaction in the AFM material leads to the AFM neuron having an effective inertia. This effective inertia is one of the factors that make AFM neurons unique, giving AFM neurons properties like response latency and a finite refraction time, which will be detailed in Chapter 3.

The second term on the left-hand side of Eq. (2.35), $b\dot{\phi}$, represents the damping due to friction experienced by the pendulum. Friction acts to slow any movement by the pendulum. The magnitude of b determines how much friction is present. By comparison with the AFM neuron equation, the second term on the left-hand side of Eq. (2.24), $\alpha\dot{\phi}$, represents damping. When the sublattices, $\boldsymbol{m}_1$ and $\boldsymbol{m}_2$, have a non-zero angular velocity, $\dot{\phi}$, damping will slow this rotation. The magnitude of α determines how much damping is present in this system. The damping acts like a frictional force to slow the rotation of the sublattices, similar to the damping in a pendulum. For the AFM neuron, α is a property of the AFM material and, to a certain extent, can be controlled in fabrication.

The third term on the left-hand side of Eq. (2.35) is $mgl\sin\phi$. This is the gravitational potential for the pendulum. This potential defines a preferable orientation (i.e., anisotropy) of the pendulum and governs how the velocity of the mass will change as it revolves around the axis. Likewise, the third term on the left-hand side of Eq. (2.24), $(\omega_e/2)\sin 2\phi$, models the anisotropy of the AFM material. This anisotropy governs how the velocity of $\boldsymbol{m}_1$ and $\boldsymbol{m}_2$ will change as it rotates. It is notable that ω_e, the easy axis anisotropy frequency, is present in this term. When $\boldsymbol{m}_1$ and $\boldsymbol{m}_2$ are rotated under the action of the external spin current, the anisotropy of the AFM acts to realign $\boldsymbol{m}_1$ and $\boldsymbol{m}_2$ with the easy axis.

Finally, the term on the right-hand side of Eq. (2.35), τ_d, is the externally applied driving torque to the pendulum. When in motion, this torque acts to increase the angular

velocity. Likewise, in the model of the AFM neuron, the term on the right-hand side of Eq. (2.24) represents the STT applied by the spin current to $\boldsymbol{m}_1$ and $\boldsymbol{m}_2$ in the AFM neuron. STT is analogous to the driving torque in the pendulum. The STT depends on the current $I = I_{\mathrm{dc}} + i_{\mathrm{ac}}(t)$ that flows through the Pt substrate. Here, I_{dc} is a bias current that brings the angle of the magnetization to an initial angular displacement, and $i_{\mathrm{ac}}(t)$ represents a momentary perturbation, that incites the magnetization to rotate.

The AFM neuron equation, Eq. (2.24), is a well-known equation describing an inertial particle in a tilted washboard potential. It also exactly takes the form of the equation describing the superconducting phase in a resistively and capacitively shunted Josephson junction under a current bias [163]. In the AFM oscillator, the role of energy stored in the capacitor is played by the exchange energy, while the role of resistance is played by the Gilbert damping. Therefore, a number of effects observed in Josephson junction oscillators at cryogenic temperatures are observed with room temperature AFM oscillators.

The magnitude of the bias current determines the regime in which the AFM neuron is operating. That is, if the bias current exceeds a threshold current I_{th} described by Eq. (2.26), the system will behave as an auto-oscillator, with magnetization $\boldsymbol{m}_1$ and $\boldsymbol{m}_2$ continually rotating in the easy plane. For this system to be in the neuronal regime and thus exhibit behavior like that of a typical biological neuron, it is required that the bias current be sub-threshold, $I_{\mathrm{dc}} < I_{\mathrm{th}}$.

AFM neurons represent a significant advancement in spintronic neuromorphic computing, offering a novel device with numerous benefits. The straightforward design of the AFM SHNO facilitates the easy fabrication of AFM neurons. Moreover, leveraging the THz properties of AFM materials, AFM neurons exhibit ultra-fast dynamics, evident by their picosecond spike widths. This unique combination of simplicity and speed results in remarkably low energy consumption per operation. This dissertation will explore the

functionality of AFM neurons and their applications in neuromorphic computing. Ultimately, AFM neurons propel the field of spintronic neuromorphic computing forward, paving the way for ultra-fast and energy-efficient computing in the future.

CHAPTER THREE

BASIC DYNAMICAL PROPERTIES OF AFM NEURONS

This chapter will take the AFM neurons first introduced in section 2.3.1 and detail their dynamics not covered in previous works. A schematic diagram of a nanometer-sized, single-element artificial AFM neuron is shown in Fig. 3.1(a). In this figure, the AFM material is shown in yellow and is in contact with a metallic electrical conductor, shown in blue. The metallic conductor acts as a terminal for the AFM neuron, with an input and an output. When an electrical current, made up of a DC bias current and an input current impulse, passes through the conductor (Fig. 3.1(b)), the AFM material will respond by generating a short-duration voltage spike, as shown in Fig. 3.1(c). This output spike is similar to an action potential that is generated by a biological neuron, allowing this AFM oscillator to function as an artificial neuron. It is evident from this figure that a characteristic output spike for an AFM neuron is quite fast, with a duration of ≈ 3 ps. This high speed, which is faster than other artificial neurons, is a direct result of the intrinsic THz properties of the AFM material.

As will be shown in this chapter, there are several distinct advantages of AFM neurons over the currently employed silicon-based alternatives. Firstly, AFM neurons exhibit biologically realistic characteristics, including refraction, latency, and bursting, all of which can be controlled dynamically. Secondly, the duration of spikes is in the picosecond timescale, allowing for an operational speed that is substantially faster than conventional computers. Thirdly, this device requires several orders of magnitude less power to operate than the state of the art. Fourthly, as this artificial neuron consists of a single element, it has the potential to greatly simplify the design and fabrication stage of manufacture. Moreover, the spatial dimension is on the nanometer scale so that they can,

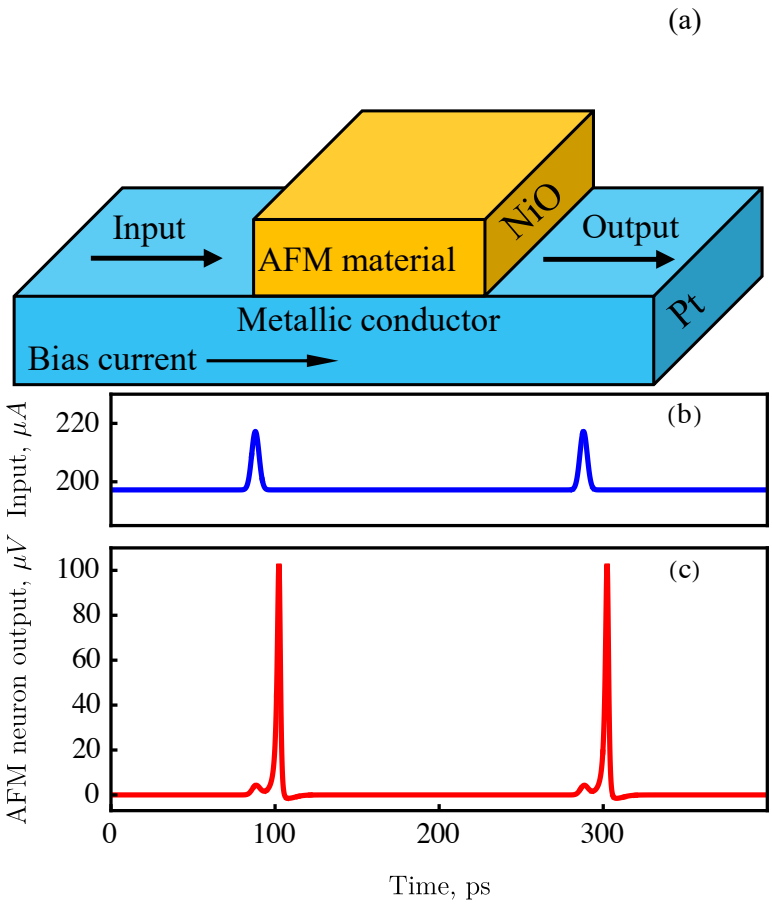

Figure 3.1: AFM neuron. (a) A cartoon of the AFM neuron, which consists of an AFM material and a metallic conductor. The input and output of the neuron are labeled. (b) Simulated input current supplied to the AFM neuron. Bias current is $\sim 198\ \mu$A; with input impulses just before 100 ps and 300 ps. (c) Simulated output spikes from an AFM neuron in response to the input, at 100 and 300 ps. In this simulation, $\alpha = 0.009$.

in principle, be included with integrated circuits that use CMOS technology [164]. Lastly, AFM neurons operate at room temperature and, when interconnected, will allow the development of physical spiking neural networks.

This chapter starts by thoroughly examining the physical parameters used in the simulations forming the basis of this dissertation. It then goes deeper, taking a closer look at the terms in the AFM neuron equation derived in section 2.1.2. The unique characteristics of a single AFM neuron are discussed, including aspects like bursting, refraction, and polarity. After that, it explores the dynamic outcomes when multiple AFM neurons are connected in chains, both with symmetric and asymmetric coupling. The results discussed in this chapter were previously presented in paper [26] and conference presentation [34].

3.1 Physical implementation and simulation parameters

As shown in section 2.3.1, an AFM oscillator governed by the AFM neuron equation, which we repeat here for convenience,

$$\frac{1}{\omega_{ex}}\ddot{\phi} + \alpha\dot{\phi} + \frac{\omega_e}{2}\sin 2\phi = \sigma I, \tag{2.24}$$

can serve as an artificial neuron. A summary of material parameters related to the AFM neuron equation and the output equation, repeated here for convenience,

$$v(t) = \beta\dot{\phi}(t), \tag{2.28}$$

are given in Table 3.1. Many of the values in this table are the same as those presented in an earlier work [21] and are specific for an AFM neuron composed of a NiO/Pt bilayer. It should be noted, that I_{th}, Eq (2.26), is proportional to the easy plane anisotropy ω_e and, thus, depends on the in-plane anisotropy of the AFM material. It is possible, in principle, to decrease I_{th} by reducing the anisotropy field by Voltage-Controlled Magnetic Anisotropy (VCMA) or by using magnetoelastic interactions. Similar effects might be

Table 3.1: AFM material parameters, fundamental constants, and physical dimensions used in simulations, unless otherwise noted.

Parameter	Description	Simulation value
ω_{ex}	Exchange frequency	$2\pi \times 27.5$ THz
ω_{e}	Easy axis anisotropy frequency	$2\pi \times 1.75$ GHz
ω_{h}	Hard axis anisotropy frequency	$2\pi \times 43.9$ GHz
α	Effective damping	0.1
$\lvert\gamma\rvert/2\pi$	Gyromagnetic ratio	28 GHz/T
M_s	Saturation magnetization	351 kA/m
θ_{SH}	Spin Hall angle	0.1
g_r	Spin mixing conductance	6.9×10^{18} m^{-2}
e	Elementary charge	1.6×10^{-19} C
λ	Pt spin diffusion length	7.3 nm
ρ	Resistivity of Pt	4.8×10^{-7} Ω·m
d_{AFM}	NiO thickness	5 nm
w_{AFM}	NiO/Pt interface width	10 nm
ℓ_{AFM}	NiO/Pt interface length	40 nm
d_{Pt}	Pt thickness	20 nm
η		5.4×10^{-17} V·s
σ	Spin-torque efficiency	27.1×10^{12} rad/A·s
β	Spin pumping efficiency	0.11×10^{-15} V·s
I_{th}	Threshold current	0.203 mA

achieved by interfacial Dzyaloshinskii-Moriya field present at the AFM-heavy metal interface. Complete elimination of I_{th}, however, is not possible since the operation of AFM neuron relies on anisotropic angular dependence of the AFM potential energy.

The constant η, present in σ the spin-torque efficiency Eq. (2.25), and β the spin pumping efficiency Eq. (2.29), is given by

$$\eta = \left[\theta_{\text{SH}} \frac{g_r e \lambda \rho}{2\pi}\right] \tanh \frac{d_{Pt}}{2\lambda}, \tag{3.1}$$

where θ_{SH} is the spin Hall angle, g_r is the spin mixing conductance, e is the magnitude of the fundamental electric charge, λ is the spin-diffusion length in Pt, and ρ is the resistivity of thin film Pt [21].

It should be noted in Eqs (2.24) and (2.28), that by increasing the values of η, σ, and β, the performance of the AFM neuron will be improved. Therefore, the performance characteristics of the AFM neuron depend on the physical dimensions of the AFM neuron; specifically, d_{AFM}, w_{AFM}, and d_{Pt}. For example, in Eq. (2.25), the value of σ increases for small values of d_{AFM} and w_{AFM}. Therefore, we have chosen $d_{\mathrm{AFM}} = 5$ nm and $w_{\mathrm{AFM}} = 10$ nm as simulation parameters. These values are small, yet reasonable for nano-fabrication.

Likewise, d_{Pt} appears in Eqs (2.25), (2.29), and (3.1). To maximize η, a thickness with $d_{Pt} > 2\lambda$ should be chosen. However, a thin d_{Pt} is beneficial to maximize σ and β. Taking this into consideration, $d_{Pt} \sim 20$ nm was chosen as a simulation parameter. This thickness is reasonable for nano-fabrication.

The size of the entire structure must be considered for the choice of ℓ_{AFM}, the length of the NiO/Pt interface. The NiO material should be small enough that its entire volume is in a uniform ground state; that is, it should be a single crystal with a single domain, and without any domain walls. In addition, the volume of the AFM material should be large enough that the magnetization will not spontaneously rotate in the easy plane due to thermal energy. The energy required for thermal noise to rotate the magnetization is equal to $V_{\mathrm{AFM}} B_e M_s$, where V_{AFM} is the volume of the AFM material and $B_e = \omega_e/|\gamma|$ is the easy axis anisotropy field. The thermal energy is equal to $k_B T$, where k_B is the Boltzmann constant and the temperature is $T = 300$ K. Thus, a reasonable volume would be $V_{\mathrm{AFM}} > 10(k_B T/B_e M_s)$, which corresponds to an AFM material with a volume of $V_{\mathrm{AFM}} \sim 2000$ nm^3. For our chosen d_{AFM}, this corresponds to a NiO/Pt interface with a surface area of 400 nm^2. This surface area is on par with the size of

CMOS transistors. With this surface area, and w_{AFM} defined above, it is appropriate to use a simulation parameter for the length of the NiO/Pt interface as $\ell_{\mathrm{AFM}} = 40$ nm.

With these size parameters, the spin torque efficiency is approximately $\sigma = 27.1 \times 10^{12}$ rad/A·s, and the spin pumping efficiency is $\beta \sim 0.11 \times 10^{-15}$ V·s/rad. Considering that a typical value for $\dot{\phi}$ is about 1 rad/ps, we can assume that all together, voltage spikes produced by an AFM neuron will have a magnitude on the order of $\beta\dot{\phi} \approx 100\ \mu$V, with a duration as short as 1 ps. Also, with this σ, the threshold current is $I_{\mathrm{th}} \sim 0.2$ mA.

The effective damping α for NiO can vary between 0.001 and 0.1. Damping in NiO depends on the technology of film preparation, and therefore there is some flexibility in how α can be varied in simulation. Smaller damping parameters lead to a shorter spike duration.

It is important to note that AFM neurons require a DC electric current I_{dc} to be constantly flowing through the Pt substrate. The purpose of this current, as stated earlier, is to bias the magnetization so that ϕ_0 is close to ϕ_{th}, so it can generate a spike with the receipt of a small current impulse $i_{\mathrm{p}}(t)$. The energy consumption of an AFM neuron can be estimated by considering I_{dc}. Previously, it was estimated that a current near the threshold bias current of $I_{\mathrm{th}} = 0.2$ mA would be required to drive the rotation of $\boldsymbol{m}_1$ and $\boldsymbol{m}_2$. If the resistance of the platinum beneath the NiO is given by $R_{\mathrm{pt}} = \rho\ell_{\mathrm{AFM}}/d_{\mathrm{Pt}}w_{\mathrm{AFM}}$, then the power consumption of this structure can be estimated as $I_{\mathrm{th}}^2 R_{\mathrm{Pt}} \sim 4$ µW. If the time per synaptic operation is conservatively estimated as 100 ps, the energy consumption of a single AFM neuron is $\sim 10^{-3}$ pJ per synaptic operation. This power consumption can be compared with other spiking neuromorphic hardware [165]. For example, the energy per synaptic operation for the Intel Loihi Neuromorphic Chip was reported to be 20 pJ [166] while another all CMOS artificial neuron reports an energy consumption of 247 pJ [167]. The energy consumption of AFM neurons is even below the consumption of other

spintronic artificial neurons. For example, a STNO artificial neuron reports an energy consumption of 4.96 pJ per synaptic operation [168]. The efficiency of an AFM neuron can be evaluated in units of SOPS/W, where SOPS stands for synaptic operations per second [169]. Using this measure, a single AFM neuron will have a performance of 10 TSOPS and an efficiency of about 2500 TSOPS/W, which far more efficient than comparable systems reported in Ref. [169]. The high efficiency of AFM neurons is a direct result of its high speed of operation, which is a result of the high exchange frequency of NiO and other AFM materials. Please note that these efficiency estimates are for the AFM neurons only, and do not include the power consumed by support circuitry or by interconnections between the neurons.

It is worth noting that platinum was chosen for simulations because it is relatively straightforward to fabricate and has an acceptable spin Hall angle $\theta_{SH} \sim 0.1$. However, it may be possible to employ a topological insulator with a much higher spin Hall angle, for example $\theta_{SH} \sim 50$ for BiSb [170]. The use of a material with a higher spin Hall angle will greatly improve the power efficiency of this system. For example, use of material with $\theta_{SH} \sim 10$ will decrease power consumption to $\sim 10^{-7}$ pJ per synaptic operation and, at the same time, increase output spike amplitude to ~ 10 mV.

At present, AFM neurons have not yet been fabricated. The reason relates to the difficulty in fabricating an insulating structure with nanometer dimensions. To function properly, the AFM structure should be fabricated with several important characteristics. As previously mentioned, the structure should be large enough so that the magnetization will not rotate spontaneously due to thermal noise, but small enough that it is monocrystalline and of a single domain. Additionally, the easy plane anisotropy in the AFM film must be oriented correctly with respect to the Pt film plane, and a clean interface between the substrate and the AFM material is required for an efficient interfacial effect. These technical challenges will need to be overcome prior to the

experimental demonstration of an AFM neuron. However, we believe that the performance of this system justifies expanded research in this area. In addition, it has been suggested that a neuron with properties similar to an AFM neuron can be constructed from a magnetic tunnel junction using available fabrication technology [171], [172].

Since the AFM neurons have not yet been realized experimentally, the configuration of support circuitry has yet to be determined. In addition, the presence of defects and other noise sources will require attention in the design of support circuitry to allow the propagation of spiking signals. Thus, details about integration with CMOS or other technologies will not be addressed in this dissertation.

3.2 Single AFM neuron behavior

This section discusses the dynamic behavior of an AFM neuron that is modeled by Eq. (2.24). It will begin by demonstrating the spiking behavior of an AFM neuron by numerical simulation. After this, the refractory properties of AFM neurons are discussed, as will the response of AFM neurons to polarity changes.

3.2.1 AFM neuron spiking demonstration

Together, Eqs (2.24) and (2.28) describe the input-output behavior of an AFM neuron; the input is the current I and the output is the voltage $v(t)$. In most cases, there is no general analytical solution; thus Eq. (2.24) can only be solved numerically.

Numerical simulations of Eqs (2.24) and (2.28) were performed to demonstrate an AFM neuron generating spikes. Results of these simulations are shown in Fig. 3.2. The simulations were performed with a bias current of $I_{\mathrm{dc}} = 198$ μA, which is 5 μA below the threshold current $I_{\mathrm{th}} = 203$ μA. As mentioned earlier, I_{th} is the threshold current that determines when the AFM neuron is in the neuronal regime ($I_{\mathrm{dc}} < I_{\mathrm{th}}$), and when it behaves as an auto-oscillator ($I_{\mathrm{dc}} > I_{\mathrm{th}}$).

The input to the AFM neuron, current impulse $i_p(t)$, is shown in Fig. 3.2(a). In this simulation, $i_p(t)$ has four peaks. The threshold current $i_{\mathrm{th}} = I_{\mathrm{th}} - I_{\mathrm{dc}}$ which is 5 μA

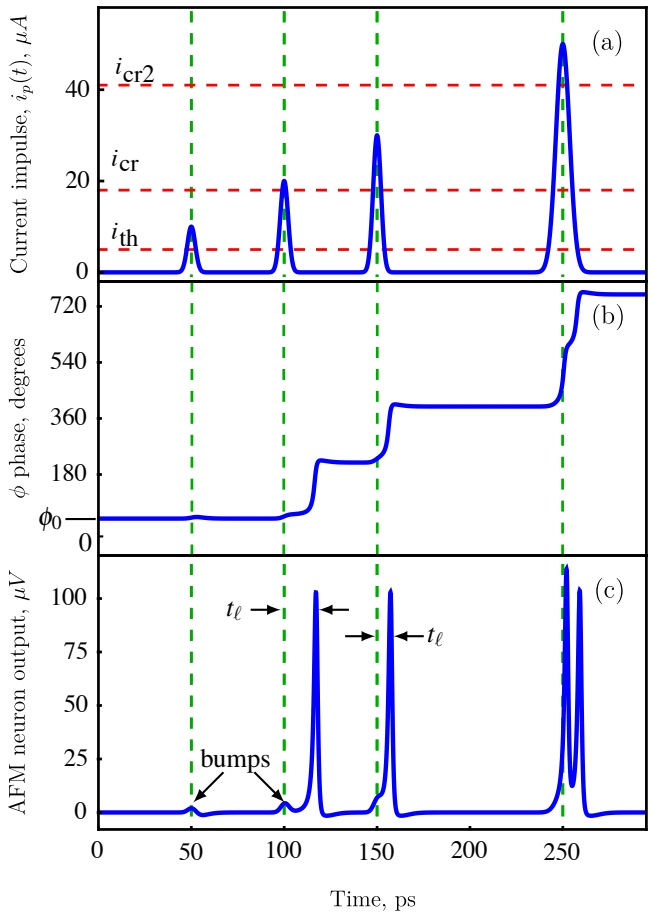

Figure 3.2: Input current and simulated AFM neuron output. (a) The simulated input current. The blue curve represents the input current $i_p(t)$, the lower dashed red line represents the threshold current i_{th}, the center red dashed line represents the critical current, i_{cr}, and the top red dashed line represents the critical current for bursting behavior, i_{cr2}. (b) The simulated azimuthal angle ϕ of the Nèel vector $\boldsymbol{l}$ in the easy plane, shown in the coordinate axis at the top right corner of Fig. 2.4. Green vertical dashed lines show the time of input perturbations. (c) Voltage output of the AFM neuron. The latency t_ℓ for two spikes is labeled. In this simulation, $\alpha = 0.009$.

above the bias current, is represented in the figure by a red dashed line. Note, that the *threshold* current i_{th} is the input signal amplitude that leads to magnetization rotation in the DC regime, i.e., for a *very long* duration of the input signal. To induce rotation with a *short* input pulse, its amplitude should exceed a certain *critical* value i_{cr}, which depends on the input duration, and for the parameters of Fig. 3.2, equals $i_{\text{cr}} = 18$ μA. For further increase of the input current amplitude ($i_p > i_{\text{cr2}} = 41$ μA), one input pulse will generate burst spikes, as explained below. The four input pulses in Fig. 3.2(a) have different amplitudes: one is below the critical current ($i_{\text{th}} < i_p < i_{\text{cr}}$), two pulses of different amplitudes in the range $i_{\text{cr}} < i_p < i_{\text{cr2}}$, and the last spike in the burst range $i_p > i_{\text{cr2}}$.

Figure 3.2(b) and (c) show the response of the AFM neuron to the current impulse. Figure 3.2(b) shows the azimuthal angle ϕ of the Nèel vector $\boldsymbol{l}$, and Fig. 3.2(c) shows the output voltage according to Eq. (2.28). It is evident from this figure that for the first 50 ps, in the absence of a current impulse, that ϕ remains constant, and thus $\dot{\phi} = 0$. The output voltage, which is proportional to $\dot{\phi}$, remains at zero during this interval.

At $t = 50$ ps, there is a current impulse with an amplitude of 10 μA. This impulse is larger than i_{th} but is is less than i_{cr}. Because the impulse is less than the critical current, the magnetization does not rotate, and there is no output spike. This current impulse, however, does cause a small movement in the Néel vector $\boldsymbol{l}$, as can be seen in the small bump at $t = 50$ ps in Fig. 3.2(c).

Next, at $t = 100$ ps, there is a current impulse of 20 μA which exceeds i_{cr}. The response to this input current impulse consists of, first, a small bump at $t = 100$ ps (see Fig. 3.2(c)). Then, after a delay of $t_\ell \sim 10$ ps, the neuron fires. This can be seen at time $t = 110$ ps in the 180° rotation of ϕ in Fig. 3.2(b), and in the voltage spike in Fig. 3.2(c).

The behavior of the AFM neuron at $t = 100$ ps demonstrates two properties that closely resemble the behavior of biological neurons. Firstly, AFM neurons follow the "all-or-nothing" law [173]. That is, these neurons only fire when they receive sufficient

stimulus. Biological neurons only elicit action potentials when the membrane potential rises above a threshold, which then depolarizes the neural membrane. In the AFM neuron, this is equivalent to the input current being momentarily larger than the critical current.

Secondly, concerning the delay t_ℓ. In biological neurons, this delay is called the *neuronal response latency*, which is the time between the input stimulus and the activation potential [174]. In AFM neurons, the delay is due to the time it takes for the magnetization to rotate past the threshold angle. Visualized as a simple pendulum shown in Fig. 2.8, the perturbation provides just enough energy for ϕ to pass ϕ_{th} or 180°. However, the velocity will be very slow as ϕ approaches the critical angle as it works against the gravitational force, or in the case of an AFM neurons, the anisotropy. Then, once ϕ is past ϕ_{th}, the mass will accelerate. In the pendulum model, this latency is due to the inertia in the mechanical system. The latency in AFM neurons is a direct result of the effective inertia that comes from the exchange energy acting as an effective mass in the AFM neuron equation, Eq. (2.24).

The duration of the response latency depends on the magnitude of the input impulse. This is demonstrated by the response of the AFM neuron at time $t = 150$ ps. At this time, the current impulse is 30 μA, which is larger than the previous spike. Once again, the AFM neuron magnetization rotates by 180°, as shown in Fig. 3.2(b), and the rotation brings about a voltage spike, as shown in Fig. 3.2(c). Please note that this voltage spike has the same amplitude and duration as the previous voltage spike. However, the response latency has a shorter duration because the AFM neuron received a larger input current impulse. A shorter latency can also be achieved by increasing the value of the driving DC current, I_{dc}. This would bring the AFM magnetization closer to the threshold value I_{th}. This illustrates how the dynamics of an AFM neurons is analogous to any system with inertia. The rate at with the magnetization travels through the anisotropic potential is dependent on the strength of the driving force and the additional stimulus.

Lastly, consider the behavior of the AFM neuron at $t = 250$ ps. At this time, the momentary increase in the instantaneous electric current is larger than i_{cr2}. When the electric current is larger than i_{cr2}, the AFM neuron will exhibit bursting behavior. This can be seen in Fig. 3.2(c), where the AFM neuron shows a double peak, and in Fig. 3.2(b), where $\boldsymbol{l}$ rotates by 360°, twice as much as for the previous two impulses. In biological neurons, this behavior is also known as bursting [175]–[179].

Above, we illustrate the response of AFM neurons to a realistic spiking signal, akin to those that propagate within AFM neural networks. Previously, a similar investigation examined the effect of sinusoidally modulated bias current [160], which is detailed in section 2.3.1, which is more relevant to utilizing AFM oscillators for signal processing rather than AI applications. The findings reported in Ref. [160], replicated in this thesis, demonstrate AFM behavior consistent with the observations presented above. For AFM neurons, $i_{\mathrm{cr}} \neq i_{\mathrm{th}}$; thus, it is expected that a change in the relative magnitudes of I_{dc} and $i_{\mathrm{p}}(t)$ will lead to different behaviors. This is demonstrated in Fig. 3.3, which was made via simulation with a sinusoidal input for $i_{\mathrm{p}}(t)$ and a bias current I_{dc} [160]. The axes are scaled as a ratio of $I_{\mathrm{dc}}/I_{\mathrm{th}}$ and $i_{\mathrm{p}}(t)/I_{\mathrm{th}}$. In this figure, there are three regions: single spike (red), bursting (blue), and no spikes (yellow). The boundary between the red and yellow regions represents the critical current i_{cr}, which is the minimum current impulse required to generate a spike. The boundary between the generation of single spiking signals and bursting signals, i_{cr2}, corresponds to a line between the red and blue regions. Additionally, there is a dashed line in the yellow region, which represents the threshold current $i_p = i_{\mathrm{th}} = I_{\mathrm{th}} - I_{\mathrm{dc}}$ for very long pulses. One noteworthy characteristic in this plot is that as I_{dc} decreases, the separation between i_{cr} and i_{th} increases, and there is an increased range where single spiking signals can occur.

It can also be seen from Fig. 3.3 that when $I_{\mathrm{dc}} > I_{\mathrm{th}}$, the AFM magnetizations will rotate more than once. In this regime, AFM neurons are capable of generating a

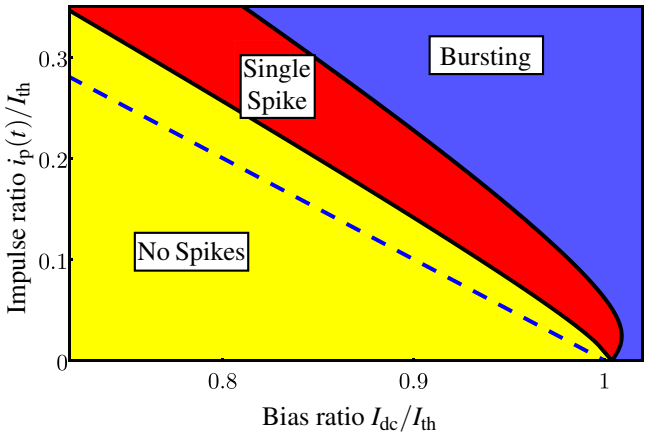

Figure 3.3: AFM neuron spike characteristics. For the yellow region, the AFM neuron produces no spikes. In the red region, the AFM neuron generates a single spike. In the blue region, the AFM neuron exhibits bursting behavior. The behavior depends on the relative values of $i_p(t)$ and I_{dc}. In this simulation, $\alpha = 0.01$. Figure reproduced from R. Khymyn et al., Scientific Reports, 8, 1–9 (2018) and H. Bradley et al, AIP Advances, vol. 13, no. 1, p. 015 206, Jan. 2023, licensed under a Creative Commons Attribution (CC BY) license.

continuous train of spikes that has a frequency that depends on the amplitude of I_{dc}. Interestingly, biological neurons subject to sustained suprathreshold stimuli will also elicit a train of action potentials whose frequency depends on the strength of the stimulus [178], [180]. Biological neurons can exhibit adaptation in spike trains; they feature a change in the duration of interspike intervals. They can also exhibit stuttering, which are spike trains with inconsistent rhythms [178]. AFM neurons can also exhibit adaptation by tuning the bias current and can exhibit stuttering with the introduction of noise to the bias current. For both types of neurons, the characteristics of the superthreshold spike generation are dependent on the size and variation of the stimulus.

3.2.2 AFM neuron refraction

Due to the effective inertia modeled by the first term in the AFM neuron equation Eq. (2.24), AFM neurons intrinsically exhibit refraction, a property that will be explored in this subsection. This property, that bears close resemblance to the behavior of

biological neurons, is a positive attribute for AFM neurons. Refraction is not intrinsically present in CMOS spiking neurons, although it can be emulated [165].

In AFM neurons, there is a period of time when the AFM magnetizations are in the act of rotation, and the AFM neuron is unable to fire even if it receives an additional impulse $i_{\mathrm{p}}(t)$. In biological systems, this is called the *absolute refractory period*, which is defined as the time interval after the neuron fires where it cannot fire again [173]. There are also times when the AFM magnetizations are in the act of recovery, and the AFM neuron responds with modified behavior. In biological systems, this is generally called the *relative refractory period* [173]. These two refractory properties of an AFM neuron are demonstrated in Fig. 3.4, and will be discussed below.

The absolute refractory period will be considered first in Fig. 3.4(a). In this simulation, the first spike arrives at an AFM neuron at $t = 200$ ps, as shown by a red curve. After a latency of about 50 ps, the neuron fires, as shown by the green curve. Then, as shown by a blue curve, a second input spike arrives at $t = 302.3$ ps, 102.3 ps after the first spike. In this case, the second spike does not cause the AFM neuron to spike. This is because the AFM neuron is still within its absolute refractory period, and it is unable to fire a second time.

The simulation results in Fig. 3.4(b) demonstrates the relative refractory period of AFM neurons. In this case, a second input arrives at $t = 302.4$ ps, which is 102.4 ps after the first spike and 0.1 ps later than above. In this case, the AFM neuron generates a second spike after a latency of about 400 ps. Thus, during the relative refractory period, the AFM neuron can generate a spike, but with an extended latency.

A simulation showing the response of an AFM neuron without refraction is considered in Fig. 3.4(c). Once again, the first spike arrives at $t = 200$ ps and after a latency of about 50 ps, the neuron responds with a spike. The blue input then arrives at the AFM neuron at $t = 385$ ps, which is 185 ps after the initial input. Then, once again, after a

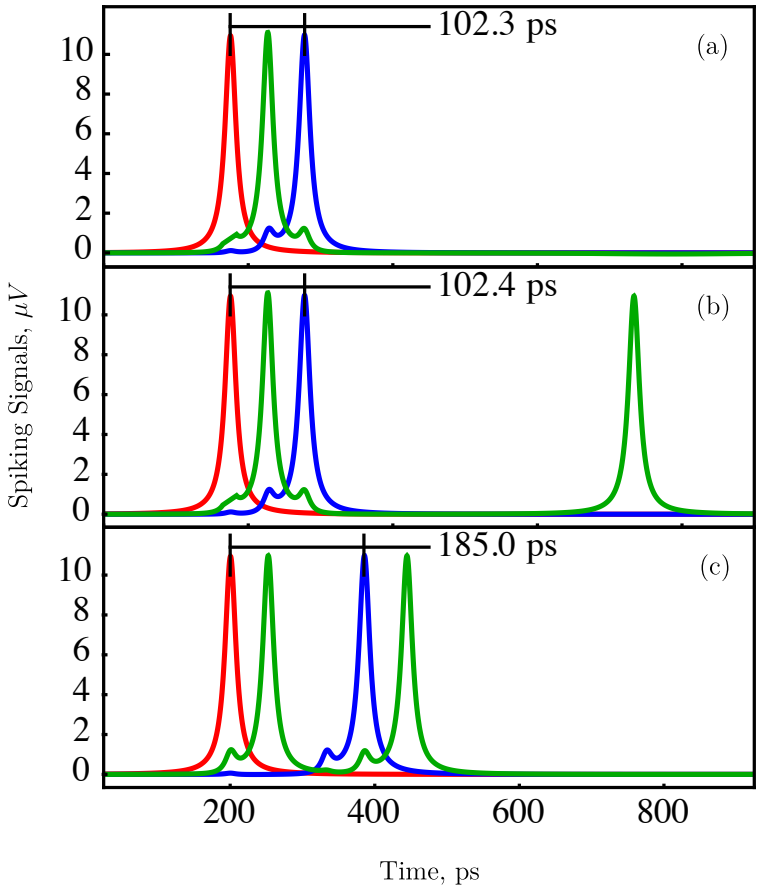

Figure 3.4: Simulation demonstrating the refractory period of the AFM neuron. For these simulations, inputs to the neuron are shown with red and blue curves, while the output of the neuron is shown with a green curve. (a) The red input spike leads to a green output spike with $t_\ell = 50$ ps. The blue input spike occurs after an interval of 102.3 ps, during the absolute refractory period. The neuron does not spike a second time. (b) The blue input spike occurs after an interval of 102.4 ps, during the relative refractory period. The second output spike occurs after a long delay. (c) The blue input spike occurs after an interval of 185 ps. The second output spike has the same latency as the first spike, because the AFM neuron is not in its refractory period.

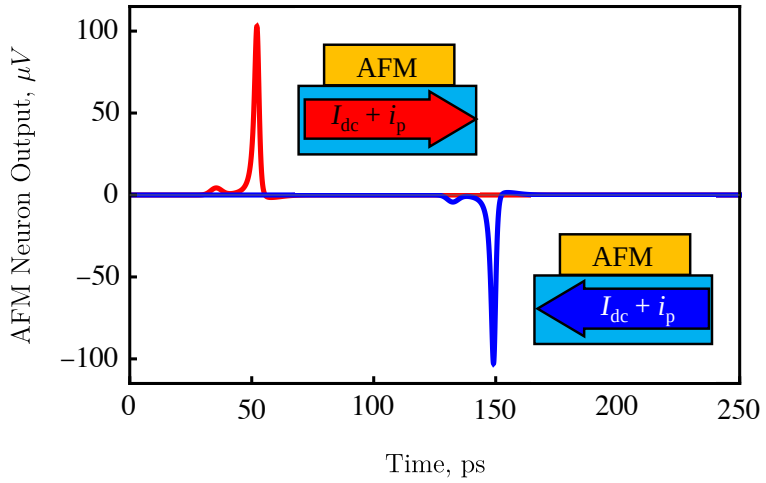

Figure 3.5: Reversible polarity of a single AFM neuron. The red curve shows the response of the neuron to a positive current that surpasses i_{cr}, while the blue curve shows the response of the same AFM neuron to a negative current that surpasses $-i_{cr}$. In these simulations, $\alpha = 0.009$.

latency of about 50 ps, the neuron fires, as is shown by a green curve. Please note that the latency responses for both inputs are the same. For the parameters simulated, 185 ps is the minimum time required for the AFM neuron to fire with the same latency.

The length of the refractory period of an AFM neuron can be dynamically controlled by changing the bias current I_{dc}. The refractory period also depends on the effective damping, the anisotropy, and the exchange frequency of the AFM material. Please note that for an AFM neuron with a lower damping parameter, the refractory time will be substantially shorter.

3.2.3 AFM neuron polarity

Interestingly, AFM neurons can also reverse their polarity; specifically, they can spike with both positive and negative voltages. This can be achieved by biasing an AFM neuron with DC currents of different polarity, which induces magnetization rotation in the opposite direction.

AFM neuron behavior for different bias polarities is illustrated in Fig. 3.5. Here red curves show responses of AFM neurons with positive current, and blue curves show the response of AFM neurons to negative current. It is evident from the figure that the polarity of AFM neuron spikes can be reversed in response to a change in current direction.

Unlike AFM neurons, biological neurons are unable to produce negative action potentials in response to negative stimuli. However, biological neurons can be inhibited by hyper-polarization stimuli [181]. A spike employing negative polarity to inhibit a neighboring neuron will be demonstrated in Chapter 4. The bipolar character of AFM neuron dynamics may find useful applications in developing new types of SNNs consisting of two competing subnetworks (positively and negatively biased). The neurons in one subnetwork will stimulate neurons in the same network, but inhibit neurons of the opposite network.

3.3 Interconnecting AFM neurons

For AFM neurons to be useful, they should be interconnected in neural networks. The previous sections described the behavior of individual AFM neurons. This section will discuss how multiple AFM neurons can be interconnected to form a physical neural network.

A summary of interconnection schemes is shown in Fig. 3.6. In Fig. 3.6(a), neurons ‘A’ and ‘B’ are connected by a single piece of platinum. With this connection, both neurons are subject to the same bias current. Likewise, spikes generated by neuron ‘A’, will travel downstream to induce a spike in neuron ‘B’.

A second simple method of interconnecting neurons is shown in Fig. 3.6(b). In this case, both AFM neurons are connected to separate Pt stips. This allows a bias current to be provided to each AFM neuron independently. A copper waveguide interconnects the neurons to transmit spin current between neurons ‘C’ and ‘D’. In Fig. 3.6(b), when neuron

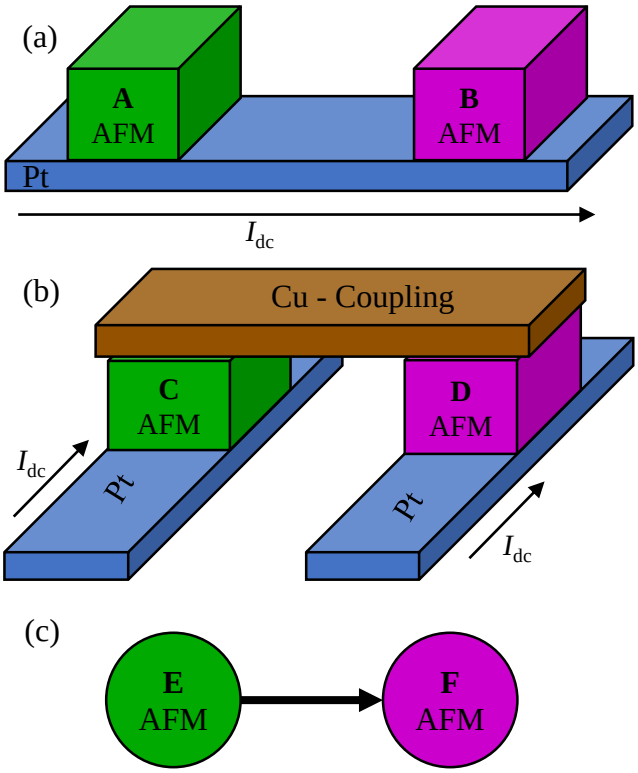

Figure 3.6: AFM neuron interconnection. (a) Schematic of electrical interconnection. Here, neuron 'A' is green and neuron 'B' is magenta, and the two neurons are connected via the blue platinum substrate. (b) Schematic of spin current interconnection. Here, neurons 'C' and 'D' are biased independently by two Pt substrates, and they are interconnected via a copper coupling waveguide, shown in brown. (c) Schematic of a generic interconnection. Neuron 'E' is represented by a green circle, and neuron 'F' is represented by a magenta circle. These two neurons are interconnected by a generic synapse, which is represented by an arrow.

'C' spikes, it generates a spin current that can flow into the copper connector and travel to neuron 'D'. If the spin current is of sufficient magnitude, it can induce neuron 'D' to generate a spike. In the scheme, there would be a delay as the spike of spin current produced by neuron 'C' travels down the copper waveguide to neuron 'D'. This synaptic delay of copper bridges can be found by solving the one-dimensional spin diffusion equation for spin accumulation in copper,

$$\frac{\partial \vec{s}}{\partial t} = -\frac{\vec{s}}{\tau_s} + D\frac{\partial^2 \vec{s}}{\partial x^2}, \tag{3.2}$$

where τ_s is the spin relaxation time and D is the diffusion constant [60]. The ansatz of $\vec{s} \approx e^{i\omega t + ikx}$ can be made to solve Eq. (3.2) with the real part of the solution, $k(\omega)$, describing the propagation of the spin current. The group velocity of the resulting spin wave takes the form,

$$\frac{1}{v_{gr}} = \frac{\partial k'}{\partial \omega}. \tag{3.3}$$

Therefore, the synaptic delay of the copper bridge is found from,

$$\tau_{delay} = \frac{L}{v_{gr}} = L\left(\frac{\partial k'}{\partial \omega}\right), \tag{3.4}$$

where L is the length of the copper between the two AFM neurons. By using the standard diffusion parameters for copper [182] and AFM neuron dimensions described in section 3.1, the synaptic delay for a copper bridge with a length of 100 nm is found to be about 1.5 ps. It is possible to change the coupling strength between the neurons by changing the width, thickness, and length of the copper waveguide.

The coupling configurations depicted in Fig. 3.6(a) and (b) establish connections between AFM neurons via physical waveguides. These waveguides facilitate spike transmission in the 'forward' direction (from neuron 'A'/'C' to neuron 'B'/'D'), enabling AFM neurons to trigger each other. However, such connections also facilitate spike

propagation in the 'backward' direction (from neuron 'B'/'D' to neuron 'A'/'C'), leading to bidirectional coupling. Further exploration of this bidirectional signal propagation will be conducted in a subsequent section.

Unfortunately, the strengths of the inter-neuron connections in Fig. 3.6(a) and (b) are fixed, and cannot be adjusted. To use AFM neurons in neural networks for machine learning and AI, it is required that the connection between neurons be mediated by an adjustable synapse. This is depicted schematically in Fig. 3.6(c). In this figure, both neurons are assumed to be properly biased with a DC current. When a momentary impulse of sufficient amplitude is applied to neuron 'E', it will generate a spike. This spike will travel through a synapse, which is represented in this figure by an arrow, to neuron 'F'. If the signal that arrives at neuron 'F' is of sufficient amplitude, neuron 'F' will also generate a spike.

All synapses simulated in this dissertation are assumed to be "ideal," meaning that the synaptic weights can be adjusted instantaneously and be of any value. This thesis is focused primarily on presenting AFM neurons as realizable hardware; thus, we do not go into the details of how synapses will be realized. It is worth mentioning that electrical synapses can be physically realized in different ways [99], for example, using memristors [183], multiferroic heterostructures [184], Josephson junctions [185], or even implemented in CMOS [186].

Artificial synapses can also be constructed using spintronic devices; i.e. devices that use magnetic elements and their dynamics. For example, STNOs [149], [187]–[189], domain walls [141], [190]–[193], and skyrmions [194]–[196] have all been shown to act like synapses to interconnect artificial neurons. Spintronic devices have many distinct advantages over their electrical counterparts, with an ability to closely resemble biological synapses with a low power consumption. Spintronic synapses have been shown to exhibit the potentiation and depression behaviors of biological synapses [194], [195], and also

shown to exhibit STDP, the biological process that adjusts the weights between neurons [190], [191].

3.3.1 Mathematical model for AFM neural networks

A mathematical model for a single AFM neuron was given by the AFM neuron equation, Eq. (2.24). In contrast, when multiple AFM neurons are interconnected into a neural network, the neurons will interact with each other via spiking output voltages. The interaction can be modeled by a system of differential equations:

$$\frac{1}{\omega_{ex}}\ddot{\phi}_i + \alpha\dot{\phi}_i + \frac{\omega_e}{2}\sin 2\phi_i = \sigma I_i + \sum_{i\neq k}\kappa_{ik}\dot{\phi}_k. \tag{3.5}$$

In this equation, i and k are indices that represent the i-th and k-th neuron, and κ_{ik} represents a matrix of coupling coefficients. Like all neural networks, we envision that the interaction between neurons will be mediated by synaptic weights. In this equation, synapses are represented by the coupling coefficients κ_{ik}. In a few words, by simulating Eq. (3.5), one can simulate an entire SNN of AFM neurons. It is hoped that, eventually, instead of simulations, fabricated AFM neurons will be available to perform computations at a picosecond timescale.

Equation (3.5) assumes that the timing delays related to the interconnections are negligible in comparison to the refractory period. From Eq. (3.4), the synaptic delay of a copper bridge is 1.5 ps and is clearly less than the refractory period of ≈ 100 ps discussed in section 3.2.2. Thus a synaptic delay is not included in the simulations of this dissertation. To simulate a system with delays, $\dot{\phi}_i$ would need to be modified.

3.3.2 Simple neuron chain

Simulations were performed on a chain of five interconnected neurons, as represented in Fig. 3.7(a). In this figure, five AFM neurons are represented by circles, and electrical connections with synapses are represented by arrows.

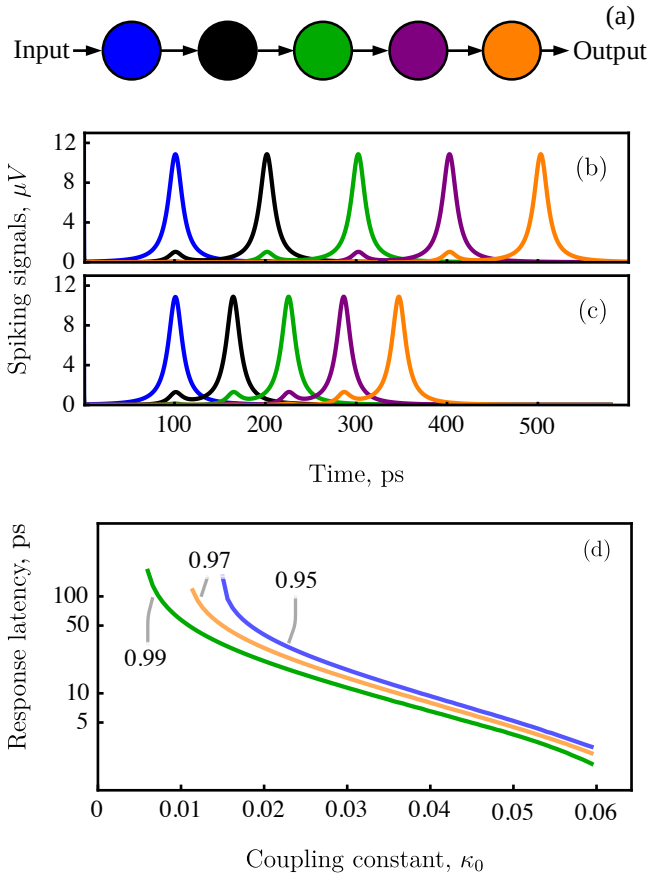

Figure 3.7: Simulation results for five AFM neurons connected in a sequential chain. (a) The neural network for a five-neuron chain. Circles represent AFM neurons, and arrows represent synapses. (b) Voltage output with $\kappa_0 = 0.011$. The color of each curve represents the voltage output of each neuron. (c) Voltage output with $\kappa_0 = 0.015$. (d) The relationship between κ_0 and response latency. Different colored lines show I_{dc}/I_{th} values of 0.99 (green), 0.97 (orange), and 0.95 (blue).

The neuron chain is intended to function as follows. First, there is a current impulse that originates on the left that will cause the magnetizations of the blue neuron to rotate and thus generate a voltage spike. The spike from the blue neuron then travels through a synapse to the black neuron, where it will have sufficient amplitude to cause the magnetization of the black neuron to rotate, and thus generate a voltage spike. After this, the spike from the black neuron will flow to the next neuron, thus continuing down the chain.

Numerical simulations were run for this system according to Eq. (3.5). In this simulation, every neuron is considered to have a damping constant of $\alpha = 0.1$ and a bias current of $I_{\rm dc} = 198\ \mu$A, which is $\sim 0.98 I_{\rm th}$. Weights in the synaptic connections are assigned to the matrix κ_{ik}, which in this case is a 5×5 coupling matrix given by:

$$\kappa_{ik} = \kappa_0 \begin{bmatrix} 0 & 0 & 0 & 0 & 0 \\ 1 & 0 & 0 & 0 & 0 \\ 0 & 1 & 0 & 0 & 0 \\ 0 & 0 & 1 & 0 & 0 \\ 0 & 0 & 0 & 1 & 0 \end{bmatrix}, \tag{3.6}$$

where κ_0 is the coupling constant that determines the overall strength of neuronal interconnects.

Consider first the simulation results with $\kappa_0 = 0.011$, shown in Fig. 3.7(b). For this simulation, a momentary stimulus is provided to the leftmost (blue) neuron, leading to a spike at time $t = 100$ ps, as can be seen from the blue curve in Fig. 3.7(b). The voltage produced by the blue neuron, which is about 10 μV, then causes the black AFM neuron to spike at $t = 190$ ps, as shown by the black curve. The spike from the black neuron, which has the same amplitude, continues towards the green neuron. This leads the green neuron to generate a spike, which then leads the purple and orange neurons to generate spikes in

succession. Thus, a spiking signal can propagate through a chain of interconnected neurons.

Note that in Fig. 3.7(b), there is a uniform time delay of about 90 ps between two neighboring neuron spikes. This delay is the neuron response latency t_ℓ which was discussed previously. As before, the duration of the latency can be adjusted by increasing the amplitude of the perturbation $i_p(t)$ that initiates the magnetization revolution in the AFM material. In a neural network, the amplitude of a spike incident on an AFM neuron can be changed by adjusting the value of the synaptic weight.

Thus, the duration of the response latency can be adjusted by changing the weights in the coupling matrix. Simulation results for a chain of neurons, with a larger synaptic weight, are demonstrated in Fig. 3.7(c). Here, the weights were changed to $\kappa_0 = 0.015$, while the bias current, the effective damping, and the coupling matrix, Eq. (3.6), remained unchanged. With the increased synaptic weights, the neurons fire as before, with a shortened latency of about 50 ps. The time between neuron spikes can thus be controlled by adjusting the synaptic weight. The relationship between synaptic weights and response latency may be useful in the implementation of machine learning algorithms for SNNs. Chapter 5 details one such learning algorithm used to train AFM neurons for pattern recognition.

Of course, the bias current also plays a role in determining the latency in a sequential chain of neurons. This is examined in Fig. 3.7(d). The figure shows how the latency and the coupling coefficient κ_0 are related, for three values of bias current $I_{\rm dc}/I_{\rm th}$. Two trends can be ascertained from this graph. First, for all three bias currents, as κ_0 increases, the latency decreases. Second, as the bias current increases, a smaller coupling constant is able to induce a shorter latency.

Thus, this section has established that AFM neurons can be interconnected and that spikes can be transmitted between neurons through these interconnections. It was also established that the weights can be used to change the response latency of neuron spikes.

3.3.3 Symmetric coupling

Interestingly, it is possible to transmit spin current directly between neurons with a non-magnetic metal like copper. This idea was illustrated schematically in Fig. 3.6(b). In that figure, when neuron 'C' spikes, it generates a spin current that can flow into the copper connector and travel to neuron 'D', which will, in turn, also produce a spike of spin current. However, with this simple waveguide, the spike generated by neuron 'D' can then re-enter the copper connector, and flow back to neuron 'C'. That is, the coupling between these two neurons is bi-directional; hence, this type of coupling can be called *symmetric coupling*. The concept of symmetric coupling in a system of bio-inspired neurons is novel; therefore, it will be considered in detail in this subsection.

Unfortunately, machine algorithms have not been developed that can use bi-directional signal propagation. Therefore, it will be beneficial if AFM neurons could be interconnected via symmetric coupling yet transmit signals in just a single direction. This can be done by exploiting the refraction properties of AFM neurons to induce one-way spike transmission.

Figure 3.8 will demonstrate how the refraction properties of AFM neurons can be used to send a signal unidirectionally through a chain of symmetrically coupled neurons. In Fig. 3.8(a) the signal will originate in the red neuron on the left, and in Fig. 3.8(b) the signal will originate in the purple neuron on the right. In this schematic, all four synapses are fully bidirectional; for example, a signal generated by the blue neuron will flow to both the red neuron and the green neuron. For this neuron chain, the coupling matrix is a

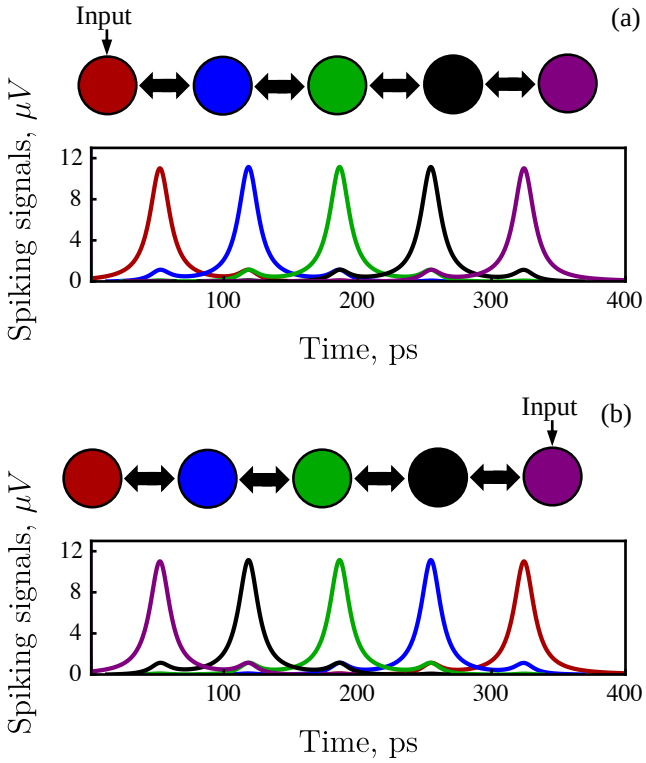

Figure 3.8: Symmetric coupling and unidirectional signal propagation. (a) Simulation result for a symmetrically coupled neural network, with an initial signal on the left, and (b) with an initial signal on the right.

symmetric matrix,

$$\kappa_{ik} = \kappa_0 \begin{bmatrix} 0 & 1 & 0 & 0 & 0 \\ 1 & 0 & 1 & 0 & 0 \\ 0 & 1 & 0 & 1 & 0 \\ 0 & 0 & 1 & 0 & 1 \\ 0 & 0 & 0 & 1 & 0 \end{bmatrix}. \tag{3.7}$$

In spite of the fact that all connections are bi-directional, simulations show that the signal will flow in only one direction.

First, consider a simulation performed where the first spike was initiated in the red neuron on the left. The simulation results are shown in Fig. 3.8(a). In this simulation, the red neuron generates a spike a $t = 50$ ps. This spike propagates to the blue neuron, which generates a spike at $t = 120$ ps. The spike from the blue neuron propagates symmetrically in two directions; and arrives at both the red neuron and the green neuron at $t = 120$ ps. At $t = 120$ ps the red neuron is in its absolute refractory period and will not generate a spike. In contrast, the green neuron will generate a spike as a result of the incoming spin current at $t = 190$ ps. After this, the green, black, and purple neurons spike in sequence. In each case, the signal will propagate symmetrically after a neuron spikes, but the refractory properties of AFM neurons prevent them from spiking, thus ensuring unidirectional signal propagation.

Consider now the network shown schematically in Fig. 3.8(b). This network is identical to that in Fig. 3.8(a), except that in this case the first spike is initiated in the purple neuron on the right. Results of simulating this neural network are also shown in Fig. 3.8(b), with the signal propagating from the purple neuron to the red neuron.

It is important to note that the neural networks in Fig. 3.8(a) and (b) are identical and unchanged; the only difference is where the initial spike was delivered. It should also be emphasized that spikes only propagate in one direction due to the refraction properties

of the AFM neuron. However, spike propagation can travel in both directions depending on where the initial spike originates from. It would be beneficial to create a circuit where signal propagation is only possible in one direction.

It is possible to form an isolator with a symmetrically connected neural network that serves this purpose. An isolator serves a function similar to that of a diode or a check valve, and restricts the signal flow to a single direction. A circuit that contains an isolator is shown in Fig. 3.9(a). The circuit consists of two sets of symmetrically coupled chains neurons, shown in red for neurons 1 through 5, and shown in blue for neurons 6 through 9. The portion of this circuit that functions as an isolator are neurons 4, 5, and 6, and includes the two weak synaptic couplings that converge on neuron 6. In this configuration, signals can flow in just one direction, from neuron 1 to neuron 9, but cannot flow in the reverse direction. This will be demonstrated via simulation.

Results of the first simulations performed on this circuit are shown in Fig. 3.9(b). In this simulation, neuron 1 spikes at $t \sim 100$ ps, and this signal propagates from neuron 1 towards neuron 5. At about $t = 500$ ps, neurons 4 and 5 generate spikes in rapid succession. Together, the two spikes generated by these two neurons have sufficient strength to cause neuron 6 to spike despite the weak synaptic coupling between the two chains. After neuron 6 generates a spike, the signal continues down the chain towards neuron 9.

Simulations were performed on the same neural network with a signal originating at neuron 9, with the results of this simulation shown in Fig. 3.9(c). In this simulation, the signal starts at neuron 9 travels to neuron 6, which spikes at $t = 500$ ps. Due to the weak synaptic coupling, the spike generated by neuron 6 has insufficient strength to cause either neuron 4 or 5 to generate a spike. Thus, the signal is unable to journey from neuron 9 to neuron 1; spikes are prevented from propagating in the “backward” direction.

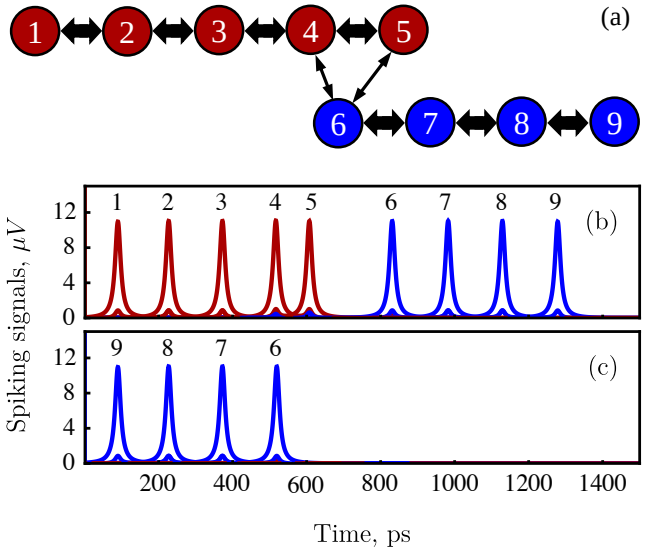

Figure 3.9: Isolator composed of symmetrically coupled neurons. (a) Schematic of the isolator circuit, with two sets of neurons, red and blue. Within these two sets, couplings are identical and fully symmetric. There is also a weak symmetric coupling between neuron 6 and neurons 4 and 5. (b) Simulation for a signal flowing from neuron 1 to neuron 9. The synaptic weights between neurons 4-5-6 are such that the combined spikes of neuron 4 and neuron 5 provide sufficient energy for neuron 6 to generate a spike. (c) Simulation for a signal flowing from neuron 9 to neuron 6. The signal is unable to continue flowing through the red chain due to the weak connections between neurons 6 and 4/5.

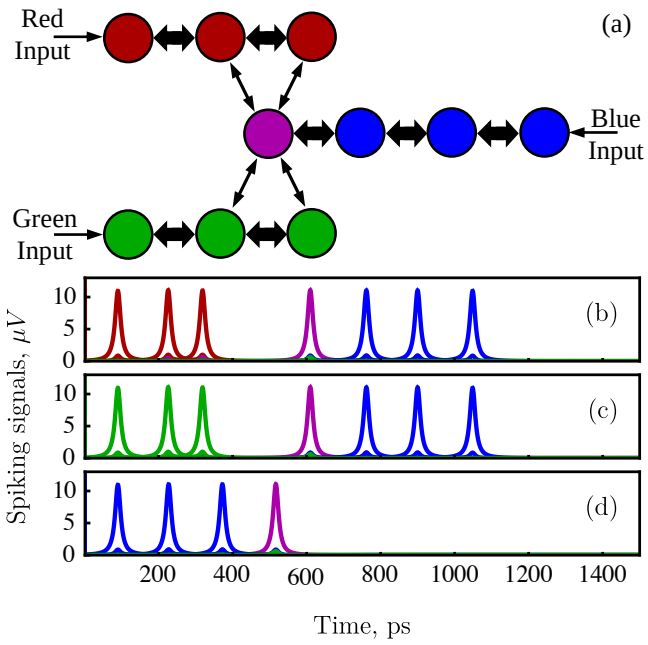

Figure 3.10: Combiner composed of symmetrically coupled neurons. (a) Schematic of the combiner circuit, with 3 sets of neurons. Input neurons are red and green, while output neurons are blue. Arrow widths represent coupling strength. (b) Simulation result for a signal that begins in the red neurons. (c) Simulation results for a signal that begins in the green neurons. (d) Simulation result for a signal that begins in the blue neurons.

The design of the isolator can be extended into a combiner circuit, whose schematic is shown in Fig. 3.10(a). This circuit has 3 sets of neurons, shown in red, green, and blue. The red and green neurons represent input branches, and the blue neurons represent an output branch. With this circuit, signals can flow from the red to blue neurons, or from the green to blue neurons. However, this configuration ensures that there is no signal leakage between the red and green branches.

Correct operation of this circuit is confirmed by simulation, with results shown in Fig. 3.10(b), (c), and (d). In Fig. 3.10(b), a signal propagates from the red input through the red neurons to the magenta neuron, then to the blue output neurons. There is no leakage to the green neurons with this architecture. Likewise, in Fig. 3.10(c), a signal that propagates from the green input to green neurons and travels to the blue neurons, without leakage to the red neurons. Lastly, in Fig. 3.10(d), a signal that begins with the blue input will propagate through the blue neurons, but will not propagate to the green or red neurons. Thus, this circuit can allow signals from the red and green branch to combine, without crosstalk between branches, and without signals flowing backwards.

3.4 Comparison of AFM neurons and biological neurons

In previous sections, characteristics shared by AFM neurons and biological neurons were presented. This section will provide a summary of these shared characteristics.

First, AFM neurons generate spiking voltages that closely resemble the action potentials of biological neurons. Furthermore, AFM neurons follow the “all-or-nothing” law. That is, AFM neurons only generate spikes when their input surpasses a critical current, in much the same way that an action potential is elicited from biological neurons. These two properties were demonstrated in section 3.2.1.

Second, AFM neurons have a response latency, as was also demonstrated in section 3.2.1. In both biological neurons and AFM neurons, after sufficient stimulus has

been delivered to the neuron, there is a time delay before the spike occurs. The latency of a stimulated biological neuron varies, depending on both the frequency and the intensity of its stimulus. With AFM neurons, the duration of the response latency can be controlled dynamically by adjusting the amplitude of the stimulus $i_p(t)$, and by adjusting the magnitude of the bias current I_{dc}. The latency period also depends on the effective damping, the anisotropy, and the exchange frequency of the AFM material.

Third, both AFM neurons and biological neurons have a refractory period. Specifically, both types of neurons have an absolute refractory period and a relative refractory period. This was discussed in section 3.2.2.

Fourth, both AFM neurons and biological neurons have variable spiking modes. That is, AFM neurons can generate single spikes, bursting spikes, or spike trains. They can also exhibit adaptation and stuttering. This was discussed in section 3.2.2.

Lastly, AFM neurons can be interconnected into a neural network where synapses mediate connections between neurons. Two methods of interconnecting neurons, via electrical current and via spin current, along with examples of spintronic synapses, were discussed in section 3.3.

Due to these similarities, AFM neurons serve as a potential candidate for modeling biological neural networks. This concept is explored in Chapter 6.

3.5 Conclusion

In summary, AFM neurons are nanometer scale spintronic elements that exhibit behavior allowing them to be used as an artificial neuron. Specifically, they have several properties that resemble the characteristics of biological neurons, including a finite refraction time, response latency, and bursting behavior. In addition, AFM neurons operate much faster than the state of the art, with a ps spike time, and with an ultra-low energy consumption of about 10^{-3} pJ per synaptic operation. It was demonstrated by simulation that AFM neurons can be interconnected into simple chains with both

symmetric and anti-symmetric coupling. In addition, one-way signal transmission can be implemented with symmetric coupling through an isolator and a combiner.

CHAPTER FOUR

SIMPLE AFM NEURON CIRCUITS

This chapter will explore how AFM neurons can be connected together in simple circuits with unique abilities. Leveraging the distinctive properties of AFM neurons outlined in the previous chapter, these circuits are designed to be compact yet highly effective. They offer potential enhancements to existing technology, such as the creation of Boolean logic gates using a limited number of neurons. Furthermore, these neuromorphic circuits exhibit unique characteristics that conventional inertia-less artificial neurons cannot replicate. For instance, the AFM inhibitor circuit demonstrates non-monotonic behaviors reminiscent of biological neural networks. Notably, the circuits discussed herein do not rely on machine learning algorithms to adjust variable synapses, simplifying their design and suggesting a straightforward implementation in hardware.

This chapter will start by detailing how AFM neurons can act as a variety of Boolean logic gates. It then goes on to discuss how multiple AFM neurons can be connected into an inhibitor circuit capable of simulating biologically realistic inhibition. Simple rings are then introduced. The chapter concludes with how the inhibitor circuit and simple rings can be combined to form controllable memory cells. The results discussed in this chapter were previously presented in paper [26] and conference presentations [29], [39], [42], [44], [45].

4.1 AFM neurons as gates for Boolean logic

Boolean logic, along with logic gates fabricated from silicon semiconductor transistors, form the backbone for conventional computing architectures [197]. While it is unlikely that AFM neurons will replace CMOS logic gates, this section provides an application example that does not require an adaptive neural network.

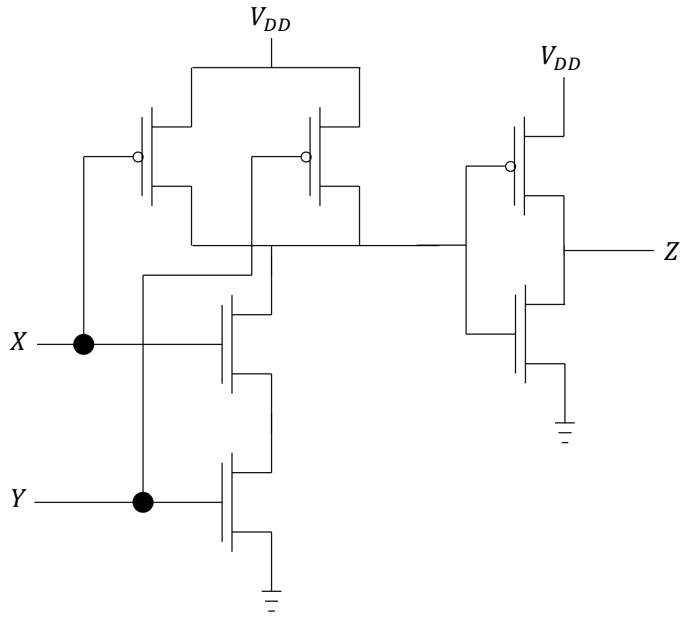

Figure 4.1: CMOS AND gate circuit. Inputs are labeled 'X' and 'Y', and the output is labeled 'Z'. A bias voltage is supplied in two places labeled as 'V_{DD}'. This CMOS AND gate circuit consists of 3 pMos transistors and 3 nMos transistors.

The most quintessential Boolean logic gate might be the AND gate [197]. The truth table for an AND gate is shown in Fig. 4.2(a). This table shows X and Y as inputs, and $Z = X \wedge Y$ as an output. In this table, 1 represents true, and 0 represents false. The CMOS circuit design for an AND gate is depicted in Fig. 4.1. It's evident from this diagram that constructing a single AND gate necessitates the use of multiple transistors. This is due to the inability to build a singular AND gate from CMOS circuit elements. Instead, two independent logic gates are combined to function as an AND gate; a NAND gate is constructed with an additional NOT gate on the output [198]. This configuration necessitates 6 transistors, complicating the design of this elementary logic gate.

In contrast to conventional CMOS circuits, a single AFM neuron with specifically tailored inputs can serve as an AND gate. As illustrated in Fig. 4.2(b), neurons X and Y

(a) AND truth table

X	Y	Z
0	0	0
0	1	0
1	0	0
1	1	1

(b) AND gate circuit

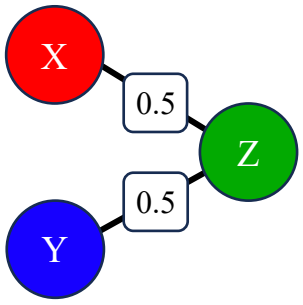

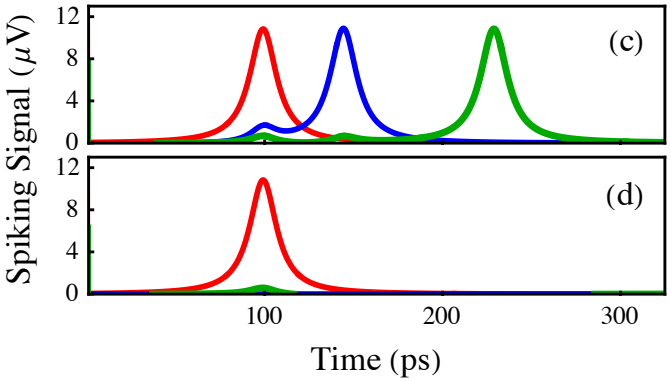

Figure 4.2: AND gate implemented with an AFM neuron. (a) Truth table for an AND gate. (b) Schematic of the AFM neuron for an AND gate. Neurons labeled X and Y serve as inputs, and neuron Z as the output. The coupling strength between inputs and outputs is set at $0.5\kappa_0$. (c) Simulation with the logical inputs $X = 1$ and $Y = 1$. X is shown with a red curve, and Y is shown with a blue curve. The output $Z = 1$ is shown with a green curve. (d) Simulation with the logical inputs $X = 1$ and $Y = 0$. X is shown with a red curve, and the $Y = 0$ curve is not visible. The $Z = 0$ curve does not show a spike, but instead a small bump.

function as inputs, while neuron Z serves as the output. To establish full strength coupling between two AFM neurons, ensuring that a spike from one neuron triggers a spike in the next, the synapses have a coupling strength of $1\kappa_0$. This coupling constant is elaborated in section 3.3.2, which presents simple chain structures. For configuring the AFM neuron as an AND gate, each input must be coupled to ensure that the strength between neurons is insufficient to elicit a spike in the output neuron independently. However, when both inputs X and Y spike, the internal threshold is reached, causing the AFM output neuron Z to generate a voltage spike. This precise configuration is achieved by setting the coupling strength between both inputs and the output to a value of $0.5\kappa_0$, as depicted in Fig. 4.2(b).

Numerical simulations of an AFM neuron configured as an AND gate were performed, with results shown in Fig. 4.2(c) and (d). The AND gate in Fig. 4.2(c) has inputs $X = 1$ and $Y = 1$. The X input is shown as a function of time with a red curve, and it has a spike at $t = 100$ ps. This spiking signal represents $X = 1$. Likewise, the Y input is shown as a function of time with a blue curve, and has a spiking signal at $t = 150$ ps. This spike represents a $Y = 1$. Together, these two inputs provide enough energy that the neuron is able to generate an output spike at $t = 220$ ps, which is represented by a green curve. This output spike represents $Z = 1$, thus demonstrating that this portion of the AND gate truth table can be realized by an AFM neuron.

Figure 4.2(d) shows the results of numerical simulation for an AND gate when the inputs are $X = 1$ and $Y = 0$. The X input is shown as a function of time with a red curve, spiking at $t = 100$ ps. This red spiking signal represents an $X = 1$ input. In this plot, Y is represented by a blue curve, which does not spike at all, and hence it properly represents $Y = 0$. In Fig. 4.2(d) there is no green output spike, only a small bump at $t = 100$ ps. This is the AFM neuron receiving the insufficient signal from the X=1 input. The lack of a green curve corresponds to the output is $Z = 0$ and is as expected for these inputs. Additional simulations were performed to confirm that the same AFM neuron will fulfill

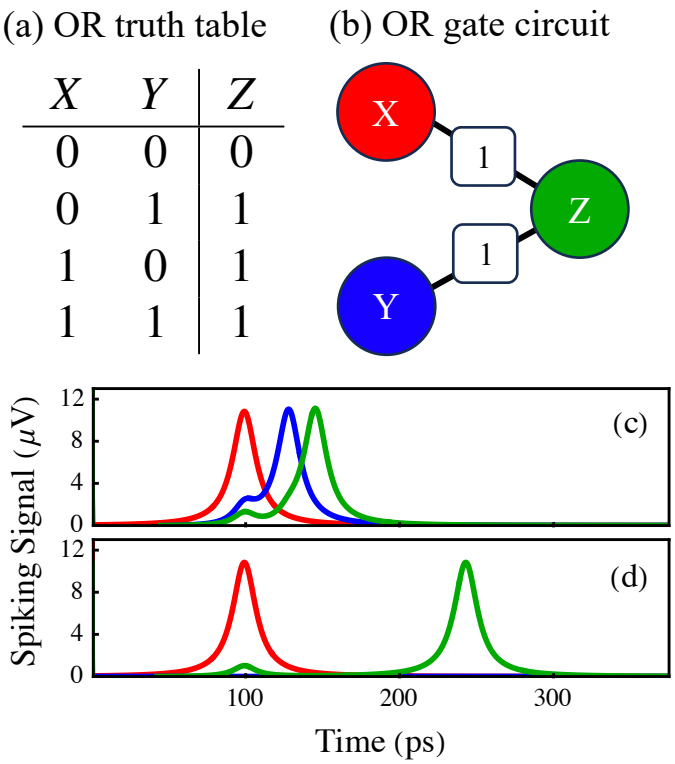

Figure 4.3: OR gate implemented with an AFM neuron. (a) Truth table for an OR gate. (b) Schematic of the AFM neuron for an OR gate. Neurons labeled X and Y serve as inputs, and neuron Z as the output. The coupling strength between inputs and outputs is set at $1\kappa_0$. (c) Simulation with the logical inputs $X = 1$ and $Y = 1$. X is shown with a red curve, and Y is shown with a blue curve. The output $Z = 1$ is shown with a green curve. (d) Simulation with a logical inputs $X = 1$ and $Y = 0$. X is shown with a red curve, and the $Y = 0$ curve is not visible. The output $Z = 1$ is shown with a green curve.

lines 1 and 2 of the AND truth table, thus showing that a single AFM neuron can act as an AND gate.

Similar to the AND gate configuration, an AFM neuron with specific coupling can be used as an OR gate. [197]. The truth table for an OR gate is shown in Fig. 4.3(a). This table shows X and Y as inputs, and Z= $X \vee Y$ as an output. Like the CMOS AND gate shown in Fig. 4.1, the CMOS OR gate circuit requires 6 transistors. Again this is due to the inability to directly construct an OR gate, which must be created from a NOR gate and

a NOT gate. As before, a single AFM neuron with carefully tailored inputs is sufficient to function as an OR gate. Figure 4.3(b) illustrates the AFM circuit for an OR gate, where inputs X and Y are coupled to output Z. In contrast to the AND gate, the coupling strength from each input is enough to produce a spike from the output with a weight of $1\kappa_0$. Therefore, a single spike from either input causes the AFM neuron to produce an output spike.

Numerical simulations of an AFM neuron configured as an OR gate were performed, with results shown in Fig. 4.3(c) and (d). The OR gate in Fig. 4.3(c) has inputs $X = 1$ and $Y = 1$. The X input is shown as a function of time with a red curve, and it has a spike at $t = 100$ ps, thus representing $X = 1$. Likewise, the Y input is shown as a function of time with a blue curve, and has a spiking signal at $t = 120$ ps, representing $Y = 1$. As each input individually is enough to produce an output, together they provide enough energy to generate an output spike at $t = 150$ ps, which is represented by a green curve. This output spike represents $Z = 1$, demonstrating that this portion of the OR gate truth table can be realized by an AFM neuron.

Figure 4.3(d) shows the results of numerical simulation for an OR gate when the inputs are $X = 1$ and $Y = 0$. The X input is again shown with a red curve spiking at $t = 100$ ps, representing an $X = 1$ input. In this plot, Y is represented by a blue curve, which does not spike at all, and hence it properly represents $Y = 0$. In Fig. 4.3(d), the output Z produces a spike illustrated by the green curve at $t = 250$ ps, thus $Z = 1$. This demonstrates that a single input is enough to produce an output, the quintessential definition of an OR gate. Additional simulations were performed to confirm that the same AFM neuron will fulfill lines 1 and 2 of the OR truth table, thus showing that a single AFM neuron can act as an OR gate.

Although both Fig. 4.3(c) and (d) correspond to lines of the truth table with the output $Z = 1$, there is a noticeable difference in the spiking time of the output neuron Z.

When both inputs generate a spike, the output neuron spikes much sooner than when only a single input fires. This discrepancy arises from the delay or response latency between inputs and outputs of an AFM neuron due to the effective inertia. With both inputs firing, the output neuron receives double the strength required to produce a single spike, thus shortening the delay between inputs and outputs of the AFM output neuron Z. This is apparent from the 100 ps difference in the spiking time of the output neuron when there are two inputs (Fig. 4.3(c)) compared to when there is only one input (Fig. 4.3(d)). This variation in output times can be problematic when incorporating multiple AFM logic gates in the same circuit. This discrepancy can be addressed by dynamically adjusting the coupling between inputs and outputs. For instance, the coupling to the output neuron can be increased above $1\kappa_0$ when only a single input fires, thereby reducing the delay between the input spike and the output spike. Conversely, the coupling can be reduced when two inputs fire to match the delay from a single input. However, the need for dynamic coupling would significantly increase the complexity of the logic gate, negating the advantages of using AFM neurons. Therefore, CMOS technology remains the best option for building large logic circuits.

In addition to serving as an AND and OR gate, a single AFM neuron can also function as a majority gate. A majority gate is a Boolean circuit that outputs true when more than half of its inputs are true. The truth table for a 3-input majority gate is depicted in Fig. 4.4(a), while the configuration for implementing this majority gate using AFM neurons is illustrated in Fig. 4.4(b). Constructing a 3-input CMOS majority gate typically requires 4 NAND gates, necessitating a total of 16 transistors [197]. In contrast, to configure a AFM circuit as a majority gate, a single input is insufficient to produce an output with the coupling strength of $0.5\kappa_0$. Instead, two inputs together would trigger the AFM output neuron to generate a single spike. Similarly, the presence of all three inputs

(a) Majority truth table

W	X	Y	Z
0	0	0	0
0	0	1	0
0	1	0	0
0	1	1	1
1	0	0	0
1	0	1	1
1	1	0	1
1	1	1	1

(b) Majority gate circuit

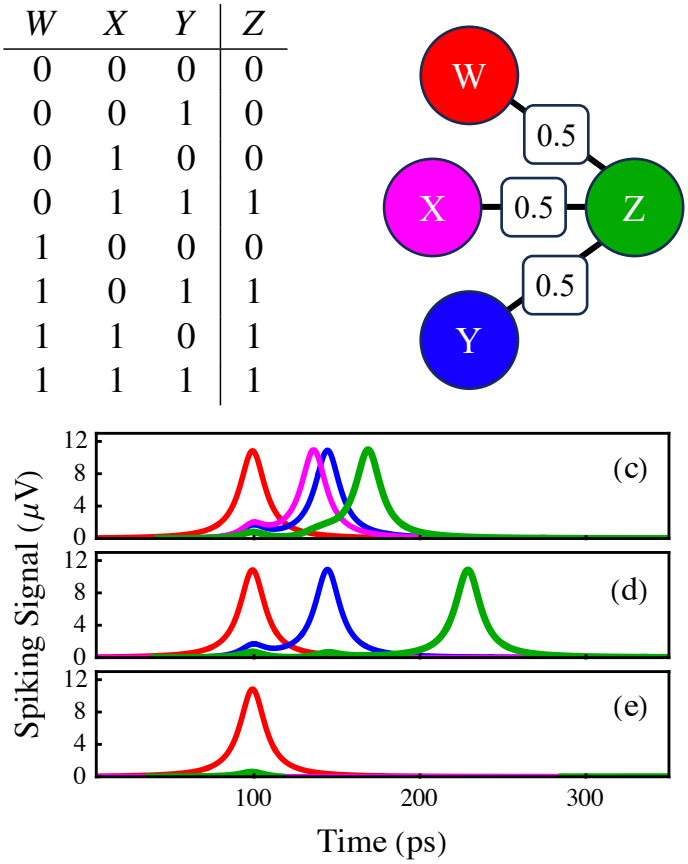

Figure 4.4: Majority gate implemented with an AFM neuron. (a) Truth table for a Majority gate. (b) Schematic of the AFM neuron for a Majority gate. Neurons labeled X, Y, and W serve as inputs, and neuron Z as the output. The coupling strength between inputs and outputs is set at $0.5\kappa_0$. (c) Simulation of a majority gate with $W = 1$ in red, $X = 1$ in magenta, and $Y = 1$ in blue. Because there are ≥ 2 true inputs, $Z = 1$, as shown by the green curve. (d) Simulation of the majority gate for $W = 1$, $X = 0$, and $Y = 1$. Because ≥ 2 inputs are true, the output Z is also true, as evidenced by the green curve. (e) Simulation of the majority gate for $W = 1$, $X = 0$, and $Y = 0$. Because < 2 inputs are true, $Z = 0$, and hence, there is no green curve.

would also lead to a single spike, while ensuring that the threshold current does not induce bursting behavior.

Numerical simulations of the majority gate are shown in Fig. 4.4(c), (d), and (e). Simulations for the last line of the truth table, when $W = 1$, $X = 1$, and $Y = 1$, are shown in Fig. 4.4(c). These inputs are represented by the red, pink, and blue curves. As a minimum of two spiking inputs is required to produce an output signal, with all three inputs spiking, an output signal is produced, illustrated by the green curve. Thus this simulation accurately reproduces this line of the truth table.

Figure 4.4(d) illustrates simulations for the inputs $W = 1$, $X = 0$, and $Y = 1$. With two out of the three inputs spiking, represented by the red and blue curves, the AFM neuron generates an output spike depicted by the green curve, representing $Z = 1$. This exemplifies the quintessential definition of a majority gate, where a positive output is produced with two or more inputs. Similar to the behavior observed in the OR gate, the timing of the output neuron Z is sooner when all three inputs are active (Fig. 4.4(c)) compared to when only two inputs are active (Fig. 4.4(d)). This phenomenon arises due to the reduced inertia-induced delay resulting from a stronger total input received by the output neuron.

Figure 4.4(e) shows simulations for $W = 1$, $X = 0$, and $Y = 0$. Here, only one input produces a spike shown by the red curve. This solitary input signal is insufficient to produce an output, shown by the lack of a green curve hence $Z = 0$. From Fig. 4.4(c-e), it is evident that a single spiking input is insufficient to generate an output spike, while two or more input spikes will generate an output spike, thus confirming that this AFM neuron circuit can act as a majority gate.

The creation of Boolean logic gates utilizing AFM neurons relies significantly on the synaptic connections established between inputs and outputs. These synapses can be realized through copper waveguides, as discussed in section 3.3. By employing this

approach, the coupling strength can be readily regulated by adjusting the dimensions of the copper synapse. Utilizing copper synapses would yield static AFM neuron circuits, which, when configured with appropriate coupling strengths, can function as Boolean logic gates. However, with the incorporation of adjustable synapses, AFM circuits can offer dynamically reconfigurable logic capabilities.

Previous work provides an in-depth analysis of performing Boolean logic with AFM neurons and includes a description of a "Q-gate" and a full-adder that consists of just three AFM neurons [199].

4.2 Inhibition

Biological neurons exhibit an interesting feature in the form of inhibition. Biological neurons can be suppressed by a second input through inhibitory synapses, which reduces the likelihood of a neuron firing by reducing the membrane voltage further away from the threshold [200], [201]. Replicating this inhibitory feature in artificial neurons requires a circuit design as depicted in Fig. 4.5(a). This inhibitor circuit comprises two inputs—an excitatory input and an inhibitory input—along with one output. The corresponding truth table, shown in Fig. 4.5(b), outlines its behavior. When

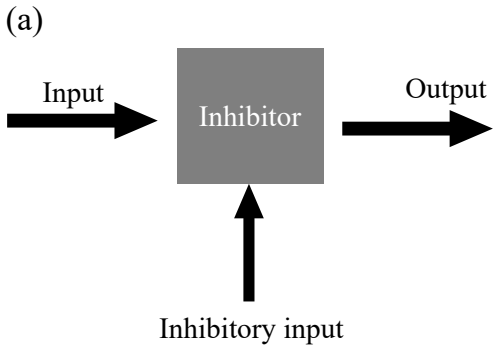

(b)

Input	Inhibitory input	Output
0	0	0
1	0	1
1	1	0

Figure 4.5: Inhibitor circuit design. (a) Schematic for the inhibitor circuit consisting of an excitatory input, an inhibitory input, and one output. (b) Truth table for an inhibitor circuit.

there's no signal from either input, the output remains inactive. With a single input from the excitatory source, the output fires. However, when both an excitatory and an inhibitory input are present, the output should be suppressed. This scenario exemplifies the non-monotonic functions observed in biological neurons. By definition, the inhibitor function involves two input signals yielding zero outputs. Traditional inertia-less artificial neurons, being strictly monotonic, produce an output with any positive number of inputs.

Leveraging the unique properties of AFM neurons, it is feasible to construct two distinct types of inhibitor circuits that adhere to the inhibitor truth table. The first approach involves using the reversible polarity of AFM neurons. By applying a negative voltage spike as the inhibitory input, two competing signals can be used to simulate *negative inhibition*. This method effectively cancels out the excitatory input, preventing the output neuron from firing. A more interesting scenario would be *positive inhibition*, where an all-positively biased circuit exhibits inhibitory signals. Positive inhibition with AFM neurons leverages the inertia-induced delay between inputs and outputs to create an inhibitor circuit with non-monotonic functions. By exploiting this delay, the circuit can produce inhibitory signals even within a positively biased framework, a feat unattainable with traditional inertia-less artificial neurons.

Since AFM neurons exhibit dual-polarity characteristics, as discussed in section 3.2.3, they can effectively simulate negative inhibition. The AFM circuit illustrating negative inhibition is depicted in Fig. 4.6(a), comprising an input neuron and an output neuron, both biased by a positive spin current. Additionally, an inhibitor neuron is biased by a negative spin current. In the simulation of the uninhibited network shown in Fig. 4.6(b), the green input neuron generates a spike at $t = 50$ ps, triggering the pink output neuron to fire a spike at $t = 115$ ps, representing an uninhibited scenario. In contrast, Fig. 4.6(c) illustrates the introduction of a negative spike from the inhibitor neuron alongside the positive input spike. Consequently, the output neuron receives two opposing signals

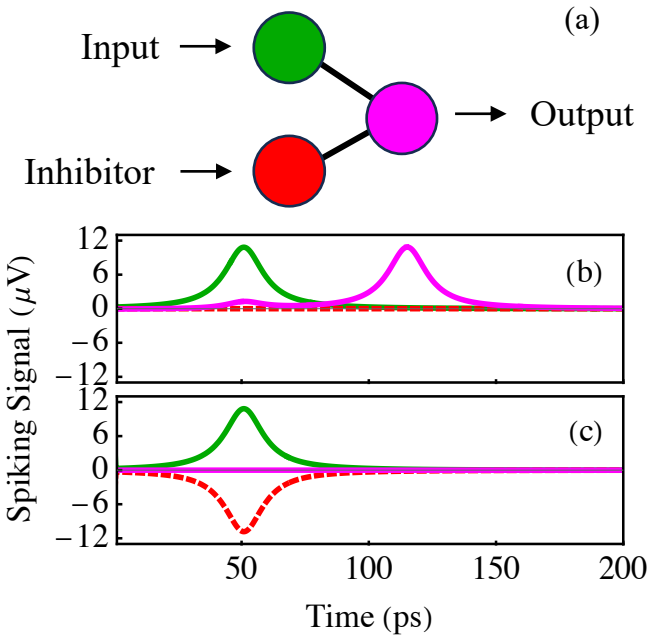

Figure 4.6: Negative inhibition. (a) AFM neuron circuit demonstrating negative inhibition, with an input neuron (green), an inhibitor neuron (red), and an output neuron (magenta). (b) Simulation of uninhibited circuit. The input neuron fires (green curve) a positive spike and leads to an output spike (magenta curve). (c) Simulation of negative inhibition. The input neuron (green curve) fires a positive spike, while the inhibitor neuron (red dashed curve) fires a negative spike. The inhibitory spike suppressed the output neuron shown by the lack of a magenta spike.

simultaneously. As a result of the opposite polarity of these signals, they cancel each other out, leading to the absence of a pink output spike in Fig. 4.6(c). This phenomenon of negative inhibition exemplifies how two sub-networks of different polarities can mutually inhibit each other.

Similar behavior can be achieved with an all-positively biased circuit by using negative coupling between the inhibitor and output neuron. However, such an approach introduces additional complexities. This necessitates the inversion of the spin current spike generated by the inhibitor neuron, requiring additional circuitry in the synaptic connection between the two neurons. Typically, synaptic connections between AFM neurons are characterized by strictly positive weights, such as those facilitated by simple copper waveguides. Therefore, it would be intriguing to devise an all-positive inhibitor circuit that doesn't rely on negative connections. Such a circuit would be unattainable with inertia-less artificial neurons due to their strictly monotonic functions. Yet, the effective inertia present in AFM neurons enables the construction of seemingly impossible circuits.

The inhibitor circuit demonstrating positive inhibition is shown in Fig. 4.7(a). This neural network consists of 5 neurons, including input (green) and output (magenta) neurons. A signal is carried from the input neuron to the output neuron through two intermediate neurons (blue). Please note that the synapses are adjusted to a value of $1\kappa_0$, illustrated by solid black lines so that the signal from the input neuron is strong enough to initiate a spike in both intermediate neurons. However, the synapses from the intermediate neurons to the output neurons are weakened with a value of $0.5\kappa_0$, illustrated by dashed black lines. A single intermediate neuron spiking is not enough to cause the output neuron to fire. Instead, both intermediate neurons must spike at nearly the same time in order to produce a strong enough signal for the output neuron to spike.

The uninhibited circuit is depicted in Fig. 4.7(b). Here, the input neuron emits a green spike at $t = 100$ ps, triggering both blue intermediate neurons to fire almost

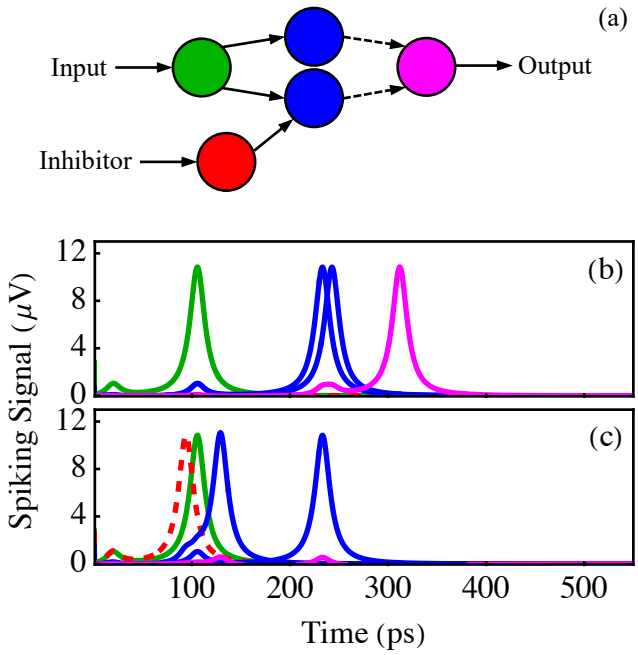

Figure 4.7: Positive inhibition. (a) The AFM circuit for demonstrating positive inhibition, with the input neuron (green), intermediate neurons (blue), output neuron (magenta), and the inhibition neuron (red). The synapses are weighted such that solid arrows represent a full connection, $1\kappa_0$, while dashed arrows represent a half connection, $0.5\kappa_0$. (b) Simulation of uninhibited circuit. The input neuron, with a green curve, fires. This leads the two intermediate neurons, with blue curves, to fire. Together, the spikes from the intermediate neurons provide enough current for the magenta output neuron to fire. (c) Simulation demonstrating positive inhibition. The red and green neurons fire, leading the lower intermediate neuron to fire with a shorter delay then the upper intermediate neuron. Because the intermediate neurons fire at different times, the output neuron does not fire.

simultaneously. The combined signals from these intermediate neurons exceed the weak coupling of the output neuron, causing it to emit a pink spike at $t = 310$ ps. In contrast, the inhibited circuit is illustrated in Fig. 4.7(c). At $t = 90$ ps, the inhibitor neuron emits a spike, indicated by the red dashed curve. The simultaneous spikes from the red and green neurons shorten the delay induced by the effective inertia of the lower intermediate neuron, prompting it to fire much sooner compared to the scenario with a single input. As the lower intermediate neuron fires at a different time than the upper intermediate neuron, insufficient energy reaches the magenta output neuron, preventing it from firing. Consequently, the inhibitor truth table's last line is satisfied: two inputs, one excitatory and one inhibitory, lead to zero outputs. This non-monotonic function of the inhibitor circuit is only possible through the effective inertia of AFM neurons and, therefore, impossible with conventional inertia-less neuromorphic circuits.

4.3 Memory cells

Consider the neural network shown in Fig. 4.8(a). It consists of a ring of AFM neurons with a simple input. Simulation results for this neural network are shown in Fig. 4.8(b). The simulation begins by first initiating a spike in the green neuron. This leads to a spike in neuron 1, which leads to a spike in neuron 2, which leads to a spike in neuron 3, which then continues around the loop back to neuron 1. As can be seen in the simulation results, the spike will continue around this ring indefinitely. This ring can receive a spike as input and hold it until it is needed in other parts of a larger neural network.

Multiple spikes can be stored in the same ring by increasing the number of neurons comprising the ring. The neural network of a ring capable of accommodating two independent spiking signals is illustrated in Fig. 4.9(a). Similar to the simple ring structure, it includes one green input neuron and six blue neurons forming the ring. Figure 4.9(b) depicts this ring holding a single spiking signal. The input neuron spikes at $t = 121$ ps represented by the green curve, introducing a single spike into the ring network. The

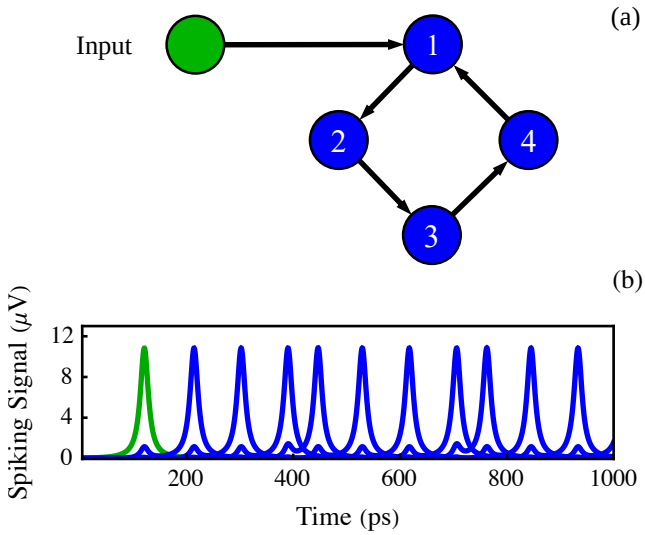

Figure 4.8: Simple AFM neuron ring. (a) Schematic of the neural network for the ring, with a green input neuron and 4 labeled blue ring neurons. (b) Simulation of the neural network, where the green curve represents a spike from the green input neuron, and the blue curves represent spikes from the four ring neurons.

propagation of a single spike around the ring is depicted by the blue curve plotting the spiking signal of one ring neuron. It clearly shows that it travels around the ring with a period of 526 ps. The simulation results of the ring holding two independent spiking signals are shown in Fig. 4.9(c). To prevent interference between the two spikes, there should be a delay between the two inputs exceeding the refraction time of AFM neurons. Additionally, the total number of ring neurons should be sufficient to maintain a significant distance between the two spikes. In this case, the input neuron inserts two spikes into the ring approximately 272 ps apart, well above the refraction time of $\approx$ 100 ps detailed in section 3.2.2. As observed from the blue curve in Fig. 4.9(c), the two spiking signals propagate around the ring independently, each with a period of $\approx$ 530 ps, and without affecting each other.

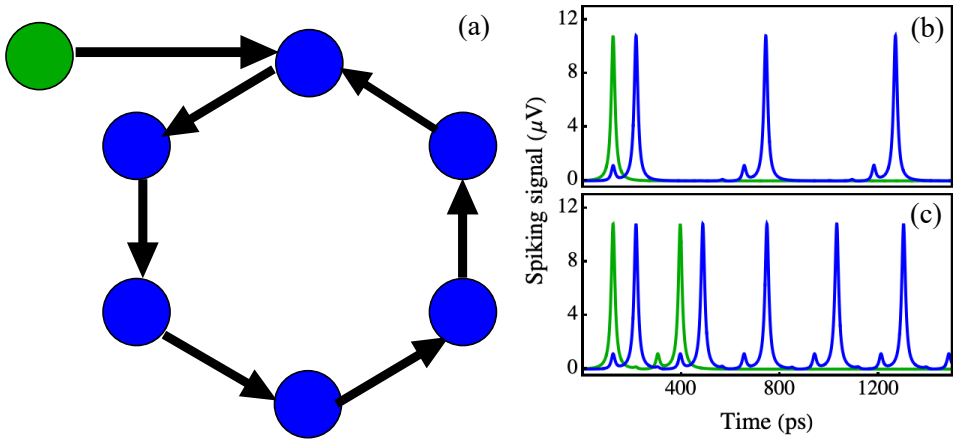

Figure 4.9: Double spiking AFM neuron ring. (a) Neural network configuration of the AFM ring capable of retaining two spiking signals, featuring one green input neuron and six blue ring neurons. (b) Simulation results illustrating the ring containing a single spiking signal. The input neuron spikes once (depicted by the green curve), and the resulting spike propagates around the ring (depicted by the blue spiking signal plotted from one neuron in the ring). The spike propagates around the loop with a period of 526 ps. (c) Simulation results of the ring retaining two spiking signals. The input neuron introduces two spikes into the loop, spaced 272 ps apart. Each spiking signal circulates around the loop with a period of ≈ 530 ps.

Figures 4.8 and 4.9 showcase examples of uncontrollable AFM rings. Remarkably, the inhibitor functionality can have applications in constructing controllable memory cells, which is shown in Fig. 4.10(a). The memory cell consists of an input neuron, an inhibitor neuron, and 5 intermediate neurons, as shown in the figure. Operation of the memory cell will be demonstrated by simulation. Initially, the entire system is at rest. Then, at $t = 100$ ps, the green input neuron generates a spike. This is shown by a green curve in Fig. 4.10(b). This signal from the input neuron then enters the blue neuron ring at the neuron labeled "1", as shown in Fig. 4.10(b). After this, the spiking signal will travel through the neuron ring, from neuron "1" to "2", then to neurons "3a" and "3b", then to neuron "4". These neurons, spiking in succession, are shown by multiple blue curves in Fig. 4.10(c). Please note that the synapses have been adjusted so that both neurons 3a and

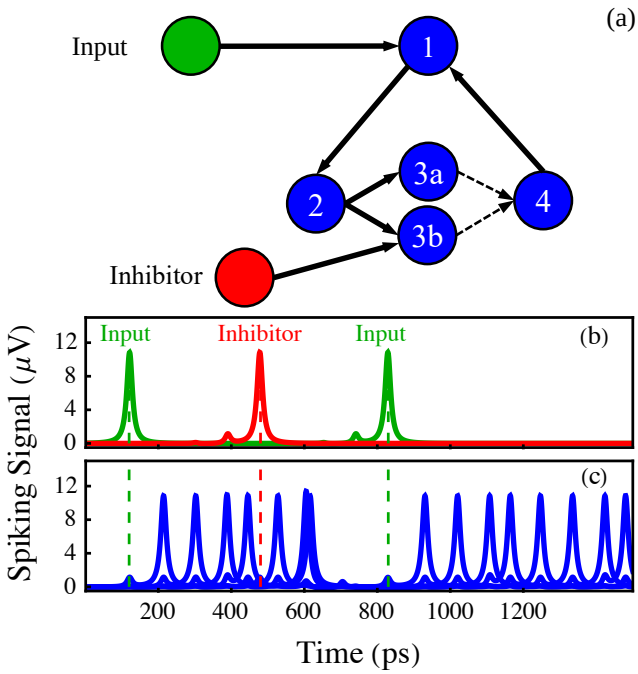

Figure 4.10: AFM neuron memory cell. (a) The memory cell neural network. The input neuron is colored green, the inhibitor neuron is colored red, and the memory neurons are colored blue. (b) Simulated input and inhibition signals. (c) Simulated response to the input. The input signal at $t = 100$ ps initiates the signal to flow from 1 to 4 and cyclically repeats until $t = 500$ ps when the inhibitor signal stops the cycle. The cycle is restarted by an input spike at $t = 800$ ps.

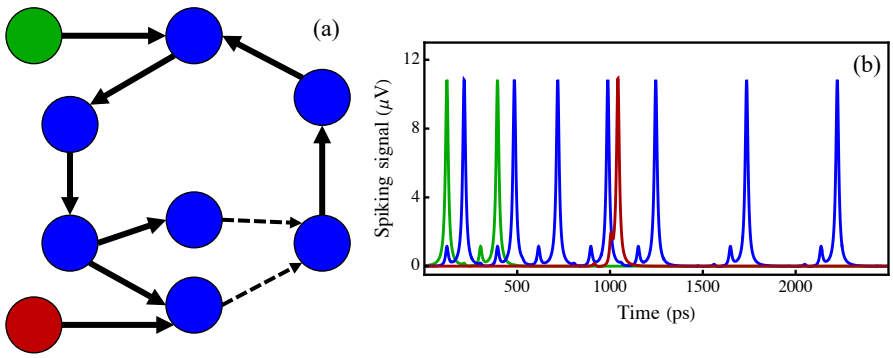

Figure 4.11: Double spiking memory cell. (a) Neural network configuration of the double spiking memory cell. It includes one input neuron (green), seven ring neurons (blue), and one inhibitor neuron (red). The inhibitor circuit is prominently visible in the center of the ring. (b) Simulation results of a double spiking memory cell, demonstrating its capability to retain two spiking signals. The green inputs represent the insertion of two spikes into the memory cell. The blue curve plots the spiking signal of one neuron in the ring and depicts the propagation of the spikes around the ring. Both spikes transverse the ring for 1000 ps. The red inhibitor signal fires at 1042 ps and suppresses one of the spiking signals while leaving the other unaffected.

3b must spike at nearly the same time in order for neuron 4 to generate a spike, thus forming an inhibitor circuit in the middle of a memory cell.

The inhibitor neuron fires at $t = 500$ ps, as shown by a red curve in Fig. 4.10(b). The signal from the inhibitor neuron causes neuron 3b to fire at a time earlier than neuron 3a. Due to this variance in timing and the weak synaptic connection between neurons 3 and 4, neuron 4 has insufficient energy to generate a spike, which stops the signal from circulating. Thus, the properties of positive inhibition were used to control a spiking signal propagating in a memory cell. After this, the input signal fires once more at $t = 800$ ps, and the memory signal circulates once again, as shown in Fig. 4.10(c).

The inhibitor memory cell can be expanded by integrating a larger ring capable of holding two spikes. Figure 4.11(a) illustrates the neural network of the double spiking memory cell. Similar to Fig. 4.9(a), it comprises six ring neurons with one input neuron,

while like Fig. 4.10(a), the inhibitor circuit is incorporated into the ring. Consistent with the setup of the double spiking ring, two spikes are introduced into the memory cell 272 ps apart, as illustrated by the green curves in Fig. 4.11(b). Both spikes traverse the loop for approximately 1000 ps. Subsequently, as one of the spikes reaches the inhibitor circuit, the red neuron emits the inhibitor signal at $t = 1042$ ps to neutralize one of the propagating spikes while the other remains unaffected. Following the red inhibitor signal, Fig. 4.11(b) clearly indicates that only a single spike remains in the ring. Hence, controllable memory cells can be engineered to hold any quantity of spikes by merely modifying the number of neurons comprising the ring.

4.4 Conclusion

In summary, simple AFM neuron circuits prove versatile for functioning as multiple Boolean logic gates. Notably, AFM neurons uniquely possess the capability to manifest inhibition—a trait reminiscent of biological neurons but absent in other inertia-less artificial neuron models. Simple AFM rings are constructed such that an initially inputted spike seamlessly propagates around the ring. Furthermore, the incorporation of an inhibitor circuit into a ring introduces precise controllable memory cells, enhancing the adaptability and functionality of AFM neuron-based architectures.

CHAPTER FIVE

PATTERN RECOGNITION WITH AFM NEURONS

Despite the increase in the computational capability of typical Von Neumann architecture, the human brain still outperforms modern computers at classification tasks with a fraction of power consumption [8], [95]. By mimicking brain-like behaviors through hardware-implemented ANNs, neuromorphic chips perform pattern recognition with reduced power consumption and increased efficiency [99].

Simple neural networks employing AFM neurons presented in previous chapters featured static synapses that carry spikes from neuron to neuron with constant coupling. Thus, they lack the ability to demonstrate more complex computation beyond signal propagation or other unique features like inhibition. Variable synapses are required in neural networks capable of demonstrating pattern recognition, a standard neuromorphic computing benchmark task. These variable synapses in neural networks are trained using machine learning algorithms such as those introduced in section 2.2.1 and section 2.2.2. This chapter will introduce two different supervised learning algorithms used to train AFM neural networks. The AFM neural networks trained for pattern recognition detailed in this chapter boast a higher efficiency in both power consumption and training and recognition time due to the ultra-fast dynamics of AFM materials.

This chapter begins by introducing the first attempt at training AFM neural networks for pattern recognition. It provides an overview of the supervised learning algorithm utilized, along with the resulting single-layer neural network. Then, a more sophisticated algorithm based on backpropagation is introduced, followed by a detailed exploration of multilayered AFM neural networks employing this technique. Some of the

results discussed in this chapter were previously presented in paper [27] and conference presentations [30], [31], [36], [37], [40], [43], [46].

5.1 SPAN neural network

In this section, we theoretically investigate the possibility of using AFM neurons combined with a supervised learning algorithm to create neural networks that recognize symbols generated from a grid of input neurons [202], [203]. We show that, due to the strongly nonlinear and inertial dynamics of AFM neurons, even a single AFM neuron is capable of successfully recognizing various symbols from a 5×5 input grid, which is enough to encode various printed symbols. Our simulations show that the total training time of an AFM neuron can be below 1 μs, while the power consumption during the training is of the order of 30 pJ. This research provides the first demonstration of the ability of AFM neurons to perform learning tasks, thus making clear the potential for using artificial AFM neurons in machine learning applications.

5.1.1 Methods

As discussed in section 2.3.1, the first term in the AFM neuron model governed by Eq. (2.24) results in an effective inertia. This inertia results in a latency or delay between a neuron receiving an input and the resulting output, an effect not found in conventional inertia-less artificial neurons. When AFM neurons are linked together, such that the output of one neuron acts as the input of the next, the delay is dependent on the coupling strength κ_{ik} between the neurons. The delay caused by inertia decreases as the strength between neurons increases. Thus, the firing time of the neuron can be easily controlled. This means that the AFM neurons are well-suited for neuromorphic algorithms in which time encoding of neuron spikes is used.

One such time-encoding approach, namely, Spike Pattern Association Neuron (SPAN) [202], is studied in this section. The architecture of an AFM neural network realizing the SPAN algorithm is shown in Fig. 5.1(a). It consists of one output "SPAN"

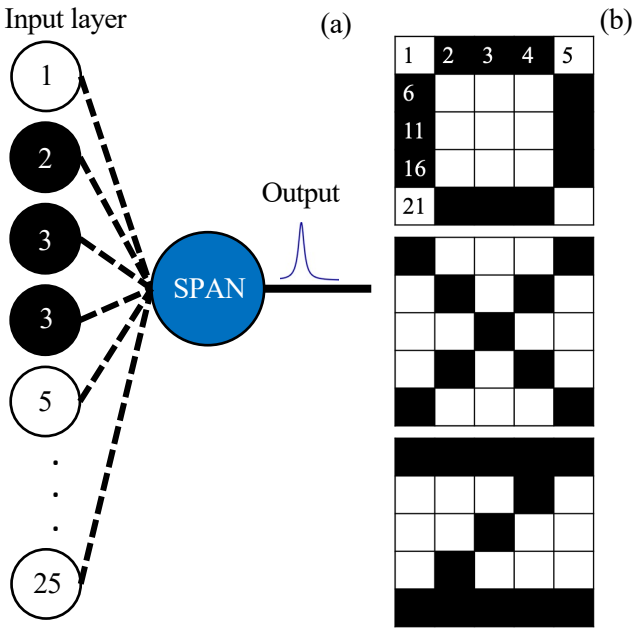

Figure 5.1: Single AFM SPAN neural network. (a) The architecture of AFM SPAN neural network. The input symbol is encoded in the spiking pattern of the input layer neurons. The synaptic weights between the input layer and the AFM SPAN neuron are adjusted during training. The temporal position of the SPAN's output spike encodes the outcome of pattern recognition. (b) Examples of the different input symbols used in pattern recognition where each pixel cell represents a different input neuron that will fire if the pixel is black.

neuron connected to many neurons of the input layer. In our simulations, the input layer consisted of 25 neurons and encoded input symbols drawn in a 5×5 binary grid. We used several shapes of the input symbols shown in Fig. 5.1(b). A blackened pixel in the input symbol causes a spike in the corresponding input neuron, while a white pixel will have no spike. The SPAN neuron is trained to output a spike at a certain target time if the input symbol matches the pattern to be recognized. To achieve this, synaptic connections between the input layer and the SPAN neuron are adjusted during the training, as explained below.

We used parallel encoding of the input layer; namely, the input symbol triggers the input neurons to fire simultaneously. There will be an output spike if the combined weights connected to the SPAN are strong enough. The goal of training is to move this output spike to the desired time for a chosen symbol. If the spike is produced earlier (later) than the target time, the weights connected to the SPAN should reduce (increase).

In more detail, the SPAN training algorithm is based on the Widrow-Hoff rule, where the difference between the desired spike time t_d and the actual spike time t_a is used to update the synaptic weights. After some manipulation, shown in Ref. [204], the Widrow-Hoff rule is transformed to describe the change in weights during training:

$$\Delta\kappa = \lambda \left(\frac{e}{2}\right)^2 \left[(t_d - t_i + \tau)e^{-\frac{(t_d - t_i)}{\tau}} - (t_a - t_i + \tau)\, e^{-\frac{(t_a - t_i)}{\tau}}\right], \tag{5.1}$$

where λ is a positive and constant learning rate, t_i is the timing of the input spike, t_d is the desired timing of the output spike, t_a is the actual timing of the output spike, and τ is a time constant corresponding to the width of a spike. A summary of constants used in the SPAN neural network is presented in appendix A. Due to the simplicity of the SPAN algorithm, it is only capable of training a neuron to a single symbol. Upon training, a

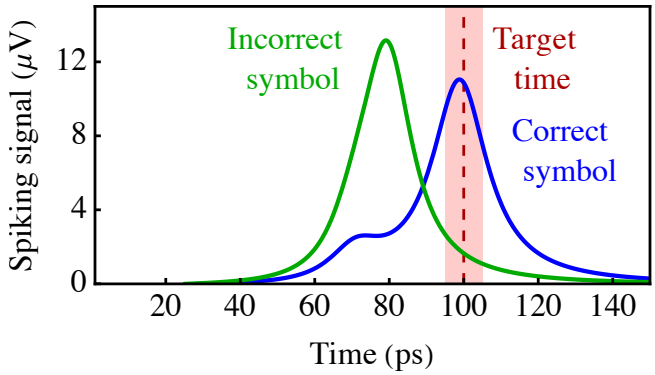

Figure 5.2: Simulation result of output signals generated by a trained AFM SPAN network. The red dashed line shows the target time for symbol recognition, with a 10 ps time window (red shading) encompassing the target time. The blue (green) line shows the simulated output spike of the AFM SPAN for the correct (incorrect) input symbol.

SPAN should output its spike at the target time t_d for the correct symbol and spike away from the target time for any other symbol.

A library of 20 symbols is used to train the neural network. These symbols are all variations of the correct symbol chosen from one of the symbols shown in Fig. 5.1(b). Variations include symbols with multiple additional or missing pixels. Initially initialized with random synaptic weights κ_{ik}, the neural network receives each symbol as an input during one epoch or cycle of training. A symbol is associated with a target time corresponding to the image's difference from the correct symbol. Using this time and the actual timing of the output neuron, the SPAN algorithm determines how the weights should be changed in accordance with Eq. (5.1). The algorithm is modified such that the weights cannot become negative, ensuring a more straightforward implementation in hardware. When all images have been processed, the weight changes resulting from each symbol are averaged, the neural network is updated, and the next epoch begins.

Figure 5.2 shows the output spikes of a SPAN neural network after training. When the correct symbol is supplied as input, the SPAN spikes within a 10 ps time window of

the target time; this implies that the neural network has recognized the chosen symbol. Any other symbol should cause a spike outside the target time window, indicating that a different symbol was used as input.

5.1.2 Results

Figure 5.3(a) shows the error between the actual and desired spike time for the correct symbol throughout training, and Fig. 5.3(b) shows the corresponding changes in each synaptic weight. In this case, the neural network is being trained to the "O" symbol, shown in Fig. 5.1(b). After an aggressive start, the change in weights is subtle for most of training. Due to the large number of inputs, each individual weight is relatively small, as only the total sum is relevant to the timing of the output spike. It should be noted that some weights continue to change throughout the whole of training. These weights, in particular, do not contribute significantly to any symbol in the training library and, therefore, have limited data when making weight adjustments.

After about 10 epochs, the trained neural network will produce a spike within a 10 ps widow of the target time when the symbol is recognized, as shown in Fig. 5.2.

Several examples of incorrect symbols serving as input and the resulting output spikes are shown in Fig. 5.4. By spiking outside the target time window for any symbol other than the correct symbol, the neural network has high accuracy in recognizing the chosen symbol. Whether additional or missing pixels serve as the difference from the correct image does not matter in making a spike outside of the target time window.

To gain a more complete understanding of how weights change when training with the "Z" symbol, a distribution of weights is plotted in Fig. 5.5. Figure 5.5(a) shows the random distribution of weight at the beginning of training, and Fig. 5.5(c) shows the weights at the end of training after 60 epochs. Figure 5.5(b), in contrast, shows the training in the middle of training after 10 epochs. It is evident from this sequence that as training progresses, the weights are adjusted in such a way that the “Z” symbol is reflected

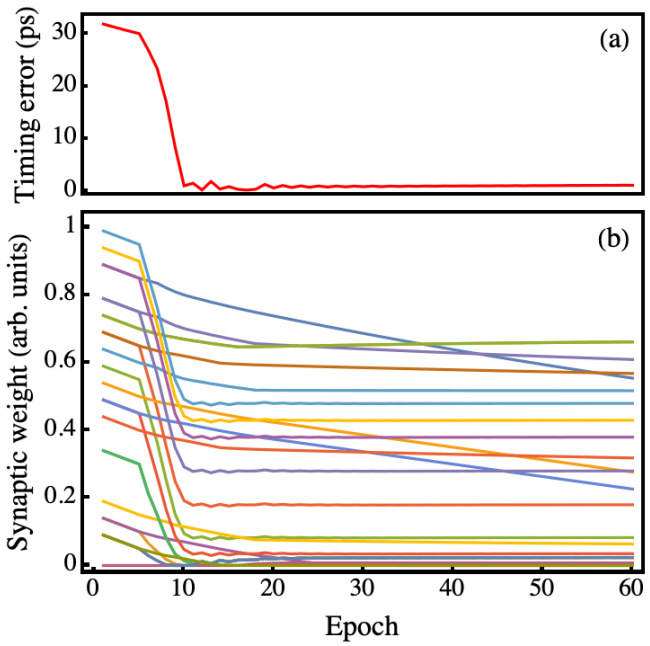

Figure 5.3: Simulations depicting the training process of an AFM SPAN. (a) Time difference between the target and actual spike times of the AFM SPAN's output over 60 epochs of training. (b) Each colored line illustrates the evolution of an individual synaptic weight from an input neuron to the AFM SPAN over 60 epochs of training.

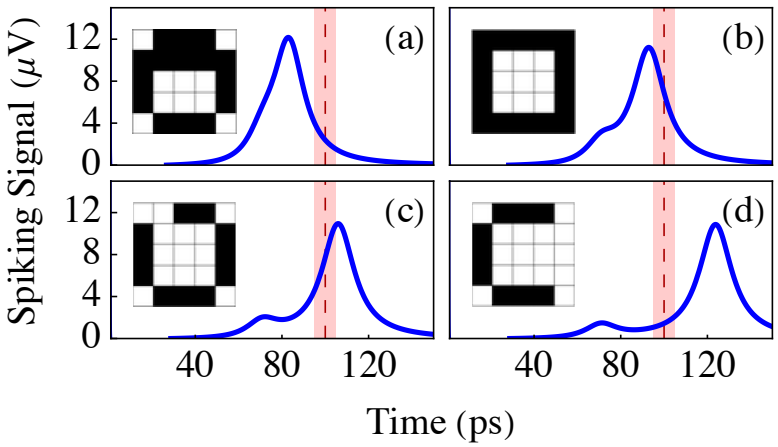

Figure 5.4: Simulation result of the output spikes of a trained AFM SPAN for different incorrect symbols, shown by insets. The dashed line represents the target time, and the red shading illustrates a 10 ps time window surrounding the target time. The simulated response for each incorrect symbol is outside the target time window, indicating that the inputted symbol is recognized to be not the correct symbol. (a,b) Input symbols have additional pixels. (c,d) Input symbols have missing pixels.

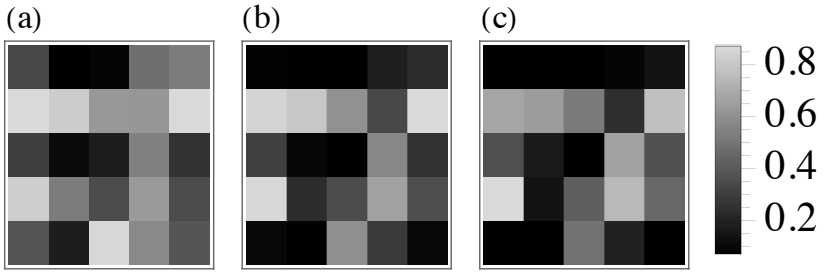

Figure 5.5: Distribution of weights connecting inputs to the AFM SPAN (a) at the beginning of training, (b) in the middle of training, (c) at the end of training.

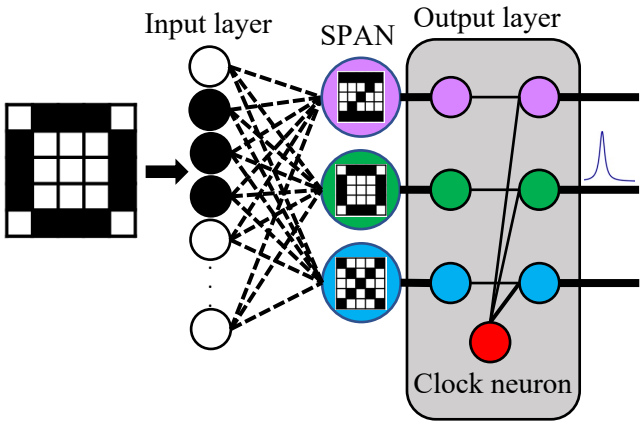

Figure 5.6: Architecture of a 3 AFM SPAN neural network. The input symbol is encoded in the spiking pattern of the input layer neurons. During training, the synaptic weights between the input neurons and each SPAN are adjusted individually as each SPAN is trained to recognize a different symbol. The weights of the output layer are weakened such that a single spike cannot propagate to the next neuron. The red neuron represents a clock neuron that spikes at the target time, combining with the SPAN corresponding to the recognized symbol to generate a sufficiently strong signal for the post-synaptic neuron to fire.

in the weight distribution. As there is little difference between Fig. 5.5(b) and Fig. 5.5(c), it can be assumed that the most significant training happens in the first 10 epochs.

Multiple AFM SPANs, trained to recognize different symbols, can be connected to the same layer of input neurons. This way, the SPAN trained to the input symbol will produce a spike within the target time window, while the others would spike outside it. With multiple SPANs all spiking at different times, the output can be unclear. Therefore, it would be convenient to clear the output by suppressing output spikes outside the target time window. This can be done by creating an additional output layer that consists of fixed synapses. The architecture of the neural network capable of suppressing unwanted outputs is shown in Fig. 5.6.

The input neurons are connected to three SPANs via trainable weights. These SPANs are each trained to recognize different symbols. The SPANs then serve as input to the output layer. The output layer's synapses have weak coupling, such that a single pre-synaptic spike is insufficient to cause a spike in the post-synaptic neuron. Two spikes must happen simultaneously to produce a strong enough signal for a post-synaptic spike.

The red neuron, shown in Fig. 5.6, is a clock neuron spiking at the target time. The clock neuron receives an input independent of the input layer's symbol. This independent input causes the clock neuron to generate a spike at the target time. Therefore, when a symbol is recognized, the corresponding SPAN will spike along with the clock neuron at the target time. These two signals are enough to overcome the weak coupling and cause the post-synaptic neuron to fire. The spikes from the SPANs that do not correspond to the input symbol would spike away from the target time, thus not combining with the clock neuron to cause an output spike. This output layer ensures that only the spike from the SPAN corresponding to the correct symbol is outputted. The output spiking signals of this neural network are shown in Fig. 5.7.

The blue, green, and magenta spikes correspond to three different SPANs trained to three different symbols, while the red spike is the clock neuron spiking at the target time. At this time, there are spikes of the clock neuron and a single SPAN corresponding to the inputted symbol. These two spikes combine to send a single spike to the output, indicating which symbol has been recognized. Therefore, this output layer creates an output that clearly identifies the recognized symbol.

The training time of the AFM SPAN neural networks for such relatively small images is very short, about 10 epochs with a 20-symbol library. Due to the high speed of AFM neurons (200 ps between inputting a symbol and the output neuron firing), this training session may last for only ≈ 40 ns of real-time. As discussed in section 3.1, the energy consumption of a single AFM neuron is calculated to be about 10^{-3} pJ per

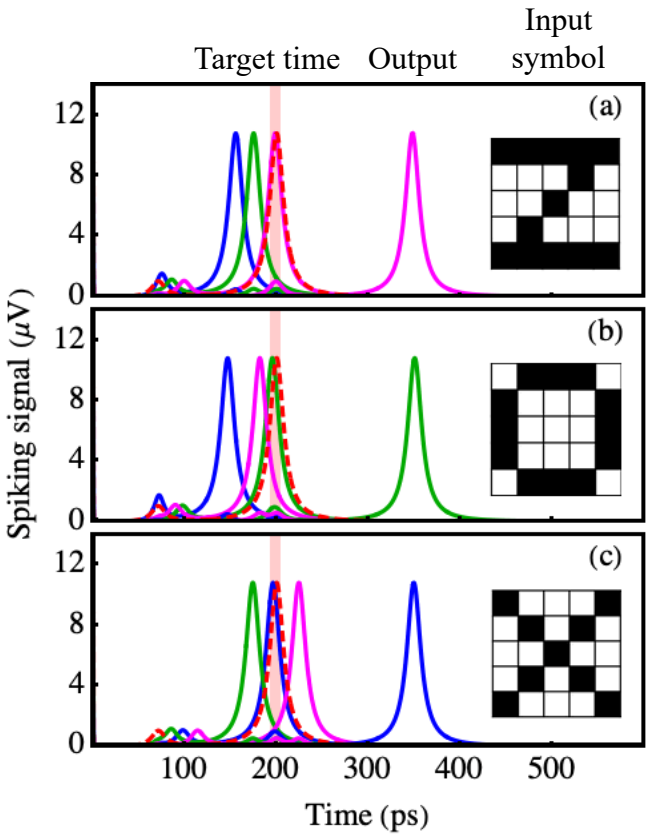

Figure 5.7: Simulated result of a 3 SPAN (pink, green, blue) neural network for 3 different input symbols (Z, O, X). The red shading represents a 10 ps time window surrounding the target time. The SPAN corresponding to the recognized symbol generates a spike within the target time window, along with the clock neuron (red dashed spike), resulting in a single output spike. The color of the output spike corresponds to the SPAN that was trained to recognize the inputted symbol.

synaptic operation. To successfully train a single SPAN, the total energy consumption of the AFM neural network is 31.2 pJ.

The use of the SPAN algorithm leads to a very simple, one-layer neural network. This neural network is limited in its ability to perform more complex tasks as a result of such simplifications. For example, the MNIST data set of handwritten digits, commonly used for neural network training, is encoded in 28×28 pixel grids. It is unlikely that the AFM SPAN neural network would be able to cope with inputs on this scale. However, even the simple network described in this section may find practical applications when high training, operation speed, and/or low power consumption are required. The simple neural network used in this section demonstrates for the first time that AFM neurons are capable of being used for neuromorphic tasks such as pattern recognition.

5.2 Gradient descent algorithm

The use of the SPAN algorithm for training AFM neurons for pattern recognition proved successful as shown by the previous section. However, the simplicity of the approach imposed limitations on the computational power of the neural network. To advance pattern recognition with AFM neurons, it is imperative to replace the SPAN algorithm with a more complex approach. Several differences arise when replacing the SPAN algorithm, including the transition to multilayer neural networks and the introduction of working memory.

Section 2.2.1 provides a concise introduction to the widely-used backpropagation algorithm for multilayer ANNs. During backpropagation, inputs traverse through a feed-forward neural network, starting from the input layer and progressing through hidden layers to the outputs. Once the inputs are fully processed, an error or loss function is calculated from the outputs. As backpropagation operates as a supervised learning algorithm, inputs are paired with desired outputs, making the error function a measure of the difference between actual and target outputs. The gradient of the error function is then

used to adjust the weights of the ANN, facilitating a process known as gradient descent to steer actual outputs toward the target outputs.

As outlined in section 2.2.2, direct application of the backpropagation algorithm to SNNs poses challenges due to their communication via undifferentiable spikes. Early attempts to adapt backpropagation for SNNs utilized temporal encoding, similar to the SPAN algorithm, wherein the precise timing of spikes was leveraged for error function computation [126]–[128]. However, alternative methods for encoding information in SNNs exist. The backpropagation algorithm employed for training AFM neural networks adopts rate-based encoding, wherein the firing rate of an output neuron is utilized for error calculation [205]. The spiking activity between connected neurons is defined as,

$$R_j(t) = \frac{1}{n}\sum_i w_{ji}\, R_i(t), \tag{5.2}$$

where n is the number of presynaptic neurons i. The weights w_{ji} are the strength of the connections between the presynaptic neurons i and the postsynaptic neuron j. This form is equivalent to the coupling term, $\sum_i \kappa_{ij}\dot{\phi}_j$, in the coupled AFM neuron equation, Eq. (3.5).

The neural network uses a least mean squared error, defined as the difference between the actual fire rate of the output neurons, R_o^a, and the target fire rate, R_o^d,

$$E(R_o^a) = \frac{1}{2}\sum_o (R_o^a - R_o^d)^2. \tag{5.3}$$

To minimize the network error, the weights are modified using the process of gradient descent,

$$\Delta w_{ij} = -\eta \frac{\partial E(R_j^a)}{\partial w_{ij}}, \tag{5.4}$$

where η is the learning rate. The weights of the multilayer neural network are then updated starting with the output layer and traveling backward through the SNN, hence the name backpropagation.

5.3 Two layer neural network

The first ensure that a gradient descent algorithm can be used to train AFM neurons, a simple 2-layer neural network is constructed. This network comprises a hidden layer and an output layer, as depicted in Fig. 5.8(a), with both layers fully connected via synaptic weights that will undergo adjustments during training. To evaluate the effectiveness of the gradient descent algorithm, four binary spiking patterns that correspond to the four outputs are encoded into input neurons: '1111', '1101', '1010', and '1100'. For instance, the pattern '1101' signifies that the 1st, 2nd, and 4th input neurons fire while the 3rd does not. This is illustrated in Fig. 5.8(b), where the input neurons fire a single spike within a specified time window. Throughout each training epoch, variations of each pattern are generated and processed by the neural network. These variations involve differences in the delay between the input neurons and the hidden layer. Subsequently, spikes propagate through the neural network, and the error is calculated at the outputs. Finally, the change in synaptic weights is determined using gradient descent.

5.3.1 Methods

Substituting the rate equation Eq. (5.2) and the error equation Eq. (5.3) into the gradient descent equation Eq. (5.4), the change of weights for the output layer and input layer takes the forms,

$$\Delta w_{oh} = -\eta \frac{1}{n_h} \left[R_o^a - R_o^d \right] R_h, \tag{5.5}$$

$$\Delta w_{hi} = -\eta \frac{1}{n_h \, n_i} \sum_O \left[R_o^a - R_o^d \right] R_i \, w_{oh}, \tag{5.6}$$

where Δw_{oh} and Δw_{hi} is the change in weight between output neuron o and hidden neuron h and between input neuron i and hidden neuron h, respectively, n_h and n_i are the number of hidden and input neurons, respectively, R_o^a and R_o^d is the actual and target fire rate of output neuron o, respectively, R_h and R_i are the fire rates of hidden neuron h and input

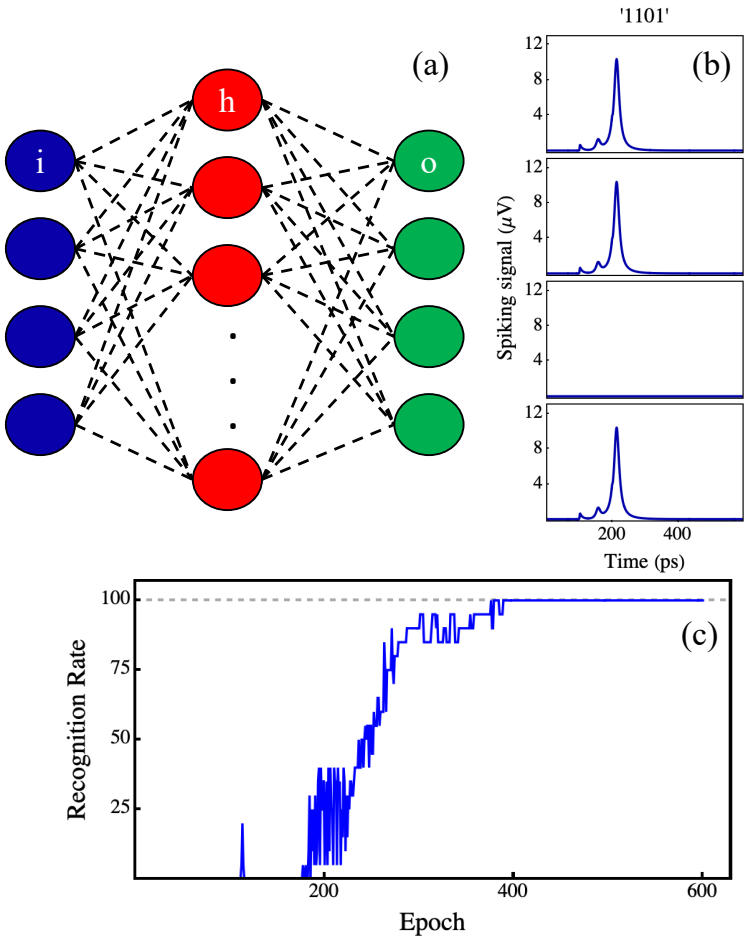

Figure 5.8: Two layer AFM neural network. (a) Architecture of the two layer AFM neural network consisting of 4 input neurons (blue), 10 hidden neurons (red), and 4 output neurons (green). Each layer is fully connected to the previous layer through trainable synapses. (b) Spiking pattern of input neurons for the pattern '1101'. A '1' in the pattern means the associated input neuron fires a single spike within a time window, while a '0' means the input neuron does not fire. (c) Recognition rate of the two-layer AFM neural network for a test set comprised of variations of the 4 input patterns.

neuron i, respectively, and η is the learning rate. Further details on the derivation of the change in weights of the output and input layers can be found in Ref. [205]. Additionally, a summary of constants used in the 2-layer neural network is covered in appendix A.

5.3.2 Results

During each epoch, the accuracy of the updated neural network is evaluated using a test set composed of variations of the four patterns. The recognition rate is depicted in Fig. 5.8(c). It is evident from the figure that this two-layer neural network achieves a 100% recognition rate in approximately 400 epochs. It's worth noting that two of the patterns used in training, '1010' and '1100', have the same number of input spikes, each spiking a total of 2 times. This underscores that the neural network recognizes the entire pattern over four input neurons rather than just the fire rate or count of spikes at the inputs. Without this capability, the trained neural network would struggle to differentiate between patterns with an equal spike count. Like the SPAN neural network, there exists a 300 ps delay between pattern encoding in the input layer and the firing of the output neurons. Thus, this neural network completes a successful training cycle within just 120 ns of real-time, demonstrating an exceptionally rapid process enabled by the THz properties of AFM neurons.

5.4 Two input graph neural network

The 2-layer neural network proves that the gradient descent algorithm can be used to train AFM neurons, but its simplicity comes with drawbacks. Primarily, this layered architecture lacks working memory, as all inputs reach the outputs nearly simultaneously while passing through a single hidden layer. Moreover, the 2-layer neural network fails to leverage any unique properties of AFM neurons. Hence, an alternative neural network structure is required to fully exploit the inertial properties inherent in AFM neurons.

In this new neural network, depicted in Fig. 5.9(a), the hidden layer adopts a directed graph structure. Within this framework, hidden neurons establish random

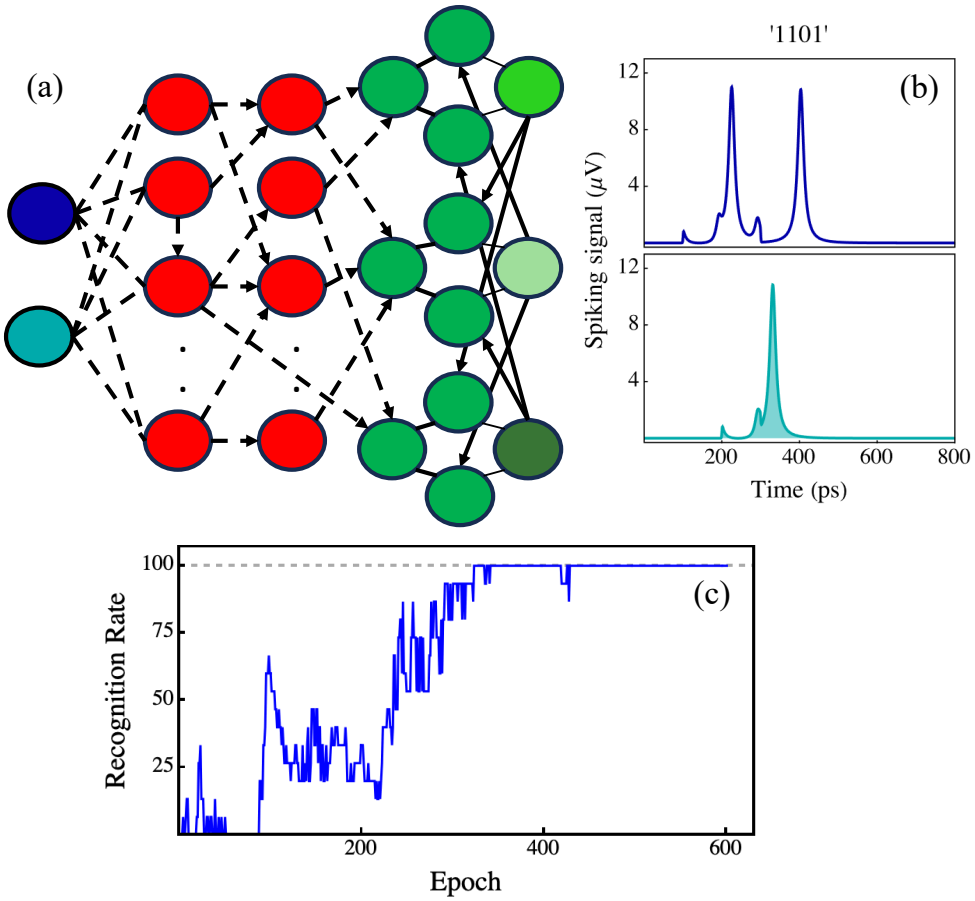

Figure 5.9: Two input graph AFM neural network. (a) Architecture of the two input graph AFM neural network consisting of 2 input neurons (blue, cyan), 20 hidden neurons (red), and 3 outputs in a winner-takes-all circuit (green). (b) Spiking pattern of input neurons for the pattern '1101' where the first input neuron spikes twice and the second input neuron spikes once, forming an overlapping sequence of three spikes in time. (c) Recognition rate of the two input graph AFM neural network for a test set comprised of variations of the 3 input patterns.

connections with other hidden neurons, ensuring the overall network maintains a feed-forward configuration. This means signals always travel towards the outputs with no backward or looping connections. Due to its graph structure, the delay between inputs and outputs takes on random values as some connections within the graph hidden layer may be shorter than others. This allows for a mixing of signals in time, introducing a nonlinear short-term memory.

Using sequential binary encoding, the inputs to the graph neural network are reduced from four neurons to two neurons. Each input neuron may emit 1 or 2 spikes, thereby forming patterns of up to 4 spikes that overlap in time. An example input pattern, '1101', is depicted in Fig. 5.9(b), wherein the first input neuron spikes twice and the second input neuron spikes once.

In the 2-layer neural network, the output layer comprises a single row of neurons, illustrated by the green neurons in Fig. 5.8(a). However, this simplistic output structure is incompatible with the graph neural network. Such a simple output layer in the graph neural network would lead to multiple outputs spiking in response to an input pattern, even post-training. To counteract this effect, the inertial properties of AFM neurons are harnessed. An inhibitor circuit, discussed in detail in section 4.2, is incorporated into each output of the graph neural network, as depicted by the green neurons in Fig. 5.9(a). The outputs of each inhibitor circuit function as the inhibitory signal for the other outputs. This results in a situation where only the first output to be excited is recorded while the others are suppressed. This is commonly referred to as a Winner-Takes-All (WTA) output. The WTA output layer is one example of the graph neural network using the inertial properties of AFM neurons. The weights of this WTA output layer are fixed and not altered during training.

Training this graph neural network progresses in the same way as the 2-layer neural network, where a variation of each pattern is created and processed by the neural

network during each epoch. Unlike the 2-layer neural network, however, the graph neural network comprises three distinct layers that undergo training. The following paragraphs will detail how gradient descent is used to update the weights of each layer.

5.4.1 Methods

The directed graph neural network consists of input neurons I, hidden neurons H, and output neurons O. The change in weights between the hidden layer and output layer follows the same form as the 2 layer neural network and has the form,

$$\Delta w_{oh} = -\eta \frac{1}{n_h} \left[R_o^a - R_o^d \right] R_h. \tag{5.5}$$

In contrast to the 2 layer neural network, the graph neural network has hidden neurons that have connections to other hidden neurons. Hence, there needs to be a rule for the change in weight of these hidden connections. As before, it starts with the gradient of the error function,

$$\Delta w_{h''h'} = -\eta \frac{\partial E(R_o^a)}{\partial w_{h'h''}}, \tag{5.7}$$

where $w_{h''h'}$ is the weights from hidden neuron h' to hidden neuron h''. The derivative is expanded using the chain rule,

$$\frac{\partial E(R_o^a)}{\partial w_{h''h'}} = \frac{\partial E(R_o^a)}{\partial R_{h''}} \frac{\partial R_{h''}}{\partial w_{h''h'}}. \tag{5.8}$$

As shown in Ref. [205], the first factor on the right-hand side of the above equation is expanded in the same way as the 2-layer neural network,

$$\frac{\partial E(R_o^a)}{\partial R_{h''}} = \sum_O \frac{\partial E(R_o^a)}{\partial R_o^a} \frac{\partial R_o^a}{\partial R_{h''}}. \tag{5.9}$$

The first term can be calculated using the error equation Eq. (5.3),

$$\frac{\partial E(R_o^a)}{\partial R_o^a} = R_o^a - R_o^d, \tag{5.10}$$

where R_o^a and R_o^d are the actual and target firing rate of output neuron o, respectively.

The second factor is solved using the rate equation Eq. (5.2),

$$\frac{\partial R_o^a}{\partial R_{h_b}} = \frac{1}{n_h} w_{oh}, \tag{5.11}$$

where n_h is the number of hidden neurons.

Together, Eq. (5.9) transforms to,

$$\frac{\partial E(R_o^a)}{\partial R_{h_b}} = \frac{1}{n_h} \sum_o \left[R_o^a - R_o^d \right] w_{oh}. \tag{5.12}$$

The second term in Eq. (5.8) is also found using the rate equation Eq. (5.2),

$$\frac{\partial R_{h''}}{\partial w_{h''h'}} = \frac{1}{n_h} R_{h'}. \tag{5.13}$$

Combining Eqs (5.12) and (5.13), the final formula for the change in weights in the hidden layer is,

$$\Delta w_{h''h'} = -\eta \frac{1}{2n_h} \sum_O \left[R_o^a - R_o^d \right] R_{h'} \; w_{oh}. \tag{5.14}$$

Finally, the change in weights from the input layer to the hidden layer is found using the same method. Gradient descent is applied to the weights of the hidden layer such that,

$$\Delta w_{hi} = -\eta \frac{\partial E(R_o^a)}{\partial w_{hi}}, \tag{5.15}$$

where w_{hi} is the weight from input neuron i to hidden neuron h.

The derivative is again expanded via the chain rule,

$$\frac{\partial E(R_o^a)}{\partial w_{hi}} = \frac{\partial E(R_o^a)}{\partial R_h} \frac{\partial R_h}{\partial w_{hi}}. \tag{5.16}$$

The first term in Eq. (5.16) is expanded with the chain rule similar to how it was done in Eq. (5.9) for the hidden layer. However, not only the interaction between the hidden layer and the output layer is considered, but also the interaction between the

hidden neurons with themselves,

$$\frac{\partial E(R_o^a)}{\partial R_h} = \sum_O \sum_H \frac{\partial E(R_o^a)}{\partial R_o^a} \frac{\partial R_o^a}{\partial R_h} \frac{\partial R_{h'}}{\partial R_{h''}}. \tag{5.17}$$

The first term has been found many times to be Eq. (5.10). The second and third terms are calculated from Eq. (5.2),

$$\frac{\partial R_o^a}{\partial R_h} = \frac{1}{n_h} w_{oh}, \tag{5.18}$$

$$\frac{\partial R_{h'}}{\partial R_{h''}} = \frac{1}{n_h} w_{h''h'}. \tag{5.19}$$

Together, Eq. (5.17) transforms in to,

$$\frac{\partial E(R_o^a)}{\partial R_h} = \frac{1}{2n_h} \sum_O \sum_H \left[R_o^a - R_o^d \right] w_{oh}\, w_{h''h'}. \tag{5.20}$$

The second term in Eq. (5.16) found using the rate equation,

$$\frac{\partial R_h}{\partial w_{hi}} = \frac{1}{n_i} R_i. \tag{5.21}$$

Combining Eqs (5.20) and (5.21), the final formula for the weight changes between the input layer and the graph hidden layer is,

$$\Delta w_{hi} = -\eta \frac{1}{2n_i n_H} \sum_O \sum_H \left[R_o^a - R_o^d \right] R_i\, w_{oh}\, w_{h''h'}. \tag{5.22}$$

In summary, to train the directed graph neural network, the formulas for the modification in weights for all three layers are as follows,

$$\Delta w_{oh} = -\eta \frac{1}{n_h} \left[R_o^a - R_o^d \right] R_h, \tag{5.5}$$

$$\Delta w_{h''h'} = -\eta \frac{1}{2n_h} \sum_O \left[R_o^a - R_o^d \right] R_{h'}\, w_{oh}, \tag{5.14}$$

$$\Delta w_{hi} = -\eta \frac{1}{2n_i n_H} \sum_O \sum_H \left[R_o^a - R_o^d \right] R_i\, w_{oh}\, w_{h''h'}. \tag{5.22}$$

A summary of constants used in the graph neural network is outlined in appendix A.

5.4.2 Results

Similar to the 2-layer neural network, the accuracy of the trained graph neural network is evaluated using a test set comprising variations of the three patterns used in training: ‘1111’, ‘0011’, and ‘1100’. The recognition rate is depicted in Fig. 5.9(c). This directed graph neural network achieves a 100% recognition rate in approximately 450 epochs. Once again, two of the patterns utilized in training exhibit the same total number of spikes; ‘0011’ and ‘1100’ each spike twice. The achievement of a 100% recognition rate demonstrates the graph neural network’s proficiency in distinguishing patterns with an equal count of input spikes. The trained neural network can take up to 800 ps to fully process an input pattern from the input layer to the output layer. Therefore, only 360 ns of training is required to reach 100% accuracy.

The key feature emerging from the directed graph design is a working memory that harnesses the inertial properties of AFM neurons. This working memory can be illustrated by plotting the neural network’s outputs at different times during training, shown in Fig. 5.10. The top panel, Fig. 5.10(a), illustrates the pattern ‘1111’ encoded by the input layer, wherein both input neurons spike twice in an overlapping sequence in time. Figure 5.10(b) shows how the outputs react at the beginning of training. Each shade of green represents one of the three outputs. It’s evident from this figure that at the beginning of training, the outputs react randomly, with some even spiking before the inputs have finished. This behavior is attributed to the presence of ultra-short connections between inputs and outputs in the graph hidden layer. From Fig. 5.10(c), depicting the outputs during the midpoint of training, it becomes evident how the neural network strives not only to decrease the number of spiking outputs but also to delay their activation. By the end of training, as shown in Fig. 5.10(d), only a single output spikes well after the

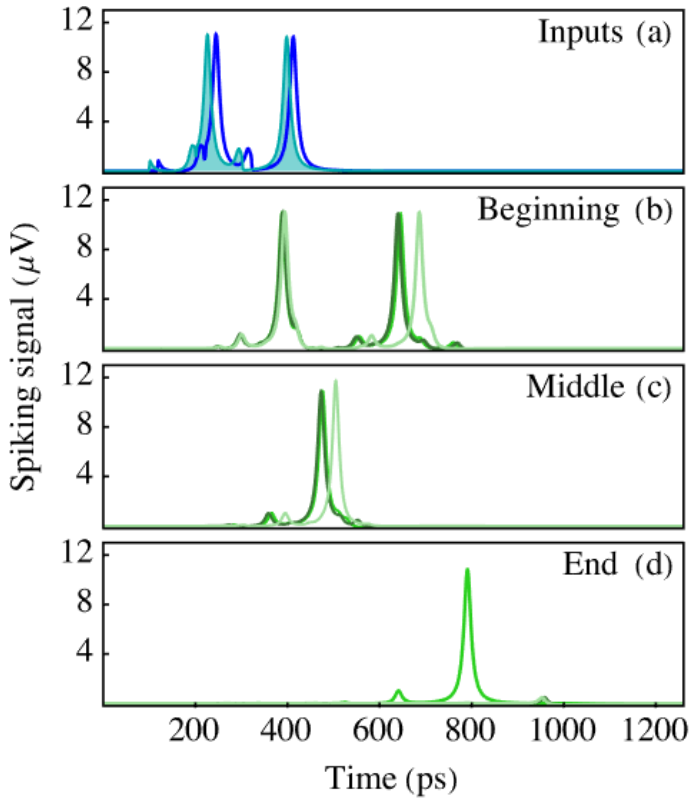

Figure 5.10: Simulated inputs and outputs to the graph neural network at different points of training. (a) Input spike pattern '1111' to the graph neural network from two input neurons that each spike twice. (b-d) Output spike pattern of a graph neural network (b) at the beginning, (c) middle, and (d) end of training.

inputs have finished, signaling successful pattern recognition. This depiction illustrates how the training process of the graph neural network adjusts the inertial delay inherent in AFM neurons, allowing the neural network sufficient time to thoroughly process the inputs before triggering the outputs. This suggests that the hidden layer possesses a form of working short-term memory.

5.5 One input graph neural network

The 2-input graph neural network presents an intriguing scenario wherein sequential rate encoding is employed, allowing the neural network's inputs to be reduced from four neurons to two neurons. This raises the question: Can this encoding scheme further reduce the number of inputs? Such a scenario is explored with the introduction of a single input graph neural network, as depicted in Fig. 5.11(a). In this neural network, patterns are encoded as temporal sequences of up to four spikes emitted by a single input neuron. An example input spiking pattern of the sequence '1111' is illustrated in Fig. 5.11(b).

The hidden layer of this 1-input neural network remains in a directed graph structure with a slight modification. As depicted in Fig. 5.10(b), the presence of ultra-short connections in the graph hidden layer causes the outputs to fire prematurely, even before the inputs have completed spiking. With a sequence of up to four spikes in time, these short connections will always result in outputs firing prematurely. To mitigate this issue, an additional layered structure is introduced to the hidden layer. The internal graph layers are labels A, B, C, and D in Fig. 5.11(a). In contrast to the previous configuration, where hidden neurons close to the inputs (A layer) could be randomly connected to any other hidden neuron, including those near the outputs (D layer), the 1-input neural network imposes additional restrictions. In this network, hidden neurons proximal to the inputs in layer A are linked exclusively to other neurons in the same layer or in the adjacent two layers, B and C. These connections are illustrated by the blue lines

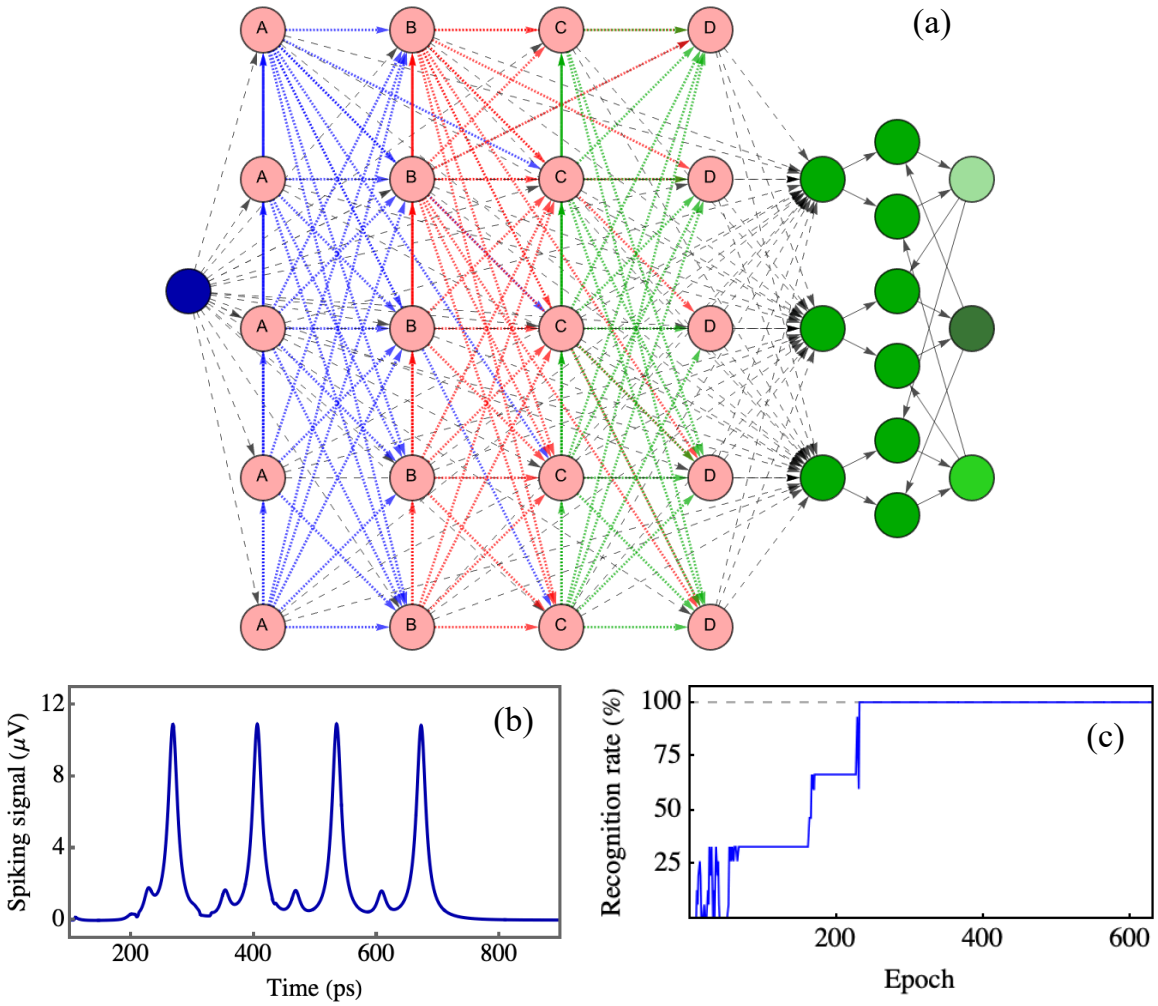

Figure 5.11: One input graph AFM neural network. (a) Architecture of the one input graph AFM neural network consisting of 1 input neuron (blue), 20 hidden neurons (red), and 3 outputs in a winner-takes-all circuit (green). Internal layered structures in the graph hidden layer are represented by groups of neurons labeled A, B, C, and D. Connection emanating from layer A are depicted in blue, from layer B in red and from layer C in green. (b) Spiking pattern of the input neuron for the pattern '1111', where the input neuron spikes four times in one sequential sequence. (c) Recognition rate of the one input graph AFM neural network for a test set comprised of variations of the 3 input patterns.

in Fig. 5.11(a). Similarly, neurons in layer B are linked to neurons also in layer B or neurons in the next two layers, C and D (red lines). Then, neurons in layer C may only be connected to neurons in layer D, depicted by the green lines. Consequently, this elongates the connections between inputs and outputs, requiring them to traverse multiple layers of hidden neurons. This modified structure effectively enables the neural network to demonstrate short-term memory akin to that observed in the 2-input neural network illustrated in Fig. 5.10.

The training of the 1-input graph neural network proceeds in the same manner as the 2-input graph neural network. The weight modification follows the same formulas as the previous network: Eq. (5.5) for the output layer, Eq. (5.14) for the hidden layer, and Eq. (5.22) for the input layer. During training, variations of the input patterns are presented to the neural network, and its accuracy in recognizing these patterns is continuously evaluated. This process is depicted in Fig. 5.11(c), where the recognition rate of the neural network for a test set consisting of various input pattern variations is illustrated. The 1-input neural network achieves a 100% recognition rate in approximately 300 epochs. The neural network requires 1000 ps to fully process a pattern from inputs to outputs. Consequently, the neural network is successfully trained within a mere 300 ns, underscoring the efficiency and rapidity of the training process.

5.6 Conclusion

In conclusion, this chapter detailed two instances of training AFM neural networks for pattern recognition. The SPAN algorithm and neural network was the first example of successful pattern recognition by AFM neurons. However, its simplicity limits the computational power of the resulting neural network. A simple 2-layer neural network was used to prove that a rate encoding gradient descent algorithm can be used to train AFM neurons. Although it did prove successful, the layered structure does not use any unique properties of AFM neurons. The directed graph design of the hidden layer allows

for the creation of neural networks with working short-term memory. The graph design employs unique features of AFM neurons and allows for the reduction of input neurons using sequential encoding.

CHAPTER SIX

BIOLOGICAL NEURAL NETWORK MODELING

This chapter will explore how AFM neurons can be used to model biological neural networks. Human behavior, physiological function, and anatomical performance are all governed by the neurons running throughout our bodies. These neurons collectively form the central nervous system, encompassing the brain and spinal cord, as well as the peripheral nervous system, which establishes connections between the central system and the rest of the body [206]. The interconnections between the peripheral and central nervous systems are highly complex, presenting significant challenges in comprehending their intricate mechanisms.

Many works have focused on modeling various biological neural networks connecting the peripheral and central nervous systems, aiming to deepen our understanding of their complex mechanisms [207]–[209]. Artificial recreations of biological neural networks can, in principle, be used to restore sensations lost by individuals with sensory loss caused by neuronal damage. Artificial neural networks also offer the potential for medical prosthetics to exhibit sensations and actions, both voluntary and involuntary, that closely resemble those of biological systems.

Additionally, implementing realistic ANNs in modern electronics holds the potential to further the development of bioinspired artificial intelligence and robotics [210]–[214]. By studying neuroscience, it is possible that the next generation of behavior-based robotics could interact with their environment and demonstrate self-preservation capabilities similar to that of humans. Furthermore, bio-inspired ANN offer advantages such as reduced power consumption and high-speed training, which could revolutionize the future of robotics.

In order to replicate the connections found in human bodies, these models use artificial neurons designed to function similarly to their biological counterparts. For example, biological neurons generate voltage spikes known as action potentials in response to external stimuli that surpass an intensity threshold. Artificial neurons strive to replicate these action potentials through similar voltage spikes that are generated only after a threshold is surpassed. Current neuromorphic chips use silicon-based transistors as spiking artificial neurons [16]. However, these neurons lack features that make biological neurons unique, such as spike profile, response latency, inhibition, and refractory periods. Section 3.4 discusses how the properties of AFM neurons resemble those of biological neurons. Due to these similarities in the unique features of AFM neurons, they make an excellent candidate for modeling biological neural networks.

In this chapter, we use AFM neurons to simulate the biological neural network responsible for the withdrawal reflex. The withdrawal reflex is a polysynaptic spinal reflex that protects the body from noxious or harmful stimuli [215]. Simulating withdrawal reflex mechanisms consists of five distinct scenarios: muscle tone, voluntary movement, responses to both weak and strong sensory stimuli, and the inhibition of reflexes. Our simulations demonstrate the high effectiveness of AFM neurons in reproducing responses of biological neural networks to various stimuli. To a large extent, this stems from the inertial properties of AFM neurons and is related to the possibility of a simple implementation of inhibitory neural connections [21], which are vital for many biological functions. As a result, the five distinct scenarios of the withdrawal reflex can be simulated with the AFM neural circuit containing less than 50 neurons.

This chapter starts with an overview of the withdrawal reflex, detailing its functions through five defined scenarios. It then compares the mathematical model for biological neurons with the AFM neuron model. Next, it introduces the AFM withdrawal neural network, and the chapter concludes by presenting the simulation results of the five

withdrawal reflex scenarios. The results discussed in this chapter were previously presented in paper [28] and conference presentations [32], [33], [35], [38], [41].

6.1 The withdrawal reflex

The withdrawal reflex is a polysynaptic spinal reflex that responds to noxious or painful stimuli by stimulating the flexion of agonist muscles and inhibiting the extension of antagonist muscles of the same limb [215]. By contracting one muscle and relaxing the opposing one, the withdrawal reflex removes a limb from the harmful stimulus.

The withdrawal reflex neural network, known as the reflex arc, involves neural pathways through the spinal cord. The reflex arc consists of sensory neurons, interneurons, and motor neurons. Sensory neurons respond to the environment by outputting spike trains with different frequencies. Interneurons in the spinal cord are able to stimulate muscles without the need for signals to travel to the brain, thereby enabling a more rapid response. Motor neurons control the muscles causing either contraction or relaxation.

Sensory neurons are part of the peripheral nervous system and are known as nociceptors, which alert the body to painful stimuli from the environment [216]. The neurons react to a noxious stimulus by creating a train of action potentials, where the frequency of the spike train is used to encode the strength of the stimulus. Through this frequency encoding, a high-frequency spike train means a more painful and damaging stimulus [217].

The critical components of the withdrawal reflex neural network are the excitatory and inhibitory interneurons located within the spinal cord [218]. These interneurons play a pivotal role by either stimulating or inhibiting the motor neurons, thereby triggering muscle contraction or relaxation.

Finally, motor neurons are categorized into two types: agonist neurons, responsible for muscle contraction, and antagonist neurons, which induce inhibitory signals, leading to muscle relaxation [219]. The simultaneous contraction and relaxation

of the muscles cause the limb to move in one direction. The collective operation of several neurons and the existence of different response regimes make the withdrawal reflex very interesting for simulations. The withdrawal reflex arc forms a static neural network capable of exhibiting five distinct scenarios without requiring modifications to its configuration. These scenarios encompass muscle tone, voluntary motion, responses to both weak and strong sensory stimuli, and reflex inhibition. Despite its simple architectural design, the neural network's functions showcase complexity, making it an ideal candidate for simulating with artificial neurons.

In the absence of external sensory stimulus, the muscle must remain engaged. To keep the muscles engaged and ready for movement, the brain constantly sends signals to the motor neurons; this is called the tone [220], [221]. Muscle tone is a constant muscular activity that is necessary background for actual movement. The tone stems from the autonomic nervous system, which is a collection of nerves alongside the brain that will fire signals to maintain muscle functionality.

In order to gain a comprehensive understanding of the withdrawal reflex, it is essential to compare it with a control scenario. This control scenario corresponds to uninterrupted voluntary limb movement. In the absence of sensory input, the brain emits signals to the motor neurons, eliciting coordinated muscle contractions and relaxations, consequently resulting in limb movement.

Similar to many neuronal pathways, the initiation of the withdrawal reflex relies on sensory neurons responding to environmental stimuli. Sensory neurons transmit signals to the brain and spinal cord after receiving stimulation from the environment. Weak sensory input, corresponding to a nonharmful stimulus, will be sent to the brain, which, in turn, will stimulate the motor neurons to move the limb. In contrast, if the sensory input is strong, as in the case of a very painful stimulus, the information will bypass the brain and travel through a shorter, faster path via the spinal interneurons. The interneurons will then

directly stimulate the motor neurons, causing limb movement and triggering a much faster involuntary withdrawal response [215].

The inhibition of a reflex is the last scenario that makes the withdrawal reflex unique and interesting to study. Biological neurons can be suppressed by a second input through inhibitory synapses, which reduces the likelihood of a neuron firing by reducing the membrane voltage further away from the threshold [200], [201]. As a result, even if the sensory signal is strong enough to trigger the withdrawal reflex through the interneurons, the cortical neurons of the brain possess the capability to inhibit these interneurons, resulting in the voluntary suppression of the reflex. To fully counteract the reflex, the brain must send voluntary signals to the motor neurons, causing the opposite reaction in the muscles; the agonist muscles relax while the antagonist muscles contract. Now, rather than being pulled away from the harmful stimulus, the limb remains in contact with it. An example of voluntary suppression of the withdrawal reflex is purposely holding one's hand on a hot stove despite the pain and heat sensory information transmitted from sensory neurons to the brain. While difficult, higher-level impulses from the brain have the capacity to alter reflex responsiveness.

The collective operation of multiple neurons and the existence of five different response regimes make the dynamic modeling of the withdrawal reflex neural network interesting but challenging to study. In this chapter, we will show, via numerical simulations, that AFM neurons are capable of fully modeling all aspects of the withdrawal neural network.

6.2 The Hodgkin-Huxley comparison

Unlike many conventional, non-inertial, artificial neurons, AFM neurons have a number of features that closely resemble biological neurons, such as spike profile, response latency, and refraction time [26], [160]. These features were explored in detail in Chapter 3. Therefore, it is interesting to compare the AFM neuron model, governed by

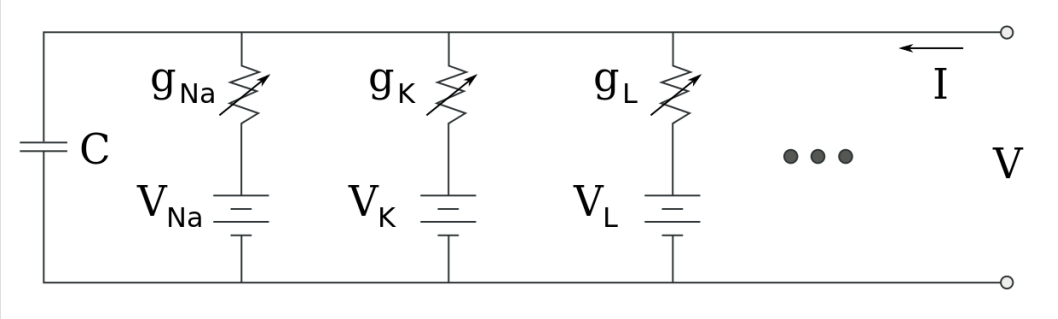

Figure 6.1: Circuit diagram of the Hodgkin-Huxley model of a biological neuron. Aspects of the biological neurons are represented by equivalent electrical components.

Eq. (2.24) and repeated here for convenience,

$$\frac{1}{\omega_{ex}}\ddot{\phi} + \alpha\dot{\phi} + \frac{\omega_e}{2}\sin 2\phi = \sigma I, \tag{2.24}$$

to a model describing a biological neuron.

The Hodgkin-Huxley model is a mathematical model that describes how action potentials in biological neurons propagate [118]. This model treats each component of biological neurons as an electrical element and has the form,

$$C_m\frac{dV_m}{dt} + g_l\left(V_m - V_l\right) + g_K\left(V_m - V_K\right) + g_{Na}\left(V_m - V_{Na}\right) = I, \tag{6.1}$$

where I is the total membrane current, C_m is the membrane capacitance, g_{Na} and g_K are the potassium and sodium conductance, respectively, V_K and V_{Na} are the potassium and sodium reversal potentials, respectively, g_l and V_l are the leak conductance and leak reversal potential, respectively, V_m is membrane voltage, and t is time. These components form an electrical circuit, depicted in Fig. 6.1, made to model biological neurons.

A relation between the terms in Eq. (2.24), which describe the dynamics of the AFM neurons, and the terms in the Hodgkin-Huxley model, Eq. (6.1), can be made.

The membrane voltage in the Hodgkin-Huxley equation, V_m, is equivalent to the angular velocity, $\dot{\phi}$, in the AFM neuron equation because the velocity of the sublattices is used to calculate the output voltage of a neuron through Eq. (2.28). This implies that the first term of Eq. (6.1), where the derivative of V_m is taken, is analogous to the first term of Eq. (2.24), which has a second derivative of ϕ. Thus, the membrane capacitance, C_m, is the inertial term in the Hodgkin-Huxley equation and is equivalent to the exchange energy term, $1/\omega_{ex}$, in the AFM neuron equation.

The second term in Eq. (6.1), g_l, describes the leakage of ions away from the neuron. This leaky current represents the resistance in the membrane voltage as it builds to the threshold resulting in a delay of the action potential spike. This serves the same purpose as the Gilbert damping term, α, in Eq. (2.24). Both terms include the voltage of the neuron and serve to slow the progress of a spike.

The total membrane current, I, on the right-hand side of Eq. (6.1), is equivalent to the coupling term on the right-hand side of the AFM neuron coupled model, Eq. (3.5), where multiple AFM neurons are connected via κ_{ik}. This coupled equation and coupling term were detailed in section 3.3.1. The membrane current in the Hodgkin-Huxley equation is the impulse into the neuron that starts the flow of ions and the build to an action potential. This corresponds to the coupling between AFM neurons, where the output of one neuron serves as the above threshold pulse to elicit another action potential in the next neuron.

The critical components of the Hodgkin-Huxley equation are the ionic conductance, g_K, and g_{Na}. The opening of the ionic channels starts the production of an action potential, and when the threshold voltage is reached, the channels close, and the action potential is fired. The conductances react to the membrane voltage, V_m, with a delay, and therefore, we can think of them as reacting to the integral of the membrane voltage. The flow of ions in these two channels is what prompts the start of an action

potential and what causes the spike profile. This relates to the anisotropy term next to ϕ in the AFM neuron equation in Eq. (2.24), $\frac{\omega_e}{2}\sin(2\phi)$. The anisotropy is responsible for accelerating the AFM sublattices through the easy axis and decelerating them through the hard axis. This acceleration and deceleration are what produce the profile of the spin-pumping voltage spike. Therefore, it is clear that the ionic conduction in the Hodgkin-Huxley equation, Eq. (6.1), is equivalent to the anisotropy term in the AFM neuron equation, Eq. (2.24).

6.3 The withdrawal reflex neural network

The architecture of the AFM neural network realizing the withdrawal reflex is shown in Fig. 6.2. It consists of the sensory neuron, the interneurons in the spinal cord, the motor neurons, and an AFM network simulating brain function. In Fig. 6.2, circles represent neurons, and arrows represent synaptic connections determined by κ in Eq. (3.5). A more detailed view of the neural network, including exact coupling coefficients, is shown in appendix B.

A single AFM neuron can be excited similarly to biological neurons through a positive stimulus and results in an output of a similar voltage spike. However, a single AFM neuron lacks the ability to be suppressed in the same way biological neurons are able to. In order to act as a single biological neuron, multiple AFM neurons are connected in the inhibitor circuit discussed in section 4.2. This circuit can now act as a biological neuron model with the ability to both be excited and inhibited.

The AFM input sensory neuron, the green circle in Fig. 6.2, simulates a nociceptor where the frequency of the spike train encodes the severity of sensory signal, with a higher frequency being a more painful stimulus. In our simulations, the sensory neuron was realized as a single AFM neuron operating in a supercritical regime, i.e., it had the driving current I above the threshold of self-generation I_{th} and continuously produces a spike train at a frequency that is proportional to the current [21], [160]. As the driving current

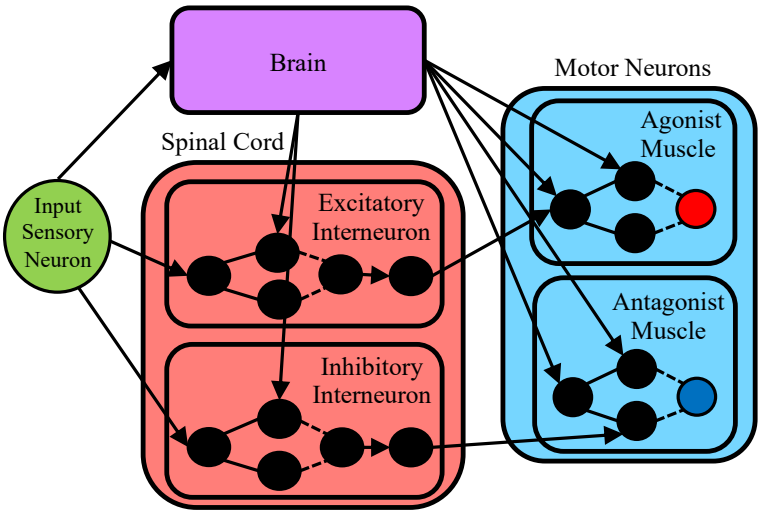

Figure 6.2: Architecture of the AFM withdrawal reflex artificial neural network. The network comprises two interneurons and two motor neurons constructed using inhibitor circuits. The sensory neuron is a single AFM neuron operating in a supercritical regime with variable bias current controlling the frequency of the generated spike train. The architecture of the AFM neural network that simulated brain functions was different in different scenarios described in the text.

increases, the frequency of spikes also increases, enabling the sensory neuron to simulate high-frequency sensory signals for a strong and painful stimulus and low-frequency sensory signals for a weak stimulus. For simulations without sensory inputs (tone and voluntary motion), the sensory neuron is in the subcritical regime where the bias current is reduced below the generation threshold, and no spike train is produced. More details on the bias currents used in the withdrawal reflex neural network are outlined in appendix B.

Similar to the biological neural network, the AFM neural network also contains excitatory and inhibitory interneurons, lying in the pink box representing the spinal cord in Fig. 6.2 [218]. The interneurons receive excitatory input from the sensory neuron. It should be noted that the interneurons are constructed from the inhibitor circuit where the inhibitory signal originates from the “brain” network, which allows for the suppression of

the withdrawal reflex. The weakened coupling of the inhibitor circuits prevents low-frequency signals, stemming from the sensory neuron, from propagating through the interneurons, ensuring that the withdrawal reflex is triggered exclusively by high-frequency, painful sensory signals. This is highly representative of the withdrawal reflex from a physiological standpoint because only noxious stimuli will elicit neuronal action potentials at a frequency and severity that will initiate the biological withdrawal reflex. A strong sensory stimulus causes the excitatory interneuron to send exciting signals to the agonist motor neurons, stimulating muscle contractions. At the same time, the inhibitory interneurons send inhibition signals to antagonist motor neurons, leading to muscle relaxation. As a result, the involuntary withdrawal reflex is triggered by a strong sensory stimulus traveling through the interneurons, causing simultaneous contraction and relaxation of the muscles, moving the limb away from the harmful stimulus.

Inhibitor circuits are also found in the construction of the antagonist and agonist motor neurons, located in the blue box in Fig. 6.2. In this way, both the brain and interneurons can send exciting signals for muscle contractions and inhibition signals for muscle relaxations. The red neuron's output will determine if the agonist muscles were excited or inhibited and the blue neuron's output will determine the antagonist muscles reaction.

At present, it is impossible to dynamically simulate a human brain's operation. Therefore, the AFM neural network modeled brain, the purple box in Fig. 6.2, functions differently in different simulated scenarios. The brain's neural network comprises several delay lines and supercritical input neurons, totaling 26 neurons. Actions independent of the sensory input (e.g., voluntary limb motion) were modeled using supercritical neurons generating continuous spike trains, similar to the sensory neuron. The cognitive delay present in the brain's functions is simulated through a variety of delay lines consisting of

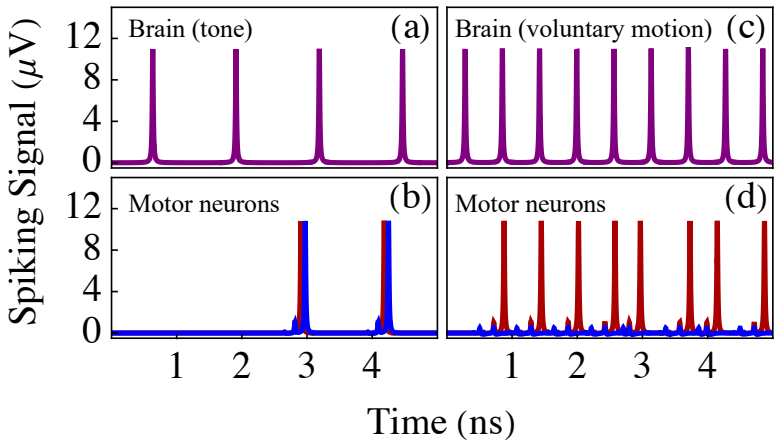

Figure 6.3: Withdrawal reflex simulations in the absence of the sensory stimulus: (a-b) tone and (c-d) voluntary motion. The top row shows the neural signals generated by the brain, purple spike trains, and the bottom row shows the response of motor agonist (red line) and antagonist (blue) neurons.

multiple neurons in chains. The exact architecture of the brain neural network is presented in appendix B.

6.4 Simulation results

Using the AFM neural network shown in Fig. 6.2, five different scenarios that define the withdrawal reflex were simulated. These five scenarios included tone, voluntary motion, response to a weak stimulus, response to a strong stimulus, and reflex inhibition.

6.4.1 Tone

Muscle tone is an essential part of any muscle motion, voluntary or involuntary. To enhance the realism of the withdrawal reflex simulation, the AFM neural network's brain component will consistently transmit a low-frequency signal to the motor neurons, replicating the effect of muscle tone.

The results of simulations of this regime are shown in Fig. 6.3(a) and (b). The top panel, Fig. 6.3(a), shows an example of the purple spike train continuously generated by

the brain network and transmitted to the motor neurons in this scenario. The bottom panel, Fig. 6.3(b), shows the reaction of the red agonist motor neuron (red curve) and blue antagonist motor neuron (blue curve) to the tone signal; as one can see, both motor neurons are weakly and equally excited in this case. These excitations lead to both agonist and antagonist muscles being slightly contracted, resulting in no movement yet maintaining muscle tone.

6.4.2 Voluntary motion

The second simulated scenario is the voluntary limb motion (see Fig. 6.3(c-d)). Similar to the tone simulations, the voluntary motion regimen has no sensory input (the AFM sensory neurons driving current is set to 0). To simulate the conscious decision to move the limb, the motor neurons receive a purple spike train from the brain via an AFM neuron with a driving current that exceeds the threshold (Fig. 6.3(c)). The signal sent by the brain causes the red agonist motor neurons to spike and the blue antagonist motor neurons to not spike, as illustrated by Fig. 6.3(d). The behavior of the motor neurons leads to muscle motion. A spike sequence indicates an excited motor neuron and, therefore, a simulated muscle contraction, whereas the absence of spikes indicates the suppression of a motor neuron and simulated muscle relaxation. From Fig. 6.3(d), it is clear that the agonist muscles (red) contract while the antagonist muscles (blue) relax, resulting in the limb's movement.

It is important to emphasize that the presence of the additional "motion" signal from the brain not only increased the spiking frequency of the agonist motor neuron but also completely suppressed the antagonist motor neuron. Such inhibitory behavior is ubiquitous in biological neural networks and vital for their proper functioning but is rather challenging to realize in conventional ANN without employing negative coupling weights. In our case, it is achieved by using simple inhibitor circuits, which are possible due to the inertial properties of AFM neurons [26]. This demonstrates that artificial AFM neurons

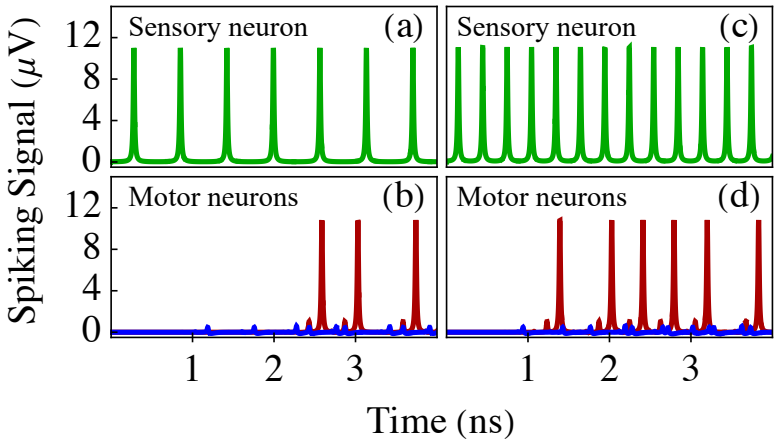

Figure 6.4: Simulated response of the withdrawal reflex arc to weak and strong sensory stimuli. (a) Spike train output of the AFM sensory neuron with a low frequency of 1.75 GHz (interspike delay 570 ps), indicating a weak stimulus. (b) Response of the motor neurons to the weak sensory stimulus. (c) Spike train output of the AFM sensory neuron with a high frequency of 3.25 GHz (delay 300 ps), indicating a strong stimulus. (d) Response of the motor neurons to the strong sensory stimulus.

are very well suited for simulations of biological neural networks and other systems with multiple competing signals.

6.4.3 Reaction to weak and strong stimuli

The next considered scenarios are the motor neurons' response to weak and strong sensory stimuli. The results of simulations of these two scenarios are illustrated in Fig. 6.4.

As a result of weak and strong stimuli, the green AFM sensory neuron enters the supercritical oscillator regime, where the driving current is above the threshold. In this regime, the frequency of the spike trains generated by the neuron is proportional to the magnitude of the driving current.

Figure 6.4(a) shows the green sensory neuron's output for a weak sensory stimulus, while Fig. 6.4(c) shows a strong sensory stimulus. The strength of the stimulus

is determined by the frequency of the spike train produced by the sensory neuron, with the strong and, therefore, more painful stimulus having a higher frequency. Biological sensory neurons encode pain similarly through this frequency encoding [216].

The motor neuron's response to the sensory stimulus can be seen in Fig. 6.4(b) and (d). Both figures show the red agonist motor neurons being excited (red curves) and causing muscle contractions, while the blue antagonist motor neurons (blue curves) are inhibited and, therefore, causing simulated muscle relaxation. As a result, the limb is moved away from the harmful stimulus. However, the response to the strong sensory stimulus, Fig. 6.4(d), happens over two times faster than the response to a weak sensory stimulus, Fig. 6.4(b).

The faster response, shown in Fig. 6.4(d), is caused by the involuntary withdrawal reflex and the interneurons. A weak stimulus with low frequency cannot induce excitation in the interneurons because the inhibitor circuits are weakly coupled. Consequently, a weaker or less painful sensory signal must first travel through the brain in order to reach the motor neurons, causing a significant delay between the sensory neuron's initial stimulus and the motor neurons' reaction. As in the biological response to pain, when the sensory signal is strong, indicating a painful stimulus, interneurons are activated, creating a shorter and faster pathway for the sensory signal to travel to the motor neurons.

6.4.4 Inhibition of the withdrawal reflex

Due to the realistic inhibition behavior of AFM neurons, it is possible to simulate another scenario: the inhibition of the withdrawal reflex. Simulations showing the interplay between the sensory neurons, the brain, and the subsequent inhibition of the withdrawal reflex in the motor neurons are shown in Fig 6.5.

In the simulations of the reflex inhibition scenario, the sensory neuron is in the strong stimulus regime, outputting a green spike train with a high frequency, as seen in Fig. 6.5(a), indicating a painful sensory stimulus. In normal conditions, the interneurons

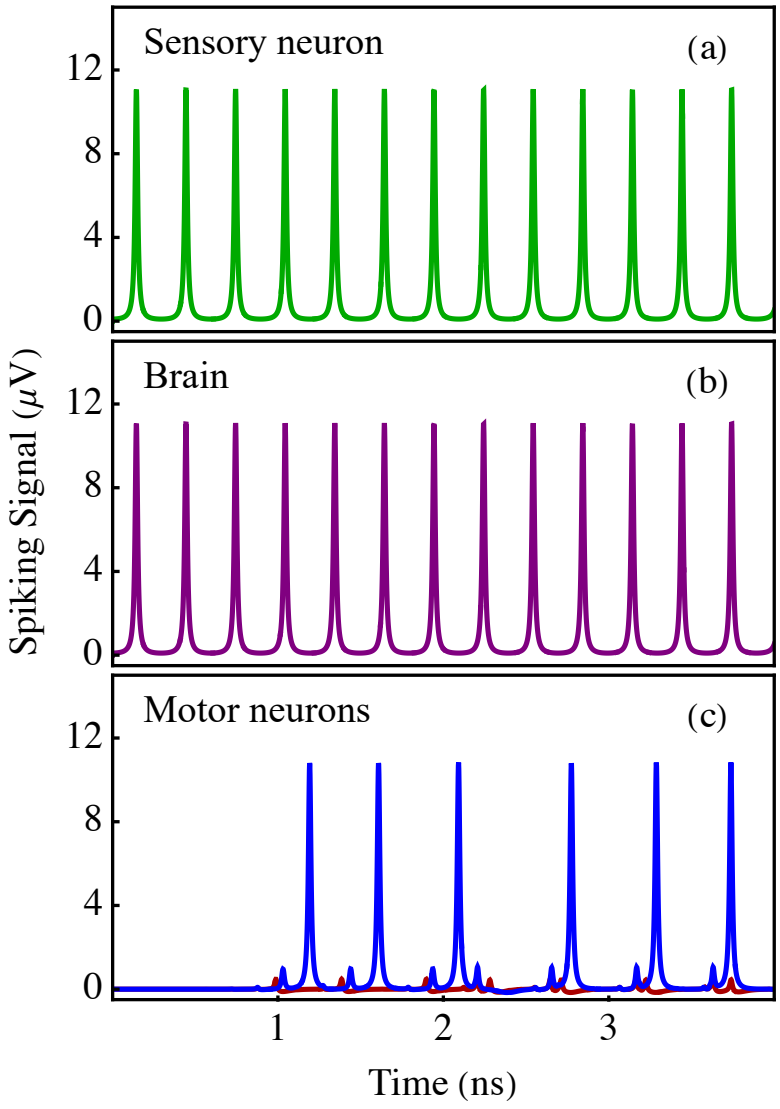

Figure 6.5: Simulated results for the inhibition of the withdrawal reflex. (a) Spike train output of the AFM sensory neuron with a high frequency of 3.25 GHz (interspike delay 300 ps), indicating a strong stimulus. (b) The signal generated by the brain to suppress the reflex. (c) Response of the motor neurons during the inhibition of the reflex regime.

would be excited, and the withdrawal reflex would be triggered. In this case, however, the brain sends a voluntary signal to the interneurons (Fig. 6.5(b)), inhibiting their output and simulating a conscious decision to neutralize the reflex. It is essential that the brain triggers the opposite reaction in the motor neurons to counteract the withdrawal reflex by relaxing the agonist muscles and contracting the antagonist muscles. Figure 6.5(c), the response of the motor neurons, illustrates this: the blue antagonist motor neurons spike, indicating muscle contraction, and the red agonist motor neurons do not spike, indicating muscle relaxation. As a result, instead of the withdrawal reflex removing the limb away from the harmful stimulus, it stays in contact with it.

As conventional inertia-less artificial neurons cannot simulate inhibition, the ability of the AFM neuron to simulate complex inhibition adds another level of realism to the modeling of biological neural networks.

6.5 Conclusion

By recreating the biological neural network of the withdrawal reflex using artificial neurons derived from AFM oscillators, we gain insight into its functionality and potential applications in robotics. The realistic inhibition of AFM neurons allows accurate replication of critical parts of the withdrawal reflex neural networks, enabling effective simulation of the reflex's five response regimes.

Many advantages arise from using AFM neurons to simulate biological systems. The action potential spikes generated by biological neurons have a duration on the order of milliseconds. In contrast, the AFM neurons used in this study have a spike width on the order of picoseconds due to the ultra-fast THz dynamics of AFM materials. Consequently, a direct comparison between biological and AFM neurons is not feasible. Nevertheless, the ultra-fast dynamics of AFM neurons suggest that any device utilizing them would achieve speeds notably exceeding those of biological neurons, offering a distinct advantage for the advancement of robotics. This spintronic neuromorphic computing

design paves the way for a high-speed and energy-efficient future in technology. Due to their ultra-fast dynamics, the AFM neural network is able to simulate the withdrawal reflex on the order of nanoseconds, as opposed to the biological withdrawal reflex, which takes half a second [215]. Thus, AFM neurons may not suit prosthetics but are ideal for high-speed robotics and bio-inspired AI.

Other biologically realistic ANNs of spinal reflexes can use over $2,000$ artificial neurons [208], [222]. The AFM withdrawal reflex neural network uses a total of 45 AFM neurons, most of which are hidden and used to simulate the brain. Additionally, there is no need for simulating adjustments in the synaptic weights in the AFM withdrawal reflex neural network. The network's static configuration of neurons and weights effectively reproduces the withdrawal reflex without the need for synaptic training. In addition, the network effectively reproduces the five regimes defined by the withdrawal reflex without the need for additional hardware or software elements related to machine learning.

The use of AFM neurons in the simulation of biological systems yields neural networks that are not only faster and more energy-efficient but also require fewer neurons. The demonstrated efficiency of the withdrawal reflex neural network model serves as a promising gateway for extending AFM neuron modeling to other biological networks, offering potential applications in both medicine and engineering.

CHAPTER SEVEN

CONCLUSIONS

Neuromorphic computing aims to explore alternative computing paradigms, striving to overcome the limitations of current technologies that hinder further technological progress. Spintronics, harnessing electron spin for developing low-power devices, offers promising avenues in this pursuit. The incorporation of spintronic devices into neuromorphic computing architectures heralds a future characterized by energy-efficient technologies. AFM oscillators, employing various spintronic principles, demonstrate the capability to generate frequencies in the terahertz range. Leveraging AFM oscillators, AFM neurons emerge as ultra-fast artificial neurons tailored for neuromorphic computing. These AFM neurons exhibit numerous distinctive features not found in other artificial neuron designs.

In the first study (Chapter 3), a comprehensive analysis of AFM neurons' characteristics is conducted. The internal effective inertia, resulting from the exchange interaction within AFM materials, gives rise to various biologically realistic attributes, such as response latency, finite refraction time, and bursting behavior. Moreover, chains of AFM neurons showcase the potential for both symmetric and asymmetric coupling. By leveraging the refraction time of AFM neurons, the creation of uni-directional signal propagation circuits is facilitated, even with symmetric coupling, through the isolator circuit.

Expanding upon the preceding investigation (Chapter 4), simple static AFM circuits are investigated. It is demonstrated that Boolean logic gates can be engineered using a single AFM neuron with specific static coupling. Additionally, the emulation of non-monotonic inhibition is achieved through the inhibitor circuit. This inhibitor can

operate effectively with all positive signals or capitalize on the reversible polarity of AFM neurons to provide negative inhibition. Subsequently, this inhibitor circuit can be integrated with basic rings to generate controllable memory cells.

In the next study (Chapter 5), AFM neurons are seamlessly integrated with machine learning algorithms to develop SNNs adept at pattern recognition. Initially, the SPAN algorithm is utilized to construct a single-layer neural network with a single output neuron. This network demonstrates the capability to recognize symbols generated from a pixelated grid within a few hundred picoseconds by triggering a spike at a target time. Subsequently, a backpropagation algorithm utilizing gradient descent is employed to train multilayered AFM neural networks. Initially, a 2-layer neural network is tested to validate the algorithm's efficacy in training AFM neurons using gradient descent. The algorithm then facilitates the creation of a multilayer AFM neural network employing a directed graph structure. This graph neural network exhibits proficiency in identifying sequential binary spiking patterns.

In the final study (Chapter 6), the striking parallels between AFM neurons and biological neurons are harnessed to emulate a biological neural network. Specifically, the withdrawal reflex—a polysynaptic reflex integrating sensory neurons, interneurons, and motor neurons—is meticulously replicated. Each element of the biological withdrawal reflex arc is faithfully emulated using AFM neurons, resulting in the construction of the AFM withdrawal reflex neural network. This network successfully reproduces five scenarios defining the functions of the withdrawal reflex. Notably, the reflex is observed in response to a strong sensory stimulus scenario, where the AFM neural network simulates the contraction and relaxation of the motor neurons within a matter of nanoseconds.

Based on these findings, AFM neurons emerge as a promising artificial neuron design capable of high-speed computation with remarkable energy efficiency. The theoretical exploration conducted in this dissertation highlights the potential of AFMs in

advancing spintronic neuromorphic computing architectures. Consequently, the results obtained justify the pursuit of experimental studies on AFM neurons. Through experimental realization, further investigations into AFM neural networks become feasible. Additionally, a comprehensive analysis of the synapses employed to interconnect AFM neurons would strengthen the case for the experimental implementation of AFM neurons.

APPENDIX A

PATTERN RECOGNITION NEURAL NETWORKS

A.1 SPAN neural network

The learning rate used in the SPAN algorithm, Eq. (5.1) is $\eta = 0.05$. Additionally, τ, the time constant related to the width of the output spike, is set to 100. Before training, the weights between the input neurons and the output SPAN neuron are initialized to a random value between $0\kappa_0$ and $1\kappa_0$. The weights in the multi SPAN neural network's output layer all have a value of $0.5\kappa_0$. This ensures a single spike is not enough for the post-synaptic neuron to fire, but two signals are strong enough to induce a spike.

A.2 Two layer neural network

The learning rate used in the gradient descent algorithm Eq. (5.4) is $\eta = 0.05$. Similar to the SPAN neural network, the weights of the 2-layer neural network are initialized to a random value. The weights between the input layer and the hidden layer are randomized between $0\kappa_0$ to $2\kappa_0$. The weights between the hidden layer and the output layer are randomized between $0\kappa_0$ to $1\kappa_0$.

A.3 Graph neural networks

The learning rate used in the gradient descent algorithm used to train the 2-input and 1-input graph neural networks, governed by Eqs (5.5), (5.14), and (5.22), is $\eta = 0.05$. The weights between the input layer and the hidden layer are randomized between $0\kappa_0$ to $2\kappa_0$. The weights within the hidden layer are randomized between $0\kappa_0$ to $1\kappa_0$. The weights between the hidden layer and the output layer are also randomized between $0\kappa_0$ to $1\kappa_0$. The WTA output layer consists of 3 interconnected inhibitor circuits. The weights related to the inhibitor circuit are found in Chapter 4.

APPENDIX B

WITHDRAWAL REFLEX NEURAL NETWORK

The most important parameter for simulating the withdrawal reflex lies in the difference in bias current for the different regimes. The magnitude of the bias current determines the regime in which the AFM neuron is operating. That is, if the bias current exceeds some threshold current I_{th}, the system will be in the super-critical regime acting as an auto-oscillator, continuously outputting a spike train. Below this threshold, the AFM neuron is in the subcritical regime, where the sublattices are stationary until acted upon by an additional external signal.

Most neurons in the withdrawal reflex neural network have a current value of 0.97 I_{th}, placing them in the subcritical regime. The AFM neurons acting as inputs to the neural network have above-threshold current values. These supercritical current values for muscle tone, weak stimulus, and strong stimulus are listed in Table B.1.

The complete AFM withdrawal reflex neural network can be seen in Fig. B.1. Neurons labeled 1-4 are in the supercritical state, acting as inputs to the neural network. Neuron 1 is the sensory input neuron and has current I_{weak} during the weak sensory stimulus scenario and I_{strong} during the strong sensory stimulus and the reflex inhibition scenarios. Neuron 2 is a supercritical neuron acting as the muscle tone input and has the bias current I_{tone} during all scenarios. Neuron 3 is a supercritical neuron acting as the input during the voluntary motion scenario. During this scenario, it has the bias current I_{weak}. Neuron 4 is a supercritical neuron acting as the brain's input during the inhibition

Table B.1: Bias current values in the AFM withdrawal reflex neural network.

Parameter	Description	Simulation value
I_{th}	Threshold current	0.203 mA
I_{sub}	Subcritical current	0.97 I_{th}
I_{tone}	Supercritical tone current	1.001 I_{th}
I_{weak}	Supercritical weak current	1.005 I_{th}
I_{strong}	Supercritical strong current	1.018 I_{th}

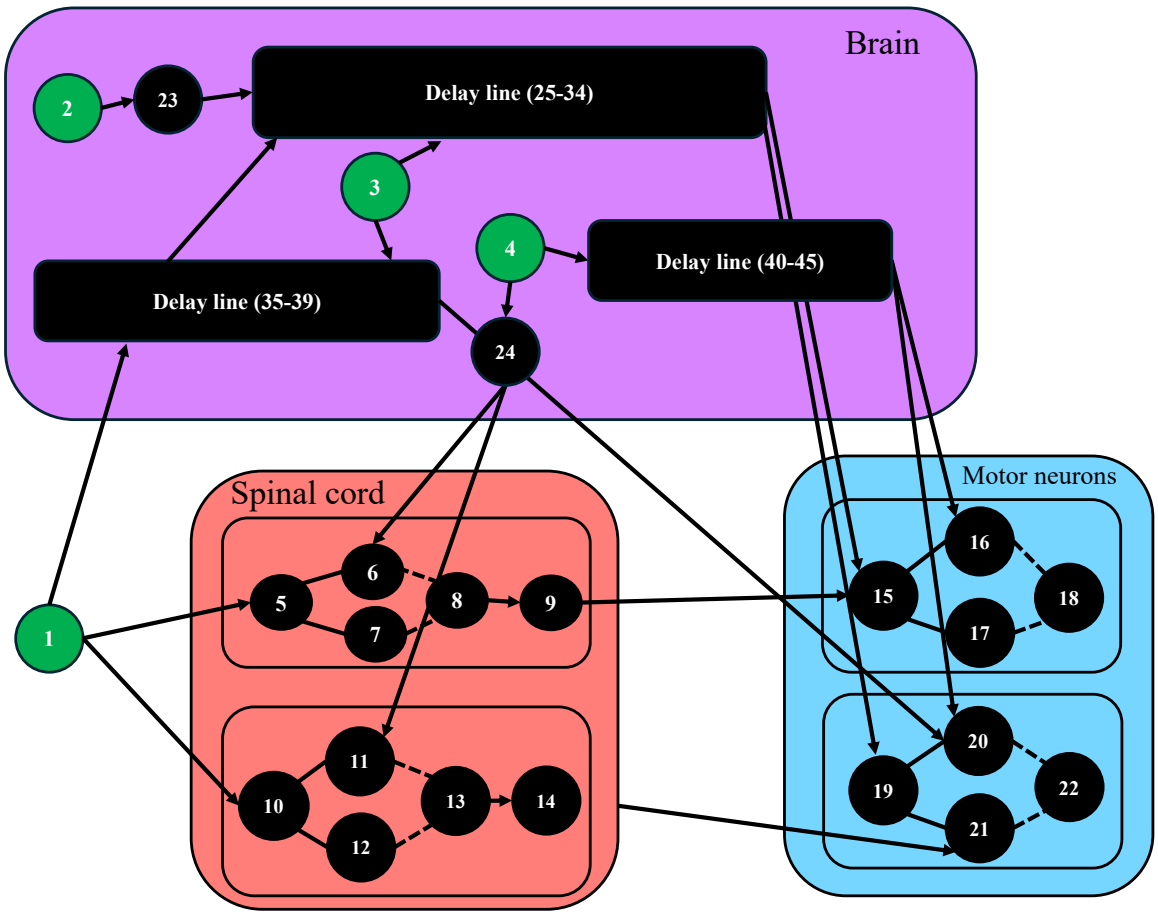

Figure B.1: Complete AFM withdrawal reflex neural network. Green circles are AFM neurons acting in the supercritical regime acting as inputs to the neural network. Black circles are neurons acting in the subcritical regime. Black boxes labeled delay lines consist of multiple subcritical neurons linked in a chain.

of a reflex scenario. During this scenario, this neuron has the bias current I_{strong}. These current values are listed in Table B.1.

The synaptic connections of the withdrawal reflex neural network are determined via non-zero elements in a sparse array. A majority of the synaptic connections in the neural network have the coupling coefficient $\kappa_0 = 0.011$. This value was determined from Chapter 3 and Ref. [26], where simple chains of AFM neurons are simulated. Some

Table B.2: Synaptic connections in the AFM withdrawal reflex neural network. Synaptic connections are determined via non-zero elements in a sparse array. These non-zero elements have the value of the coupling coefficient κ.

Coupling coefficient	Synapse
$\kappa_0 = 0.011$	(1,5),(1,10),(1,35),(35,36),(36,37), (37,38),(38,39),(35,25),(2,23),(23,25), (25,26),(26,27),(27,28),(28,29),(29,30), (30,31),(31,32),(32,33),(33,34),(34,15), (34,19),(3,39),(3,34),(4,24),(24,6), (24,11),(4,40),(40,41),(41,42),(42,43), (43,44),(44,45),(45,16),(45,20),(39,20), (10,11),(10,12),(13,14),(5,6),(5,7), (8,9),(15,16),(15,17),(19,20),(19,21)
$\kappa = 0.5k_0$	(6,8),(7,8),(11,13),(12,13),(16,18), (17,18),(20,22),(21,22)

neurons in the inhibitor circuit exhibit weak coupling, illustrated by the dashed lines in Fig. B.1. These connections have a coupling coefficient of $0.5\kappa_0$. The inhibitor circuit and its coupling constants were studied in detail in Chapter 4 and Ref. [26]. Synaptic connections in the AFM withdrawal reflex neural network are listed in Table B.2.

REFERENCES

[1] J. Puebla, J. Kim, K. Kondou, and Y. Otani, "Spintronic devices for energy-efficient data storage and energy harvesting," en, *Communications Materials*, vol. 1, no. 1, pp. 1–9, May 2020, Publisher: Nature Publishing Group, ISSN: 2662-4443. DOI: 10.1038/s43246-020-0022-5.

[2] W. Kang, E. Deng, Z. Wang, and W. Zhao, "Spintronic Logic-in-Memory Paradigms and Implementations," en, in *Applications of Emerging Memory Technology: Beyond Storage*, M. Suri, Ed., Singapore: Springer, 2020, pp. 215–229, ISBN: 9789811383793. DOI: 10.1007/978-981-13-8379-3_9.

[3] S. Matsunaga, J. Hayakawa, S. Ikeda, *et al.*, "MTJ-based nonvolatile logic-in-memory circuit, future prospects and issues," in *Automation & Test in Europe Conference & Exhibition 2009 Design*, ISSN: 1558-1101, Apr. 2009, pp. 433–435. DOI: 10.1109/DATE.2009.5090704.

[4] S. Bhatti, R. Sbiaa, A. Hirohata, H. Ohno, S. Fukami, and S. N. Piramanayagam, "Spintronics based random access memory: A review," *Materials Today*, vol. 20, no. 9, pp. 530–548, Nov. 2017, ISSN: 1369-7021. DOI: 10.1016/j.mattod.2017.07.007.

[5] S. S. P. Parkin, M. Hayashi, and L. Thomas, "Magnetic Domain-Wall Racetrack Memory," *Science*, vol. 320, no. 5873, pp. 190–194, Apr. 2008, Publisher: American Association for the Advancement of Science. DOI: 10.1126/science.1145799.

[6] F. Ogban, I. Arikpo, and I. Eteng, "Von Neumann Architecture and Modern Computers.," *Global Journal of Mathematical Sciences Vol. 6, No. 2, 2007, Page 97: ISSN 1596-6208 Indexed and abstracted on AJOL (UK): http://www.ajol.info*, vol. Vol. 6, No. 2, 2007, Page 97, Sep. 2007. DOI: 10.4314/gjmas.v6i2.21415.

[7] R. Eigenmann and D. J. Lilja, "Von Neumann Computers," en, in *Wiley Encyclopedia of Electrical and Electronics Engineering*, J. G. Webster, Ed., 1st ed., Wiley, Dec. 1999, ISBN: 978-0-471-34608-1. DOI: 10.1002/047134608X.W1704.

[8] W. B. Levy and V. G. Calvert, "Communication consumes 35 times more energy than computation in the human cortex, but both costs are needed to predict synapse number," eng, *Proceedings of the National Academy of Sciences of the United States of America*, vol. 118, no. 18, e2008173118, May 2021, ISSN: 1091-6490. DOI: 10.1073/pnas.2008173118.

[9] E. Güreşen and G. Kayakutlu, "Definition of artificial neural networks with comparison to other networks," *Procedia CS*, vol. 3, pp. 426–433, Dec. 2011. DOI: 10.1016/j.procs.2010.12.071.

[10] T. Brown, B. Mann, N. Ryder, *et al.*, "Language Models are Few-Shot Learners," in *Advances in Neural Information Processing Systems*, vol. 33, Curran Associates, Inc., 2020, pp. 1877–1901.

[11] OpenAI, *GPT-4 Technical Report*, arXiv:2303.08774 [cs], Mar. 2023.

[12] S. McQuate, *UW researcher discusses just how much energy ChatGPT uses*, en.

[13] F.-h. Hsu, M. S. Campbell, and A. J. Hoane, "Deep Blue system overview," en, in *Proceedings of the 9th international conference on Supercomputing - ICS '95*, Barcelona, Spain: ACM Press, 1995, pp. 240–244, ISBN: 978-0-89791-728-5. DOI: 10.1145/224538.224567.

[14] D. Silver, A. Huang, C. J. Maddison, *et al.*, "Mastering the game of Go with deep neural networks and tree search," en, *Nature*, vol. 529, no. 7587, pp. 484–489, Jan. 2016, Number: 7587 Publisher: Nature Publishing Group, ISSN: 1476-4687. DOI: 10.1038/nature16961.

[15] A. Egri-Nagy and A. Törmänen, "The Game Is Not over Yet—Go in the Post-AlphaGo Era," en, *Philosophies*, vol. 5, no. 4, p. 37, Dec. 2020, Number: 4 Publisher: Multidisciplinary Digital Publishing Institute, ISSN: 2409-9287. DOI: 10.3390/philosophies5040037.

[16] M. Davies, N. Srinivasa, T.-H. Lin, *et al.*, "Loihi: A Neuromorphic Manycore Processor with On-Chip Learning," *IEEE Micro*, vol. 38, no. 11, pp. 82–99, Jan. 2018, ISSN: 0272-1732. DOI: 10.1109/MM.2018.112130359.

[17] M. Davies, A. Wild, G. Orchard, *et al.*, "Advancing Neuromorphic Computing With Loihi: A Survey of Results and Outlook," *Proceedings of the IEEE*, vol. 109, no. 5, pp. 911–934, May 2021, Conference Name: Proceedings of the IEEE, ISSN: 1558-2256. DOI: 10.1109/JPROC.2021.3067593.

[18] J. Grollier, D. Querlioz, K. Y. Camsari, K. Everschor-Sitte, S. Fukami, and M. D. Stiles, "Neuromorphic spintronics," en, *Nature Electronics*, vol. 3, no. 7, pp. 360–370, Jul. 2020, Number: 7 Publisher: Nature Publishing Group, ISSN: 2520-1131. DOI: 10.1038/s41928-019-0360-9.

[19] R. Ismael Salinas, P.-C. Chen, C.-Y. Yang, and C.-H. Lai, "Spintronic materials and devices towards an artificial neural network: Accomplishments and the last mile," *Materials Research Letters*, vol. 11, no. 5, pp. 305–326, May 2023, ISSN: null. DOI: 10.1080/21663831.2022.2147803.

[20] G. J. Lim, C. C. I. Ang, and W. S. Lew, "Spintronics for Neuromorphic Engineering," en, in *Emerging Non-volatile Memory Technologies: Physics, Engineering, and Applications*, W. S. Lew, G. J. Lim, and P. A. Dananjaya, Eds., Singapore: Springer, 2021, pp. 297–315, ISBN: 9789811569128. DOI: 10.1007/978-981-15-6912-8_9.

[21] R. Khymyn, I. Lisenkov, V. Tiberkevich, B. A. Ivanov, and A. Slavin, "Antiferromagnetic THz-frequency Josephson-like Oscillator Driven by Spin Current," en, *Scientific Reports*, vol. 7, no. 1, p. 43 705, Mar. 2017, ISSN: 2045-2322. DOI: 10.1038/srep43705.

[22] R. Khymyn, V. Tiberkevich, and A. Slavin, "Antiferromagnetic spin current rectifier," *AIP Advances*, vol. 7, no. 5, p. 055 931, Mar. 2017, ISSN: 2158-3226. DOI: 10.1063/1.4977974.

[23] R. Cheng, D. Xiao, and A. Brataas, "Terahertz Antiferromagnetic Spin Hall Nano-Oscillator," *Physical Review Letters*, vol. 116, no. 20, p. 207 603, May 2016, Publisher: American Physical Society. DOI: 10.1103/PhysRevLett.116.207603.

[24] O. R. Sulymenko, O. V. Prokopenko, V. S. Tiberkevich, A. N. Slavin, B. A. Ivanov, and R. S. Khymyn, "THz-Frequency Spin-Hall Auto-Oscillator Based on a Canted Antiferromagnet," *Physical Review Applied*, vol. 8, no. 6, p. 064 007, Dec. 2017, arXiv:1707.07491 [physics], ISSN: 2331-7019. DOI: 10.1103/PhysRevApplied.8.064007.

[25] G. Consolo, G. Valenti, A. R. Safin, S. A. Nikitov, V. Tyberkevich, and A. Slavin, "Theory of the electric field controlled antiferromagnetic spin Hall oscillator and detector," *Physical Review B*, vol. 103, no. 13, p. 134 431, Apr. 2021, Publisher: American Physical Society. DOI: 10.1103/PhysRevB.103.134431.

[26] H. Bradley, S. Louis, C. Trevillian, *et al.*, "Artificial neurons based on antiferromagnetic auto-oscillators as a platform for neuromorphic computing," en, *AIP Advances*, vol. 13, no. 1, p. 015 206, Jan. 2023, ISSN: 2158-3226. DOI: 10.1063/5.0128530.

[27] H. Bradley, S. Louis, A. Slavin, and V. Tyberkevych, *Pattern recognition using spiking antiferromagnetic neurons*, arXiv:2308.09071 [physics], Aug. 2023.

[28] H. Bradley, L. Quach, S. Louis, and V. Tyberkevych, *Antiferromagnetic Artificial Neuron Modeling of Biological Neural Networks*, Nov. 2023. DOI: 10.21203/rs.3.rs-3616808/v1.

[29] H. Bradley and V. Tyberkevych, *Inertial Artificial Neural Networks Based on Antiferromagnetic Oscillators*, Aug. 2020.

[30] H. Bradley and V. Tyberkevych, *Spike Pattern Association Neuron using Antiferromagnetic Artificial Neurons*, Aug. 2021.

[31] H. Bradley, S. Louis, and V. Tyberkevych, *Neuromorphic pattern recognition using antiferromagnetic artificial neurons*, Aug. 2022.

[32] H. Bradley, L. Quach, S. Louis, and V. Tyberkevych, *Antiferromagnetic artificial neuron modeling of biological neural networks*, Sep. 2023.

[33] H. Bradley, L. Quach, S. Louis, and V. Tyberkevych, *Antiferromagnetic artificial neuron modeling of biological neural networks*, Apr. 2023.

[34] H. Bradley, S. Louis, and V. Tyberkevych, *Antiferromagnetic Artificial Neural Networks with Symmetric Coupling*, Apr. 2021.

[35] H. Bradley, L. Quach, S. Louis, and V. Tyberkevych, *Antiferromagnetic artificial neuron modeling of biological neural networks*, May 2023.

[36] H. Bradley, V. Tyberkevych, and A. Slavin, *Gradient Descent Learning in Multilayer Antiferromagnetic Neural Networks*, May 2024.

[37] H. Bradley and V. Tyberkevych, *Spike Pattern Recognition Using Antiferromagnetic Artificial Neurons*, Aug. 2022.

[38] H. Bradley, L. Quach, S. Louis, and V. Tyberkevych, *Antiferromagnetic artificial neuron modeling of biological neural networks*, Aug. 2023.

[39] H. Bradley and V. Tyberkevych, *Neuromorphic Memory Rings Based on Artificial Antiferromagnetic Neurons*, Mar. 2021.

[40] H. Bradley and V. Tyberkevych, *Spike Pattern Recognition Using Antiferromagnetic Artificial Neurons*, Mar. 2022.

[41] H. Bradley, L. Quach, S. Louis, and V. Tyberkevych, *Antiferromagnetic artificial neuron modeling of biological neural networks*, Mar. 2023.

[42] H. Bradley and V. Tyberkevych, *Dynamic Effects of Exchange Inertia in Artificial Neural Networks Based on Antiferromagnetic Oscillators.* Nov. 2020.

[43] H. Bradley, S. Louis, and V. Tyberkevych, *Pattern Recognition Using Antiferromagnetic Artificial Spiking Neurons*, Oct. 2022.

[44] H. Bradley and V. Tyberkevych, *Exchange Inertia Effects in Artificial Neural Networks Using Antiferromagnetic Oscillators.* Nov. 2020.

[45] H. Bradley and V. Tyberkevych, *Neuromorphic Computing Using Artificial Antiferromagnetic Neurons*, May 2021.

[46] H. Bradley, V. Tyberkevych, and A. Slavin, *Gradient Descent Learning in Multilayer Antiferromagnetic Neural Networks*, Apr. 2024.

[47] S. B. Marc Cahay Marc, *Introduction to Spintronics*, 2nd ed. Boca Raton: CRC Press, Sep. 2015, ISBN: 978-0-429-15638-0. DOI: 10.1201/b19103.

[48] A. Hirohata and K. Takanashi, "Future perspectives for spintronic devices," en, *Journal of Physics D: Applied Physics*, vol. 47, no. 19, p. 193 001, Apr. 2014, Publisher: IOP Publishing, ISSN: 0022-3727. DOI: 10.1088/0022-3727/47/19/193001.

[49] A. Hirohata, K. Yamada, Y. Nakatani, *et al.*, "Review on spintronics: Principles and device applications," *Journal of Magnetism and Magnetic Materials*, vol. 509, p. 166 711, Sep. 2020, ISSN: 0304-8853. DOI: 10.1016/j.jmmm.2020.166711.

[50] A. Hirohata, H. Sukegawa, H. Yanagihara, *et al.*, "Roadmap for Emerging Materials for Spintronic Device Applications," *IEEE Transactions on Magnetics*, vol. 51, no. 10, pp. 1–11, Oct. 2015, Conference Name: IEEE Transactions on Magnetics, ISSN: 1941-0069. DOI: 10.1109/TMAG.2015.2457393.

[51] E. Vedmedenko, R. Kawakami, D. Sheka, *et al.*, "The 2020 Magnetism Roadmap," *Journal of Physics D: Applied Physics*, vol. 53, Jun. 2020. DOI: 10.1088/1361-6463/ab9d98.

[52] M. N. Baibich, J. M. Broto, A. Fert, *et al.*, "Giant Magnetoresistance of (001)Fe/(001)Cr Magnetic Superlattices," *Physical Review Letters*, vol. 61, no. 21, pp. 2472–2475, Nov. 1988, Publisher: American Physical Society. DOI: 10.1103/PhysRevLett.61.2472.

[53] G. Binasch, P. Grünberg, F. Saurenbach, and W. Zinn, "Enhanced magnetoresistance in layered magnetic structures with antiferromagnetic interlayer exchange," *Physical Review B*, vol. 39, no. 7, pp. 4828–4830, Mar. 1989, Publisher: American Physical Society. DOI: 10.1103/PhysRevB.39.4828.

[54] U. Hartmann and R. Coehoorn, *Magnetic Multilayers and Giant Magnetoresistance: Fundamentals and Industrial Applications*, en. Springer Science & Business Media, Jan. 2000, Google-Books-ID: Iefd6kCbFxsC, ISBN: 978-3-540-65568-8.

[55] H. Yoda, "MRAM Fundamentals and Devices," en, in *Handbook of Spintronics*, Y. Xu, D. D. Awschalom, and J. Nitta, Eds., Dordrecht: Springer Netherlands, 2016, pp. 1031–1064, ISBN: 978-94-007-6892-5. DOI: 10.1007/978-94-007-6892-5_39.

[56] J. W. Lu, E. Chen, M. Kabir, M. R. Stan, and S. A. Wolf, "Spintronics technology: Past, present and future," *International Materials Reviews*, vol. 61, no. 7, pp. 456–472, Oct. 2016, Publisher: SAGE Publications, ISSN: 0950-6608. DOI: 10.1080/09506608.2016.1204097.

[57] S. A. Wolf, D. D. Awschalom, R. A. Buhrman, *et al.*, "Spintronics: A Spin-Based Electronics Vision for the Future," *Science*, vol. 294, no. 5546, pp. 1488–1495, Nov. 2001, Publisher: American Association for the Advancement of Science. DOI: 10.1126/science.1065389.

[58] N. F. Mott and R. H. Fowler, "The electrical conductivity of transition metals," *Proceedings of the Royal Society of London. Series A - Mathematical and Physical Sciences*, vol. 153, no. 880, pp. 699–717, Jan. 1997, Publisher: Royal Society. DOI: 10.1098/rspa.1936.0031.

[59] P. Dey and J. N. Roy, "Spin-Transfer Torque," en, in *Spintronics: Fundamentals and Applications*, P. Dey and J. N. Roy, Eds., Singapore: Springer, 2021, pp. 127–144, ISBN: 9789811600692. DOI: 10.1007/978-981-16-0069-2_5.

[60] T. Shinjo, Ed., *Nanomagnetism and Spintronics*, English, 2nd edition. Amsterdam Walthan, MA: Elsevier, Oct. 2013, ISBN: 978-0-444-63279-1.

[61] D. C. Ralph and M. D. Stiles, "Spin transfer torques," *Journal of Magnetism and Magnetic Materials*, vol. 320, no. 7, pp. 1190–1216, Apr. 2008, ISSN: 0304-8853. DOI: 10.1016/j.jmmm.2007.12.019.

[62] J. C. Slonczewski, "Current-driven excitation of magnetic multilayers," *Journal of Magnetism and Magnetic Materials*, vol. 159, no. 1, pp. L1–L7, Jun. 1996, ISSN: 0304-8853. DOI: 10.1016/0304-8853(96)00062-5.

[63] L. Berger, "Emission of spin waves by a magnetic multilayer traversed by a current," eng, *Physical Review. B, Condensed Matter*, vol. 54, no. 13, pp. 9353–9358, Oct. 1996, ISSN: 0163-1829. DOI: 10.1103/physrevb.54.9353.

[64] Y. Tserkovnyak, A. Brataas, and G. E. W. Bauer, "Enhanced Gilbert Damping in Thin Ferromagnetic Films," *Physical Review Letters*, vol. 88, no. 11, p. 117 601, Feb. 2002, Publisher: American Physical Society. DOI: 10.1103/PhysRevLett.88.117601.

[65] Y. Tserkovnyak, A. Brataas, and G. E. W. Bauer, "Spin pumping and magnetization dynamics in metallic multilayers," *Physical Review B*, vol. 66, no. 22, p. 224 403, Dec. 2002, Publisher: American Physical Society. DOI: 10.1103/PhysRevB.66.224403.

[66] Y. Tserkovnyak, A. Brataas, G. E. W. Bauer, and B. I. Halperin, "Nonlocal magnetization dynamics in ferromagnetic heterostructures," en, *Reviews of Modern Physics*, vol. 77, no. 4, pp. 1375–1421, Dec. 2005, ISSN: 0034-6861, 1539-0756. DOI: 10.1103/RevModPhys.77.1375.

[67] A. Brataas, Y. Tserkovnyak, G. E. W. Bauer, and B. I. Halperin, "Spin battery operated by ferromagnetic resonance," *Physical Review B*, vol. 66, no. 6, p. 060 404, Aug. 2002, Publisher: American Physical Society. DOI: 10.1103/PhysRevB.66.060404.

[68] P. Dey and J. N. Roy, "Basic Elements of Spintronics," en, in *Spintronics: Fundamentals and Applications*, P. Dey and J. N. Roy, Eds., Singapore: Springer, 2021, pp. 23–73, ISBN: 9789811600692. DOI: 10.1007/978-981-16-0069-2_2.

[69] J. Sinova, J. Wunderlich, and T. Jungwirth, "Anomalous and Spin-Injection Hall Effects," in *Handbook of Spin Transport and Magnetism*, Num Pages: 18, Chapman and Hall/CRC, 2012, ISBN: 978-0-429-19287-6.

[70] M. L. Néel, "Propriétés magnétiques des ferrites ; ferrimagnétisme et antiferromagnétisme," fr, *Annales de Physique*, vol. 12, no. 3, pp. 137–198, 1948, Number: 3 Publisher: EDP Sciences, ISSN: 0003-4169, 1286-4838. DOI: 10.1051/anphys/194812030137.

[71] L. Néel, "Magnetism and Local Molecular Field," *Science*, vol. 174, no. 4013, pp. 985–992, Dec. 1971, Publisher: American Association for the Advancement of Science. DOI: 10.1126/science.174.4013.985.

[72] J. M. D. Coey, *Magnetism and Magnetic Materials*. Cambridge: Cambridge University Press, 2010, ISBN: 978-0-521-81614-4. DOI: 10.1017/CBO9780511845000.

[73] S. A. Siddiqui, J. Sklenar, K. Kang, *et al.*, "Metallic antiferromagnets," *Journal of Applied Physics*, vol. 128, no. 4, p. 040 904, Jul. 2020, ISSN: 0021-8979. DOI: 10.1063/5.0009445.

[74] V. Baltz, A. Manchon, M. Tsoi, T. Moriyama, T. Ono, and Y. Tserkovnyak, "Antiferromagnetic spintronics," *Reviews of Modern Physics*, vol. 90, no. 1, p. 015 005, Feb. 2018, Publisher: American Physical Society. DOI: 10.1103/RevModPhys.90.015005.

[75] A. F. Andreev and V. I. Marchenko, "Symmetry and the macroscopic dynamics of magnetic materials," en, *Soviet Physics Uspekhi*, vol. 23, no. 1, p. 21, Jan. 1980, Publisher: IOP Publishing, ISSN: 0038-5670. DOI: 10.1070/PU1980v023n01ABEH004859.

[76] B. A. Ivanov, "Spin dynamics of antiferromagnets under action of femtosecond laser pulses (Review Article)," en, *Low Temperature Physics*, vol. 40, no. 2, pp. 91–105, Feb. 2014, ISSN: 1063-777X, 1090-6517. DOI: 10.1063/1.4865565.

[77] S. S. Hernandez and J. M. H. Ferras, "Ferromagnetic resonance in Yttrium Iron Garnet," en, 2017.

[78] S. I. Kiselev, J. C. Sankey, I. N. Krivorotov, *et al.*, "Microwave oscillations of a nanomagnet driven by a spin-polarized current," en, *Nature*, vol. 425, no. 6956, pp. 380–383, Sep. 2003, Number: 6956 Publisher: Nature Publishing Group, ISSN: 1476-4687. DOI: 10.1038/nature01967.

[79] W. H. Rippard, M. R. Pufall, S. Kaka, S. E. Russek, and T. J. Silva, "Direct-Current Induced Dynamics in Co90Fe10/Ni80Fe20 Point Contacts," *Physical Review Letters*, vol. 92, no. 2, p. 027 201, Jan. 2004, Publisher: American Physical Society. DOI: 10.1103/PhysRevLett.92.027201.

[80] V. E. Demidov, S. Urazhdin, H. Ulrichs, *et al.*, "Magnetic nano-oscillator driven by pure spin current," en, *Nature Materials*, vol. 11, no. 12, pp. 1028–1031, Dec. 2012, Number: 12 Publisher: Nature Publishing Group, ISSN: 1476-4660. DOI: 10.1038/nmat3459.

[81] V. E. Demidov, S. Urazhdin, A. Zholud, A. V. Sadovnikov, and S. O. Demokritov, "Nanoconstriction-based spin-Hall nano-oscillator," *Applied Physics Letters*, vol. 105, no. 17, p. 172 410, Oct. 2014, ISSN: 0003-6951. DOI: 10.1063/1.4901027.

[82] Z. Duan, A. Smith, L. Yang, *et al.*, "Nanowire spin torque oscillator driven by spin orbit torques," en, *Nature Communications*, vol. 5, no. 1, p. 5616, Dec. 2014, Number: 1 Publisher: Nature Publishing Group, ISSN: 2041-1723. DOI: 10.1038/ncomms6616.

[83] M. Collet, X. de Milly, O. d'Allivy Kelly, *et al.*, "Generation of coherent spin-wave modes in yttrium iron garnet microdiscs by spin–orbit torque," en, *Nature Communications*, vol. 7, no. 1, p. 10 377, Jan. 2016, Number: 1 Publisher: Nature Publishing Group, ISSN: 2041-1723. DOI: 10.1038/ncomms10377.

[84] J.-G. Choi, J. Park, M.-G. Kang, *et al.*, "Voltage-driven gigahertz frequency tuning of spin Hall nano-oscillators," en, *Nature Communications*, vol. 13, no. 1, p. 3783, Jun. 2022, Number: 1 Publisher: Nature Publishing Group, ISSN: 2041-1723. DOI: 10.1038/s41467-022-31493-z.

[85] E. V. Gomonay and V. M. Loktev, "Spintronics of antiferromagnetic systems (Review Article)," en, *Low Temperature Physics*, vol. 40, no. 1, pp. 17–35, Jan. 2014, ISSN: 1063-777X, 1090-6517. DOI: 10.1063/1.4862467.

[86] H. V. Gomonay and V. M. Loktev, "Spin transfer and current-induced switching in antiferromagnets," *Physical Review B*, vol. 81, no. 14, p. 144 427, Apr. 2010, Publisher: American Physical Society. DOI: 10.1103/PhysRevB.81.144427.

[87] R. Cheng, M. W. Daniels, J.-G. Zhu, and D. Xiao, "Ultrafast switching of antiferromagnets via spin-transfer torque," *Physical Review B*, vol. 91, no. 6, p. 064 423, Feb. 2015, Publisher: American Physical Society. DOI: 10.1103/PhysRevB.91.064423.

[88] J. Sinova, S. O. Valenzuela, J. Wunderlich, C. H. Back, and T. Jungwirth, "Spin Hall effects," *Reviews of Modern Physics*, vol. 87, no. 4, pp. 1213–1260, Oct. 2015, ISSN: 0034-6861, 1539-0756. DOI: 10.1103/RevModPhys.87.1213.

[89] A. Hoffmann, "Spin Hall Effects in Metals," *IEEE Transactions on Magnetics*, vol. 49, no. 10, pp. 5172–5193, Oct. 2013, ISSN: 0018-9464, 1941-0069. DOI: 10.1109/TMAG.2013.2262947.

[90] J. M. Meckbach, *Superconducting multilayer technology for Josephson devices: technology, engineering, physics, applications* (Karlsruher Schriftenreihe zur Supraleitung). KIT Scientific Publ, 2013, ISBN: 978-3-7315-0122-0.

[91] P. Anderson, *Lectures on the Many-body Problem*. Academic Press, 1964.

[92] A. M. Turing, "Computing Machinery and Intelligence," en, *Mind*, vol. 59, no. 236, pp. 433–460, 1950.

[93] M. Roser, *The brief history of artificial intelligence: The world has changed fast – what might be next?* Dec. 2022.

[94] Z. Shao, R. Zhao, S. Yuan, M. Ding, and Y. Wang, "Tracing the evolution of AI in the past decade and forecasting the emerging trends," *Expert Systems with Applications*, vol. 209, p. 118 221, Dec. 2022, ISSN: 0957-4174. DOI: 10.1016/j.eswa.2022.118221.

[95] "Big data needs a hardware revolution," en, *Nature*, vol. 554, no. 7691, pp. 145–146, Feb. 2018, Bandiera_abtest: a Cg_type: Editorial Number: 7691 Publisher: Nature Publishing Group Subject_term: Computer science, Mathematics and computing. DOI: 10.1038/d41586-018-01683-1.

[96] S. Mittal, "A Survey of ReRAM-Based Architectures for Processing-In-Memory and Neural Networks," en, *Machine Learning and Knowledge Extraction*, vol. 1, no. 1, pp. 75–114, Mar. 2019, Number: 1 Publisher: Multidisciplinary Digital Publishing Institute, ISSN: 2504-4990. DOI: 10.3390/make1010005.

[97] X. Zou, S. Xu, X. Chen, L. Yan, and Y. Han, "Breaking the von Neumann bottleneck: Architecture-level processing-in-memory technology," en, *Science China Information Sciences*, vol. 64, no. 6, p. 160 404, Apr. 2021, ISSN: 1869-1919. DOI: 10.1007/s11432-020-3227-1.

[98] A. Gulati, "Understanding neurogenesis in the adult human brain," *Indian Journal of Pharmacology*, vol. 47, no. 6, pp. 583–584, 2015, ISSN: 0253-7613. DOI: 10.4103/0253-7613.169598.

[99] J. Zhu, T. Zhang, Y. Yang, and R. Huang, "A comprehensive review on emerging artificial neuromorphic devices," *Applied Physics Reviews*, vol. 7, no. 1, p. 011 312, Feb. 2020, ISSN: 1931-9401. DOI: 10.1063/1.5118217.

[100] D. V. Christensen, R. Dittmann, B. Linares-Barranco, *et al.*, "2022 roadmap on neuromorphic computing and engineering," en, *Neuromorphic Computing and Engineering*, vol. 2, no. 2, p. 022 501, Jun. 2022, ISSN: 2634-4386. DOI: 10.1088/2634-4386/ac4a83.

[101] K. Gurney, *An Introduction to Neural Networks*, English, 1st edition. London: CRC Press, Aug. 1997, ISBN: 978-1-85728-503-1.

[102] R. Rojas, *Neural Networks: A Systematic Introduction*, en. Springer Science & Business Media, Jun. 2013, Google-Books-ID: 4rESBwAAQBAJ, ISBN: 978-3-642-61068-4.

[103] J. Delua, *Supervised vs. Unsupervised Learning: What's the Difference?* en-US, Mar. 2021.

[104] M. Alloghani, D. Al-Jumeily, J. Mustafina, A. Hussain, and A. J. Aljaaf, "A Systematic Review on Supervised and Unsupervised Machine Learning Algorithms for Data Science," en, in *Supervised and Unsupervised Learning for Data Science*, ser. Unsupervised and Semi-Supervised Learning, M. W. Berry, A. Mohamed, and B. W. Yap, Eds., Cham: Springer International Publishing,

2020, pp. 3–21, ISBN: 978-3-030-22475-2. DOI: 10.1007/978-3-030-22475-2_1.

[105] S. Dridi, *Supervised Learning - A Systematic Literature Review*, en-us, Apr. 2022. DOI: 10.31219/osf.io/tysr4.

[106] A. Singh, N. Thakur, and A. Sharma, "A review of supervised machine learning algorithms," in *2016 3rd International Conference on Computing for Sustainable Global Development (INDIACom)*, Mar. 2016, pp. 1310–1315.

[107] S. Naeem, A. Ali, S. Anam, and M. Ahmed, "An Unsupervised Machine Learning Algorithms: Comprehensive Review," *IJCDS Journal*, vol. 13, pp. 911–921, Apr. 2023. DOI: 10.12785/ijcds/130172.

[108] T. P. Lillicrap and A. Santoro, "Backpropagation through time and the brain," *Current Opinion in Neurobiology*, Machine Learning, Big Data, and Neuroscience, vol. 55, pp. 82–89, Apr. 2019, ISSN: 0959-4388. DOI: 10.1016/j.conb.2019.01.011.

[109] T. P. Lillicrap, A. Santoro, L. Marris, C. J. Akerman, and G. Hinton, "Backpropagation and the brain," en, *Nature Reviews Neuroscience*, vol. 21, no. 6, pp. 335–346, Jun. 2020, Number: 6 Publisher: Nature Publishing Group, ISSN: 1471-0048. DOI: 10.1038/s41583-020-0277-3.

[110] R. Rojas, "The Backpropagation Algorithm," en, in *Neural Networks: A Systematic Introduction*, R. Rojas, Ed., Berlin, Heidelberg: Springer, 1996, pp. 149–182, ISBN: 978-3-642-61068-4. DOI: 10.1007/978-3-642-61068-4_7.

[111] S. H. Haji and A. M. Abdulazeez, "Comparison of optimization techniques based on gradient decent algorithm: A review," en, *PalArch's Journal of Archaeology of Egypt / Egyptology*, vol. 18, no. 4, pp. 2715–2743, Feb. 2021, Number: 4, ISSN: 1567-214X.

[112] S. Ruder, *An overview of gradient descent optimization algorithms*, arXiv:1609.04747 [cs], Jun. 2017. DOI: 10.48550/arXiv.1609.04747.

[113] M. H. Grider, R. Jessu, and R. Kabir, "Physiology, Action Potential," eng, in *StatPearls*, Treasure Island (FL): StatPearls Publishing, 2023.

[114] Y. Guo, X. Huang, and Z. Ma, "Direct learning-based deep spiking neural networks: A review," *Frontiers in Neuroscience*, vol. 17, 2023, ISSN: 1662-453X.

[115] K. Yamazaki, V.-K. Vo-Ho, D. Bulsara, and N. Le, "Spiking Neural Networks and Their Applications: A Review," *Brain Sciences*, vol. 12, no. 7, p. 863, Jun. 2022, ISSN: 2076-3425. DOI: 10.3390/brainsci12070863.

[116] M. Pfeiffer and T. Pfeil, "Deep Learning With Spiking Neurons: Opportunities and Challenges," *Frontiers in Neuroscience*, vol. 12, 2018, ISSN: 1662-453X.

[117] F. Ponulak and A. Kasinski, "Introduction to spiking neural networks: Information processing, learning and applications," eng, *Acta neurobiologiae experimentalis*, vol. 71, no. 4, pp. 409–433, Jan. 2011, ISSN: 1689-0035.

[118] A. L. Hodgkin and A. F. Huxley, "A quantitative description of membrane current and its application to conduction and excitation in nerve," *The Journal of Physiology*, vol. 117, no. 4, pp. 500–544, Aug. 1952, ISSN: 0022-3751.

[119] R. B. Stein, "Some Models of Neuronal Variability," *Biophysical Journal*, vol. 7, no. 1, pp. 37–68, Jan. 1967, ISSN: 0006-3495.

[120] L. Lapicque, "Quantitative investigations of electrical nerve excitation treated as polarization. 1907," eng, *Biological Cybernetics*, vol. 97, no. 5-6, pp. 341–349, Dec. 2007, ISSN: 0340-1200. DOI: 10.1007/s00422-007-0189-6.

[121] D.-A. Nguyen, X.-T. Tran, and F. Iacopi, "A Review of Algorithms and Hardware Implementations for Spiking Neural Networks," en, *Journal of Low Power Electronics and Applications*, vol. 11, no. 2, p. 23, Jun. 2021, Number: 2 Publisher: Multidisciplinary Digital Publishing Institute, ISSN: 2079-9268. DOI: 10.3390/jlpea11020023.

[122] Y. Dong, D. Zhao, Y. Li, and Y. Zeng, "An unsupervised STDP-based spiking neural network inspired by biologically plausible learning rules and connections," *Neural Networks*, vol. 165, pp. 799–808, Aug. 2023, ISSN: 0893-6080. DOI: 10.1016/j.neunet.2023.06.019.

[123] S. Song, K. D. Miller, and L. F. Abbott, "Competitive Hebbian learning through spike-timing-dependent synaptic plasticity," en, *Nature Neuroscience*, vol. 3, no. 9, pp. 919–926, Sep. 2000, Number: 9 Publisher: Nature Publishing Group, ISSN: 1546-1726. DOI: 10.1038/78829.

[124] G.-q. Bi and M.-m. Poo, "Synaptic Modifications in Cultured Hippocampal Neurons: Dependence on Spike Timing, Synaptic Strength, and Postsynaptic Cell Type," en, *The Journal of Neuroscience*, vol. 18, no. 24, pp. 10 464–10 472, Dec. 1998, ISSN: 0270-6474, 1529-2401. DOI: 10.1523/JNEUROSCI.18-24-10464.1998.

[125] Y. Dan and M.-M. Poo, "Spike Timing-Dependent Plasticity: From Synapse to Perception," *Physiological Reviews*, vol. 86, no. 3, pp. 1033–1048, Jul. 2006, Publisher: American Physiological Society, ISSN: 0031-9333. DOI: 10.1152/physrev.00030.2005.

[126] S. M. Bohte, J. N. Kok, and H. La Poutré, "Error-backpropagation in temporally encoded networks of spiking neurons," *Neurocomputing*, vol. 48, no. 1, pp. 17–37, Oct. 2002, ISSN: 0925-2312. DOI: 10.1016/S0925-2312(01)00658-0.

[127] S. B. Shrestha and Q. Song, "Robustness to Training Disturbances in SpikeProp Learning," en, *IEEE Transactions on Neural Networks and Learning Systems*, vol. 29, no. 7, pp. 3126–3139, Jul. 2018, ISSN: 2162-237X, 2162-2388. DOI: 10.1109/TNNLS.2017.2713125.

[128] S. McKennoch, Dingding Liu, and L. Bushnell, "Fast Modifications of the SpikeProp Algorithm," en, in *The 2006 IEEE International Joint Conference on Neural Network Proceedings*, Vancouver, BC, Canada: IEEE, 2006, pp. 3970–3977, ISBN: 978-0-7803-9490-2. DOI: 10.1109/IJCNN.2006.246918.

[129] A. Sengupta, K. Yogendra, and K. Roy, "Spintronic devices for ultra-low power neuromorphic computation (Special session paper)," in *2016 IEEE International Symposium on Circuits and Systems (ISCAS)*, ISSN: 2379-447X, May 2016, pp. 922–925. DOI: 10.1109/ISCAS.2016.7527392.

[130] J. Grollier, D. Querlioz, and M. D. Stiles, "Spintronic Nanodevices for Bioinspired Computing," en, *Proceedings of the IEEE. Institute of Electrical and Electronics Engineers*, vol. 104, no. 10, p. 2024, Oct. 2016, Publisher: NIH Public Access. DOI: 10.1109/JPROC.2016.2597152.

[131] G. Finocchio, J. A. C. Incorvia, J. S. Friedman, *et al.*, "Roadmap for Unconventional Computing with Nanotechnology," en, *Nano Futures*, 2024, ISSN: 2399-1984. DOI: 10.1088/2399-1984/ad299a.

[132] A. Sengupta, P. Panda, P. Wijesinghe, Y. Kim, and K. Roy, "Magnetic Tunnel Junction Mimics Stochastic Cortical Spiking Neurons," en, *Scientific Reports*, vol. 6, no. 1, p. 30 039, Jul. 2016, Number: 1 Publisher: Nature Publishing Group, ISSN: 2045-2322. DOI: 10.1038/srep30039.

[133] J. Cai, B. Fang, L. Zhang, *et al.*, "Voltage-Controlled Spintronic Stochastic Neuron Based on a Magnetic Tunnel Junction," en, *Physical Review Applied*, vol. 11, no. 3, p. 034 015, Mar. 2019, ISSN: 2331-7019. DOI: 10.1103/PhysRevApplied.11.034015.

[134] Q. Zheng, X. Zhu, Y. Mi, Z. Yuan, and K. Xia, "Recurrent neural networks made of magnetic tunnel junctions," *AIP Advances*, vol. 10, no. 2, p. 025 116, Feb. 2020, Publisher: American Institute of Physics. DOI: 10.1063/1.5143382.

[135] D. Wang, R. Tang, H. Lin, *et al.*, "Spintronic leaky-integrate-fire spiking neurons with self-reset and winner-takes-all for neuromorphic computing," en, *Nature Communications*, vol. 14, no. 1, p. 1068, Feb. 2023, Number: 1 Publisher: Nature Publishing Group, ISSN: 2041-1723. DOI: 10.1038/s41467-023-36728-1.

[136] D. R. Rodrigues, R. Moukhader, Y. Luo, *et al.*, "Spintronic Hodgkin-Huxley-Analogue Neuron Implemented with a Single Magnetic Tunnel Junction," *Physical Review Applied*, vol. 19, no. 6, p. 064 010, Jun. 2023, Publisher: American Physical Society. DOI: 10.1103/PhysRevApplied.19.064010.

[137] D. A. Allwood, G. Xiong, C. C. Faulkner, D. Atkinson, D. Petit, and R. P. Cowburn, "Magnetic domain-wall logic," eng, *Science (New York, N.Y.)*, vol. 309, no. 5741, pp. 1688–1692, Sep. 2005, ISSN: 1095-9203. DOI: 10.1126/science.1108813.

[138] S. Dutta, S. A. Siddiqui, F. Büttner, L. Liu, C. A. Ross, and M. A. Baldo, "A logic-in-memory design with 3-terminal magnetic tunnel junction function evaluators for convolutional neural networks," in *2017 IEEE/ACM International Symposium on Nanoscale Architectures (NANOARCH)*, ISSN: 2327-8226, Jul. 2017, pp. 83–88. DOI: 10.1109/NANOARCH.2017.8053724.

[139] A. Sengupta and K. Roy, "A Vision for All-Spin Neural Networks: A Device to System Perspective," *IEEE Transactions on Circuits and Systems I: Regular Papers*, vol. 63, no. 12, pp. 2267–2277, Dec. 2016, Conference Name: IEEE Transactions on Circuits and Systems I: Regular Papers, ISSN: 1558-0806. DOI: 10.1109/TCSI.2016.2615312.

[140] N. Hassan, X. Hu, L. Jiang-Wei, *et al.*, "Magnetic domain wall neuron with lateral inhibition," *Journal of Applied Physics*, vol. 124, no. 15, p. 152 127, Oct. 2018, ISSN: 0021-8979. DOI: 10.1063/1.5042452.

[141] A. Sengupta, Y. Shim, and K. Roy, "Proposal for an All-Spin Artificial Neural Network: Emulating Neural and Synaptic Functionalities Through Domain Wall Motion in Ferromagnets," *IEEE Transactions on Biomedical Circuits and Systems*, vol. 10, no. 6, pp. 1152–1160, Dec. 2016, Conference Name: IEEE Transactions on Biomedical Circuits and Systems, ISSN: 1940-9990. DOI: 10.1109/TBCAS.2016.2525823.

[142] W. H. Brigner, J. S. Friedman, N. Hassan, *et al.*, "Shape-Based Magnetic Domain Wall Drift for an Artificial Spintronic Leaky Integrate-and-Fire Neuron," en, *IEEE Transactions on Electron Devices*, vol. 66, no. 11, pp. 4970–4975, Nov. 2019, ISSN: 0018-9383, 1557-9646. DOI: 10.1109/TED.2019.2938952.

[143] N. Nagaosa and Y. Tokura, "Topological properties and dynamics of magnetic skyrmions," en, *Nature Nanotechnology*, vol. 8, no. 12, pp. 899–911, Dec. 2013, Number: 12 Publisher: Nature Publishing Group, ISSN: 1748-3395. DOI: 10.1038/nnano.2013.243.

[144] X. Chen, W. Kang, D. Zhu, *et al.*, "A compact skyrmionic leaky-integrate-fire spiking neuron device," *Nanoscale*, vol. 10, p. 6139, Feb. 2018. DOI: 10.1039/C7NR09722K.

[145] S. Li, W. Kang, Y. Huang, X. Zhang, Y. Zhou, and W. ZHAO, "Magnetic skyrmion-based artificial neuron device," *Nanotechnology*, vol. 28, 31LT01, Jul. 2017. DOI: 10.1088/1361-6528/aa7af5.

[146] S. Liu, G. Wang, T. Bai, *et al.*, "Magnetic Skyrmion-Based Spiking Neural Network for Pattern Recognition," en, *Applied Sciences*, vol. 12, no. 19, p. 9698, Jan. 2022, Number: 19 Publisher: Multidisciplinary Digital Publishing Institute, ISSN: 2076-3417. DOI: 10.3390/app12199698.

[147] Z. Zeng, G. Finocchio, and H. Jiang, "Spin transfer nano-oscillators," en, *Nanoscale*, vol. 5, no. 6, pp. 2219–2231, Mar. 2013, Publisher: The Royal Society of Chemistry, ISSN: 2040-3372. DOI: 10.1039/C2NR33407K.

[148] J. Torrejon, M. Riou, F. A. Araujo, *et al.*, "Neuromorphic computing with nanoscale spintronic oscillators," en, *Nature*, vol. 547, no. 7664, pp. 428–431, Jul. 2017, Number: 7664 Publisher: Nature Publishing Group, ISSN: 1476-4687. DOI: 10.1038/nature23011.

[149] N. Leroux, A. Mizrahi, D. Markovic, *et al.*, "Hardware realization of the multiply and accumulate operation on radio-frequency signals with magnetic tunnel junctions," *Neuromorphic Computing and Engineering*, vol. 1, Apr. 2021. DOI: 10.1088/2634-4386/abfca6.

[150] A. Ross, N. Leroux, A. De Riz, *et al.*, "Multilayer spintronic neural networks with radiofrequency connections," en, *Nature Nanotechnology*, vol. 18, no. 11, pp. 1273–1280, Nov. 2023, Number: 11 Publisher: Nature Publishing Group, ISSN: 1748-3395. DOI: 10.1038/s41565-023-01452-w.

[151] T. Jungwirth, J. Wunderlich, and K. Olejník, "Spin Hall effect devices," en, *Nature Materials*, vol. 11, no. 5, pp. 382–390, May 2012, Number: 5 Publisher: Nature Publishing Group, ISSN: 1476-4660. DOI: 10.1038/nmat3279.

[152] T. Chen, R. K. Dumas, A. Eklund, *et al.*, "Spin-Torque and Spin-Hall Nano-Oscillators," en, *Proceedings of the IEEE*, vol. 104, no. 10, pp. 1919–1945, Oct. 2016, ISSN: 0018-9219, 1558-2256. DOI: 10.1109/JPROC.2016.2554518.

[153] M. Zahedinejad, A. A. Awad, S. Muralidhar, *et al.*, "Two-dimensional mutually synchronized spin Hall nano-oscillator arrays for neuromorphic computing," en, *Nature Nanotechnology*, vol. 15, no. 1, pp. 47–52, Jan. 2020, Number: 1 Publisher: Nature Publishing Group, ISSN: 1748-3395. DOI: 10.1038/s41565-019-0593-9.

[154] S. Manna, R. Medwal, and R. S. Rawat, "Reconfigurable neural spiking in bias field free spin Hall nano-oscillator," en, *Physical Review B*, vol. 108, no. 18, p. 184 411, Nov. 2023, ISSN: 2469-9950, 2469-9969. DOI: 10.1103/PhysRevB.108.184411.

[155] D. Marković, M. W. Daniels, P. Sethi, A. D. Kent, M. D. Stiles, and J. Grollier, "Easy-plane spin Hall nano-oscillators as spiking neurons for neuromorphic computing," en, *Physical Review B*, vol. 105, no. 1, p. 014 411, Jan. 2022, ISSN: 2469-9950, 2469-9969. DOI: 10.1103/PhysRevB.105.014411.

[156] V. Brehm, J. W. Austefjord, S. Lepadatu, and A. Qaiumzadeh, "A proposal for leaky integrate-and-fire neurons by domain walls in antiferromagnetic insulators," en, *Scientific Reports*, vol. 13, no. 1, p. 13 404, Aug. 2023, Number: 1 Publisher: Nature Publishing Group, ISSN: 2045-2322. DOI: 10.1038/s41598-023-40575-x.

[157] S. Zhang and Y. Tserkovnyak, "Antiferromagnet-Based Neuromorphics Using Dynamics of Topological Charges," en, *Physical Review Letters*, vol. 125, no. 20, p. 207 202, Nov. 2020, ISSN: 0031-9007, 1079-7114. DOI: 10.1103/PhysRevLett.125.207202.

[158] N. Bindal, R. K. Raj, and B. K. Kaushik, "Antiferromagnetic skyrmion based shape-configured leaky-integrate-fire neuron device," en, *Journal of Physics D: Applied Physics*, vol. 55, no. 34, p. 345 007, Jun. 2022, Publisher: IOP Publishing, ISSN: 0022-3727. DOI: 10.1088/1361-6463/ac71e4.

[159] N. Bindal, C. A. C. Ian, W. S. Lew, and B. K. Kaushik, "Antiferromagnetic skyrmion repulsion based artificial neuron device," en, *Nanotechnology*, vol. 32, no. 21, p. 215 204, Mar. 2021, Publisher: IOP Publishing, ISSN: 0957-4484. DOI: 10.1088/1361-6528/abe261.

[160] R. Khymyn, I. Lisenkov, J. Voorheis, *et al.*, "Ultra-fast artificial neuron: Generation of picosecond-duration spikes in a current-driven antiferromagnetic auto-oscillator," en, *Scientific Reports*, vol. 8, no. 1, p. 15 727, Oct. 2018, Number: 1 Publisher: Nature Publishing Group, ISSN: 2045-2322. DOI: 10.1038/s41598-018-33697-0.

[161] J. E. Hirsch, "Spin Hall Effect," *Physical Review Letters*, vol. 83, no. 9, pp. 1834–1837, Aug. 1999, Publisher: American Physical Society. DOI: 10.1103/PhysRevLett.83.1834.

[162] E. Saitoh, M. Ueda, H. Miyajima, and G. Tatara, "Conversion of spin current into charge current at room temperature: Inverse spin-Hall effect," en, *Applied Physics Letters*, vol. 88, no. 18, p. 182 509, May 2006, ISSN: 0003-6951, 1077-3118. DOI: 10.1063/1.2199473.

[163] W. C. Stewart, "Current-Voltage Characteristics of Josephson Junctions," *Applied Physics Letters*, vol. 12, pp. 277–280, Apr. 1968, ADS Bibcode: 1968ApPhL..12..277S, ISSN: 0003-6951. DOI: 10.1063/1.1651991.

[164] M. Zahedinejad, H. Mazraati, H. Fulara, *et al.*, "CMOS compatible W/CoFeB/MgO spin Hall nano-oscillators with wide frequency tunability," *Applied Physics Letters*, vol. 112, no. 13, p. 132 404, 2018, Publisher: AIP Publishing LLC, ISSN: 0003-6951. DOI: 10.1063/1.5022049.

[165] C. Frenkel, M. Lefebvre, J.-D. Legat, and D. Bol, "A 0.086-mm ^2 12.7-pJ/SOP 64k-Synapse 256-Neuron Online-Learning Digital Spiking Neuromorphic Processor in 28nm CMOS," *IEEE Transactions on Biomedical Circuits and Systems*, vol. 13, no. 1, pp. 145–158, 2018, ISSN: 1932-4545, 1940-9990. DOI: 10.1109/TBCAS.2018.2880425.

[166] S. K. Esser, P. A. Merolla, J. V. Arthur, *et al.*, "Convolutional networks for fast, energy-efficient neuromorphic computing," *Proceedings of the National Academy of Sciences*, vol. 113, no. 4141, pp. 11 441–11 446, Oct. 2016, ISSN: 0027-8424, 1091-6490. DOI: 10.1073/pnas.1604850113.

[167] P. Livi and G. Indiveri, "A current-mode conductance-based silicon neuron for address-event neuromorphic systems," in *2009 IEEE International Symposium on Circuits and Systems*, ISSN: 2158-1525, May 2009, pp. 2898–2901. DOI: 10.1109/ISCAS.2009.5118408.

[168] K. Yogendra, D. Fan, and K. Roy, "Coupled Spin Torque Nano Oscillators for Low Power Neural Computation," *IEEE Transactions on Magnetics*, vol. 51, no. 10, pp. 1–9, Oct. 2015, Conference Name: IEEE Transactions on Magnetics, ISSN: 1941-0069. DOI: 10.1109/TMAG.2015.2443042.

[169] J. D. Kendall and S. Kumar, "The building blocks of a brain-inspired computer," *Applied Physics Reviews*, vol. 7, no. 1, p. 011 305, 2020, Publisher: AIP Publishing LLC, ISSN: 1931-9401. DOI: 10.1063/1.5129306.

[170] N. H. D. Khang, Y. Ueda, and P. N. Hai, "A conductive topological insulator with large spin Hall effect for ultralow power spin–orbit torque switching," *Nature Materials*, vol. 17, no. 9, pp. 808–813, 2018, Publisher: Nature Publishing Group, ISSN: 1476-4660. DOI: 10.1038/s41563-018-0137-y.

[171] S. Louis, H. Bradley, A. Slavin, and V. Tyberkevych, "Artificial neuron designed using a spin Josephson oscillator based on a synthetic antiferromagnet," *Abstracts of Joint MMM-Intermag 2022*, GPD–03, 2022.

[172] Y. Liu, I. Barsukov, Y. Barlas, I. N. Krivorotov, and R. K. Lake, "Synthetic antiferromagnet-based spin Josephson oscillator," *Applied Physics Letters*, vol. 116, no. 13, p. 132 409, 2020, Publisher: AIP Publishing LLC.

[173] L. Squire, D. Berg, F. E. Bloom, S. Du Lac, A. Ghosh, and N. C. Spitzer, *Fundamental neuroscience*. Academic press, 2012.

[174] M. Levakova, M. Tamborrino, S. Ditlevsen, and P. Lansky, "A review of the methods for neuronal response latency estimation," *Biosystems*, vol. 136, pp. 23–34, 2015, Publisher: Elsevier, ISSN: 1872-8324. DOI: 10.1016/j.biosystems.2015.04.008.

[175] P. Overton and D. Clark, "Burst firing in midbrain dopaminergic neurons," *Brain Research Reviews*, vol. 25, no. 3, pp. 312–334, 1997, Publisher: Elsevier. DOI: 10.1016/s0165-0173(97)00039-8.

[176] R. Krahe and F. Gabbiani, "Burst firing in sensory systems," *Nature Reviews Neuroscience*, vol. 5, no. 1, pp. 13–23, 2004, Publisher: Nature Publishing Group, ISSN: 1471-0048. DOI: 10.1038/nrn1296.

[177] E. M. Izhikevich, "Which model to use for cortical spiking neurons?" *IEEE Transactions on Neural Networks*, vol. 15, no. 5, pp. 1063–1070, 2004, Publisher: Ieee, ISSN: 1941-0093. DOI: 10.1109/TNN.2004.832719.

[178] W. Gerstner, W. M. Kistler, R. Naud, and L. Paninski, *Neuronal dynamics: From single neurons to networks and models of cognition*. Cambridge University Press, 2014.

[179] T. Aoyagi, N. Terada, Y. Kang, T. Kaneko, and T. Fukai, "A bursting mechanism of chattering neurons based on Ca2+-dependent cationic currents," en, *Neurocomputing*, vol. 38-40, pp. 93–98, Jun. 2001, ISSN: 09252312. DOI: 10.1016/S0925-2312(01)00540-9.

[180] D. U. Silverthorn, *Human physiology*. Jones & Bartlett Publishers, 2015.

[181] D. Purves, G. J. Augustine, D. Fitzpatrick, *et al.*, *Neuroscience*, 2nd ed. Sunderland, Mass: Sinauer Associates, 2001, ISBN: 978-0-87893-742-4.

[182] K. P. McKenna and G. J. Morgan, "Quantum simulations of spin-relaxation and transport in copper," en, *The European Physical Journal B*, vol. 59, no. 4, pp. 451–456, Oct. 2007, ISSN: 1434-6028, 1434-6036. DOI: https://doi.org/10.1140/epjb/e2007-00305-2.

[183] S. H. Jo, T. Chang, I. Ebong, B. B. Bhadviya, P. Mazumder, and W. Lu, "Nanoscale memristor device as synapse in neuromorphic systems," *Nano Letters*, vol. 10, no. 4, pp. 1297–1301, 2010, Publisher: ACS Publications, ISSN: 1530-6984. DOI: 10.1021/nl904092h.

[184] P.-P. Lu, J.-X. Shen, D.-S. Shang, and Y. Sun, "Artificial synaptic device based on a multiferroic heterostructure," *Journal of Physics D: Applied Physics*, vol. 52, no. 46, p. 465 303, 2019, Publisher: IOP Publishing, ISSN: 0022-3727. DOI: 10.1088/1361-6463/ab3b33.

[185] M. L. Schneider, C. A. Donnelly, S. E. Russek, *et al.*, "Ultralow power artificial synapses using nanotextured magnetic Josephson junctions," *Science Advances*, vol. 4, no. 1, e1701329, Jan. 2018, ISSN: 2375-2548. DOI: 10.1126/sciadv.1701329.

[186] C. Bartolozzi and G. Indiveri, "Synaptic dynamics in analog VLSI," *Neural Computation*, vol. 19, no. 10, pp. 2581–2603, 2007, Publisher: MIT Press, ISSN: 0899-7667. DOI: 10.1162/neco.2007.19.10.2581.

[187] N. Leroux, D. Marković, E. Martin, *et al.*, "Radio-frequency multiply-and-accumulate operations with spintronic synapses," *Physical Review Applied*, vol. 15, no. 3, p. 034 067, 2021, Publisher: APS.

[188] A. F. Vincent, J. Larroque, N. Locatelli, *et al.*, "Spin-Transfer Torque Magnetic Memory as a Stochastic Memristive Synapse for Neuromorphic Systems," en, *IEEE Transactions on Biomedical Circuits and Systems*, vol. 9, no. 2, pp. 166–174, Apr. 2015, ISSN: 1932-4545, 1940-9990. DOI: 10.1109/TBCAS.2015.2414423.

[189] L. Martins, A. S. Jenkins, L. S. E. Alvarez, *et al.*, "Non-volatile artificial synapse based on a vortex nano-oscillator," en, *Scientific Reports*, vol. 11, no. 1, p. 16 094, Aug. 2021, Number: 1 Publisher: Nature Publishing Group, ISSN: 2045-2322. DOI: 10.1038/s41598-021-95569-4.

[190] O. Akinola, X. Hu, C. H. Bennett, M. Marinella, J. S. Friedman, and J. A. C. Incorvia, "Three-terminal magnetic tunnel junction synapse circuits showing spike-timing-dependent plasticity," *Journal of Physics D: Applied Physics*, vol. 52, no. 49, 49LT01, 2019, Publisher: IOP Publishing, ISSN: 0022-3727. DOI: 10.1088/1361-6463/ab4157.

[191] G. Narasimman, S. Roy, X. Fong, K. Roy, C.-H. Chang, and A. Basu, "A low-voltage, low power STDP synapse implementation using domain-wall magnets for spiking neural networks," in *2016 IEEE International Symposium on Circuits and Systems (ISCAS)*, IEEE, May 2016, pp. 914–917. DOI: 10.1109/ISCAS.2016.7527390.

[192] D. Bhowmik, U. Saxena, A. Dankar, *et al.*, "On-chip learning for domain wall synapse based Fully Connected Neural Network," *Journal of Magnetism and Magnetic Materials*, vol. 489, p. 165 434, 2019, Publisher: Elsevier, ISSN: 0304-8853. DOI: 10.1016/j.jmmm.2019.165434.

[193] S. Liu, T. P. Xiao, C. Cui, J. A. C. Incorvia, C. H. Bennett, and M. J. Marinella, "A domain wall-magnetic tunnel junction artificial synapse with notched geometry for accurate and efficient training of deep neural networks," en, *Applied Physics Letters*, vol. 118, no. 20, p. 202 405, May 2021, ISSN: 0003-6951, 1077-3118. DOI: 10.1063/5.0046032.

[194] K. M. Song, J.-S. Jeong, B. Pan, *et al.*, "Skyrmion-based artificial synapses for neuromorphic computing," en, *Nature Electronics*, vol. 3, no. 3, pp. 148–155, Mar. 2020, Number: 3 Publisher: Nature Publishing Group, ISSN: 2520-1131. DOI: 10.1038/s41928-020-0385-0.

[195] Y. Huang, W. Kang, X. Zhang, Y. Zhou, and W. Zhao, "Magnetic skyrmion-based synaptic devices," *Nanotechnology*, vol. 28, no. 8, 08LT02, 2017, Publisher: IOP Publishing, ISSN: 0957-4484. DOI: 10.1088/1361-6528/aa5838.

[196] D. Das, Y. Cen, J. Wang, and X. Fong, "Bilayer-Skyrmion based design of Neuron and Synapse for Spiking Neural Network," *Physical Review Applied*, vol. 19, no. 2, p. 024 063, 2022. DOI: 10.1103/PhysRevApplied.19.024063.

[197] R. J. Tocci, N. S. Widmer, and G. L. Moss, *Digital systems: principles and applications*, 10th ed., international ed. Pearson/Prentice Hall, 2007, ISBN: 978-0-13-173969-7.

[198] C. Hawkins, J. Segura, and P. Zarkesh-Ha, *CMOS Integrated Digital Electronics: A First Course*, en. IET Digital Library, Jan. 2013, ISBN: 978-1-61353-026-9. DOI: 10.1049/SBCS501E.

[199] O. Sulymenko, O. Prokopenko, I. Lisenkov, *et al.*, "Ultra-fast logic devices using artificial "neurons" based on antiferromagnetic pulse generators," *Journal of Applied Physics*, vol. 124, no. 15, p. 152 115, Oct. 2018, ISSN: 0021-8979, 1089-7550. DOI: 10.1063/1.5042348.

[200] B. J. Baars and N. M. Gage, *Cognition, brain, and consciousness: introduction to cognitive neuroscience*, en, 2nd ed. Burlington, MA: Academic Press/Elsevier, 2010, OCLC: ocn455870625, ISBN: 978-0-12-375070-9.

[201] H. Markram, M. Toledo-Rodriguez, Y. Wang, A. Gupta, G. Silberberg, and C. Wu, "Interneurons of the neocortical inhibitory system," en, *Nature Reviews Neuroscience*, vol. 5, no. 10, pp. 793–807, Oct. 2004, Number: 10 Publisher: Nature Publishing Group, ISSN: 1471-0048. DOI: 10.1038/nrn1519.

[202] A. Mohemmed, S. Schliebs, S. Matsuda, and N. Kasabov, "Method for Training a Spiking Neuron to Associate Input-Output Spike Trains," en, in *Engineering Applications of Neural Networks*, L. Iliadis and C. Jayne, Eds., ser. IFIP Advances in Information and Communication Technology, Berlin, Heidelberg: Springer, 2011, pp. 219–228, ISBN: 978-3-642-23957-1. DOI: 10.1007/978-3-642-23957-1_25.

[203] G. Tanaka, T. Yamane, J. B. Héroux, *et al.*, "Recent advances in physical reservoir computing: A review," en, *Neural Networks*, vol. 115, pp. 100–123, Jul. 2019, ISSN: 0893-6080. DOI: 10.1016/j.neunet.2019.03.005.

[204] A. Mohemmed, S. Schliebs, S. Matsuda, and N. Kasabov, "Training spiking neural networks to associate spatio-temporal input–output spike patterns," en, *Neurocomputing*, Timely Neural Networks Applications in Engineering, vol. 107, pp. 3–10, May 2013, ISSN: 0925-2312. DOI: 10.1016/j.neucom.2012.08.034.

[205] I. Sporea and A. Grüning, "Supervised Learning in Multilayer Spiking Neural Networks," *Neural Computation*, vol. 25, no. 2, pp. 473–509, Feb. 2013, ISSN: 0899-7667. DOI: 10.1162/NECO_a_00396.

[206] L. Thau, V. Reddy, and P. Singh, "Anatomy, Central Nervous System," eng, in *StatPearls*, Treasure Island (FL): StatPearls Publishing, 2023.

[207] B. L. Dalcin, F. A. Cruz, C. M. Cortez, and E. P. L. Passos, "Computer modeling of a spinal reflex circuit," en, *Brazilian Journal of Physics*, vol. 35, pp. 987–994, Dec. 2005, Publisher: Sociedade Brasileira de Física, ISSN: 0103-9733, 1678-4448. DOI: 10.1590/S0103-97332005000600013.

[208] A. H. A. Stienen, A. C. Schouten, J. Schuurmans, and F. C. T. van der Helm, "Analysis of reflex modulation with a biologically realistic neural network," en, *Journal of Computational Neuroscience*, vol. 23, no. 3, pp. 333–348, Dec. 2007, ISSN: 1573-6873. DOI: 10.1007/s10827-007-0037-7.

[209] L. Sun, Y. Du, H. Yu, H. Wei, W. Xu, and W. Xu, "An Artificial Reflex Arc That Perceives Afferent Visual and Tactile Information and Controls Efferent Muscular Actions," *Research*, vol. 2022, p. 9 851 843, Feb. 2022, ISSN: 2639-5274. DOI: 10.34133/2022/9851843.

[210] C. Bao, T.-H. Kim, A. Hassanpoor Kalhori, and W. S. Kim, "A 3D-printed neuromorphic humanoid hand for grasping unknown objects," en, *iScience*, vol. 25, no. 4, p. 104 119, Apr. 2022, ISSN: 2589-0042. DOI: 10.1016/j.isci.2022.104119.

[211] M. Folgheraiter and G. Gini, "Human-like reflex control for an artificial hand," en, *Biosystems*, Papers presented at the Fifth International Workshop on Information Processing in Cells and Tissues, vol. 76, no. 1, pp. 65–74, Aug. 2004, ISSN: 0303-2647. DOI: 10.1016/j.biosystems.2004.05.007.

[212] K. He, Y. Liu, M. Wang, *et al.*, "An Artificial Somatic Reflex Arc," en, *Advanced Materials*, vol. 32, no. 4, p. 1 905 399, 2020, _eprint: https://onlinelibrary.wiley.com/doi/pdf/10.1002/adma.201905399, ISSN: 1521-4095. DOI: 10.1002/adma.201905399.

[213] S. Payra, G. Loke, and Y. Fink, "Enabling Adaptive Robot-Environment Interaction and Context-Aware Artificial Somatosensory Reflexes through Sensor-Embedded Fibers," in *2020 IEEE MIT Undergraduate Research Technology Conference (URTC)*, Oct. 2020, pp. 1–4. DOI: 10.1109/URTC51696.2020.9668863.

[214] D. Wang, S. Zhao, L. Li, *et al.*, "All-Flexible Artificial Reflex Arc Based on Threshold-Switching Memristor," en, *Advanced Functional Materials*, vol. 32, no. 21, p. 2 200 241, 2022, _eprint: https://onlinelibrary.wiley.com/doi/pdf/10.1002/adfm.202200241, ISSN: 1616-3028. DOI: 10.1002/adfm.202200241.

[215] C. Derderian, K. R. Shumway, and P. Tadi, "Physiology, Withdrawal Response," eng, in *StatPearls*, Treasure Island (FL): StatPearls Publishing, 2023.

[216] A. E. Dubin and A. Patapoutian, "Nociceptors: The sensors of the pain pathway," *The Journal of Clinical Investigation*, vol. 120, no. 11, pp. 3760–3772, Nov. 2010, ISSN: 0021-9738. DOI: 10.1172/JCI42843.

[217] D. Institute of Medicine (US) Committee on Pain, M. Osterweis, A. Kleinman, and D. Mechanic, *The Anatomy and Physiology of Pain*, en. National Academies Press (US), 1987, Publication Title: Pain and Disability: Clinical, Behavioral, and Public Policy Perspectives.

[218] D. Purves, G. J. Augustine, D. Fitzpatrick, *et al.*, "Excitatory and Inhibitory Postsynaptic Potentials," en, *Neuroscience. 2nd edition*, 2001, Publisher: Sinauer Associates.

[219] M. L. Latash, "Muscle coactivation: Definitions, mechanisms, and functions," *Journal of Neurophysiology*, vol. 120, no. 1, pp. 88–104, Jul. 2018, Publisher: American Physiological Society, ISSN: 0022-3077. DOI: 10.1152/jn.00084.2018.

[220] R. H. S. Carpenter and B. Reddi, *Neurophysiology: a conceptual approach [free web resources, with Vitalsource ebook]*, eng, 5th ed. London: Hodder Arnold, 2012, ISBN: 978-1-4441-3517-6.

[221] J. Ganguly, D. Kulshreshtha, M. Almotiri, and M. Jog, "Muscle Tone Physiology and Abnormalities," *Toxins*, vol. 13, no. 4, p. 282, Apr. 2021, ISSN: 2072-6651. DOI: 10.3390/toxins13040282.

[222] D. P. Bashor, "A large-scale model of some spinal reflex circuits," en, *Biological Cybernetics*, vol. 78, no. 2, pp. 147–157, Feb. 1998, ISSN: 1432-0770. DOI: 10.1007/s004220050421.